LBL-37110
UC-410

Lawrence Berkeley Laboratory
UNIVERSITY OF CALIFORNIA

Materials Sciences Division

Nonlinear Optical Spectroscopy of Diamond Surfaces

R.P. Chin
(Ph.D. Thesis)

April 1995

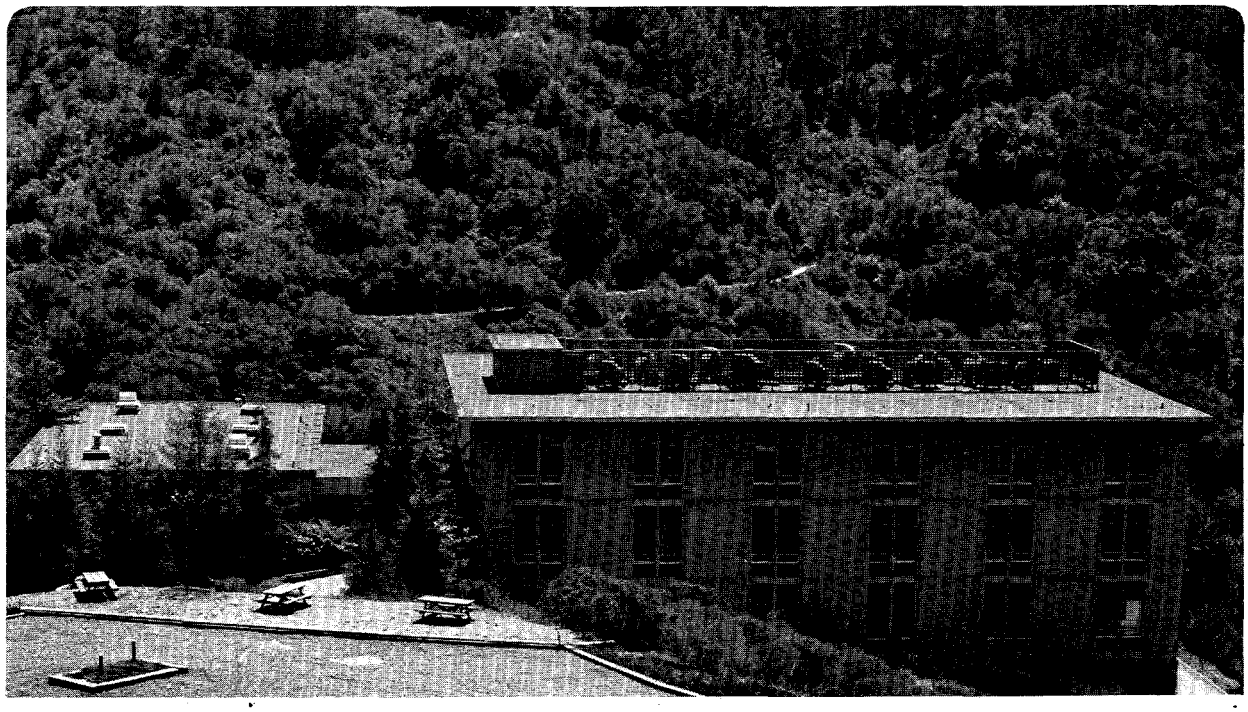

Prepared for the U.S. Department of Energy under Contract Number DE-AC03-76SF00098

LBL-37110

NONLINEAR OPTICAL SPECTROSCOPY OF DIAMOND SURFACES

RODNEY PETER CHIN
Ph.D. Thesis

DEPARTMENT OF PHYSICS
University of California

and

MATERIALS SCIENCES DIVISION
Lawrence Berkeley Laboratory
University of California
Berkeley, CA 94720

APRIL 1995

This work was supported by the Director, Office of Energy Research, Office of Basic Energy Sciences, Materials Sciences Division, of the U.S. Department of Energy under Contract No. DE-AC03-76SF00098.

Abstract

Nonlinear Optical Spectroscopy of Diamond Surfaces

by

Rodney Peter Chin

Doctor of Philosophy in Physics

University of California at Berkeley

Professor Yuen Ron Shen, Chair

Second harmonic generation (SHG) and infrared-visible sum frequency generation (SFG) spectroscopies have been shown to be powerful and versatile for studying surfaces with submonolayer sensitivity. They have been used in this work to study bare diamond surfaces and molecular adsorption on them. In particular, infrared-visible SFG as a surface vibrational spectroscopic technique has been employed to identify and monitor in-situ surface bonds and species on the diamond (111) surface. The CH stretch spectra allow us to investigate hydrogen adsorption, desorption, abstraction, and the nature of the hydrogen termination. The C(111) surface dosed with atomic hydrogen was found to be in a monohydride configuration with the hydrogen atoms situated at top-sites. The ratio of the abstraction rate to the adsorption rate was appreciable during atomic hydrogen dosing. Kinetic parameters for thermal desorption of H on C(111) were determined showing a near first-order kinetics. For the fully H-terminated (111) surface, a large (110 cm^{-1}) anharmonicity and ~19 psec lifetime were measured for the first-excited CH stretch mode. The bare reconstructed C(111)-(2x1) surface showed the presence of CC stretch modes which were consistent with the Pandey π-bonded chain structure. When exposed to the methyl radical, the SFG spectra of the C(111) surface showed features suggesting the presence of adsorbed methyl species. After heating to sufficiently high temperatures, they

were converted into the monohydride species. Preliminary results on the hydrogen-terminated diamond (100) surface are also presented.

Acknowledgments

First, I am grateful to Professor Y.R. Shen for his wisdom, scientific knowledge and patience. His intuition and clarity of thought have set high standards for all of us as graduate students.

As I gaze at the thirteen logbooks on my floor, I can't help but think of all the time I've spent in the lab. To all the members of the Shen group, past and present, I thank you for your support and encouragement. I would like to thank the members of the group who contributed to my stay here: Tom Moses, for proving that your whole system could (almost) be homemade; Dieter Wilk, for the alliance on many projects and mutual support; X.D. Zhu, who was my mentor at the beginning; Jung Huang, for introducing me to the SFG technique; Chris Mullin, who always seemed to have some time for conversation; Marla Feller and Rich Superfine, for providing a focus to keep the group together; Xu-dong Xiao, for always providing some comic relief; Colin Stanners for good conversation of life and science; Doseok Kim and Quan Du for much needed equipment loans; and Paul Cremer, the future keeper of my laser system who has been my chemistry "devil's advocate". In addition, I express much thanks to our group secretaries, Rita Jones, Barbara Gordon, and Barbara Iwai for their dedication to the group (you know you've been here too long when you need to thank three group secretaries). I would like to also express my appreciation to Sandy Stewart for always pushing purchase orders through and for the friendship which made life in Bldg. 66 more enjoyable.

I would like to thank my friend, Sue Melnik, who is a graduate student at Caltech, for so many discussions about life and each of our diamond projects.

A special thanks to Prof. Gabor Somorjai and his group for providing general support of the building 66 laboratory which has been my home for almost five years.

Before I came to Berkeley, I knew this was a special physics department. I am particularly grateful to Ken Miller and Prof. Buford Price who were instrumental in

bringing me here. Also, I would like to thank Donna Sakima, Helen Mayer, and Anne Takizawa for their help, advice and diversions. Finally, a thousand thanks to the members of the electronics and machine shops (UC campus and LBL) for their expert support.

I am extremely indebted to my collaborators at the IBM Almaden Research Center. Tung J. Chuang and Haj Seki have provided incredible support for these experiments, which otherwise would not have been possible. Their approachability has made for continued interesting and enjoyable conversation. All I can say is... "Please buy IBM!"

I thank Prof. Jing Zhang, a wonderful person, for helping me with the OPA/DFG design and for continued enjoyable e-mail conversations.

I thank Prof. Steven Louie and Xavier Blase for the collaboration on the CH vibrational anharmonicity and two-phonon bound state paper. We *will* finally get that paper through!

I thank Vessi Petrova-Koch for her enthusiastic charm and recent collaborations introducing me to the world of porous silicon and in general, nanocrystallites. Wow! ... It's overwhelming to start so many new and exciting projects and papers.

To the dissertation committee, Y.R Shen, P. Alivisatos, and P. Yu, thank you for reading this dissertation in times of such immediate deadlines.

Thanks to the Graduate Division for a second "filing status" for which I am extremely grateful.

On a personal note, I would like to thank my good friends for having made life over the last few years more enjoyable and productive. To my friends, John Davis, Eric Klementis, Dieter Wilk, Tom Moses, Tony & Loni Peurrung, Mike McCluskey, Don Saito, and Paul Cremer ... thanks a bunch for the memories of late-night Star Trek marathons, ice cream at Fentons, ski trips, camping trips, hang gliding trips, musicals, and dinner parties. To my non-scientist friends, thanks for putting up with some of our

"shop-talk". Thanks Mike, for helping me put together this computer from complete scratch.

I would like to thank the hang gliding community at large, the United States Hang Gliding Association (USHGA), the UC Berkeley Hang Gliding Club, the Marin County Hang Gliding Association, and the Wings of Rogallo with all of its diverse members for having enriched my life so tremendously. ...Yes, after this I will (again) fix the weather machine ("Herb") and so KTVU doesn't report 150 MPH gusts on top of Mt. Tam. ...And for those of you wondering, ... No, I don't skydive or bungie-jump ... now *that's* crazy. ... But ... , hang gliders are real aircraft (try going to >17,000 ft. in a Cessna!) ... You say too much hang gliding on the brain? ... we continue ...

To my relatives, thanks for holding onto those graduation presents for so long.

To my wonderful parents, Jean and Hamlet Chin, thank you for your love, patience, and support, both emotional and financial, these 13 years from home. I promise to have a real job soon.

To my twin brother, Roger, thanks. Learning from your experiences and sacrifices has helped me finish here at Berkeley.

As a final note, I acknowledge the four years of financial support by the Natural Sciences and Engineering Research Council (NSERC) of Canada under the prestigious "1967 (Centennial) Scholarship" which enabled me to come to UC Berkeley. In addition, I thank the generous support of an IBM Pre-doctoral fellowship.

Table of Contents

	Page
I. Introduction	1
References	5
II. Infrared-Visible Sum Frequency Generation and Second Harmonic Generation	7
A. Theory	8
A.1. Nonlinear Susceptibility in Second Order Nonlinear Processes	8
A.2. Second Harmonic Generation Nonlinear Response	9
A.3. Infrared-Visible Sum Frequency Generation Surface Nonlinear Susceptibility	11
A.4. (Microscopic) Nonlinear Molecular Polarizability	13
A.5. Output Radiation from the Induced Polarization	15
A.6. Higher-Order Multipole Bulk Contributions	18
B. Experiment	19
References	24
Figures	26
III. Interaction of Hydrogen with the Diamond C(111) Surface	30
A. Introduction	30
B. Second Harmonic Generation and Sum Frequency Generation	33
C. Experimental Apparatus and Sample Preparation	36
D. Experimental Results	39
D.1. Hydrogen Terminated Surface C(111)-(1x1)-H	39
D.2. Temperature Dependence of the CH Stretch Frequencies and Linewidths	41

D.3. Adsorption, Desorption, and Abstraction of Hydrogen 42

D.4. Determination of the Kinetic Parameters for Thermal Desorption of Hydrogen 46

D.5. The Reconstructed C(111)-(2x1) Surface 48

E. Discussion 50

E.1. Hydrogen Adsorption, Desorption, and Abstraction on the C(111) Surface 50

E.2. The Reconstructed Surface 54

F. Conclusion 56

References 57

Figures 61

IV. Anharmonicity and Lifetime of the CH Stretch Mode on Diamond H/C(111)-(1x1) 76

A. Introduction 76

B. Experiment 78

C. Anharmonicity and Lifetime Determination 78

D. Discussion 82

E. Conclusion 84

References 85

Tables 87

Figures 88

V. Interaction of Methyl Radicals with the Diamond C(111) Surface 93

A. Introduction 93

B. SFG Vibrational Signature of a Methyl Termination 95

C. Experiment 97

D. Methyl Radical Adsorption and Decomposition 99

E. Coadsorption by Activated Hydrogen or Methane 104

F. Discussion 105

G. Conclusion 107

References 108

Figures 110

VI. Interaction of Hydrogen with the Diamond C(100) Surface 119

A. Introduction 119

B. Experiment 120

C. Results 120

D. Discussion 122

References 123

Figures 124

VII. Conclusion and Extensions 127

Appendix A: Widely Tunable OPG/OPA/DFG Infrared System 129

Appendix B: Assorted Infrared SFG Spectra for Different Bond Types 136

Figures 137

I. Introduction

For many decades, diamond has been viewed as a precious gem with remarkable physical and chemical qualities.[1] When one talks of diamond growth, images of machinery capable of simulating Mother Nature's high temperatures and pressures are envisioned. Indeed diamond can be synthesized in this manner[2], but recently, diamond and diamond-like carbon (DLC) films were found to grow under low pressure conditions using chemical vapor deposition (CVD) techniques.[3] These CVD techniques all involve gases at low pressures (~50 torr) consisting of mostly hydrogen (99 %) and a hydrocarbon source such as methane, ethane, ethylene, etc. This ambient is then activated to produce reactive radicals by a variety of methods: thermal (hot filament), electron bombardment, and variations of plasma generation such as by microwave, RF, and DC excitation. These reactive species now facilitate the diamond growth process upon various substrates.

The subject of synthesized CVD diamond growth has created great excitment in the scientific and industrial communities. The potential applications for CVD diamond exploiting diamond's unique properties are vast.[4] Because they are hard and chemically inert, they would be ideal as protective coatings. Its high thermal conductivity makes them efficient heat spreaders and can efficiently dissipate heat from electronic devices. Because of its very wide optical transparency, they can be used as windows which span the far-infrared through to the ultraviolet spectrum. In addition, there is the potential for diamond-based electronic devices. As conventional transistors[5] they can operate at high temperatures due to the large bandgap. Under certain circumstances, the diamond surface can exhibit a "negative" electron affinity (NEA)[6] to efficiently emit electrons as "cold cathodes" in emissive-type devices.

Diamond's bulk properties have been known since the start of the seventeenth century where it was discovered to be composed of carbon (Averani and Targioni). It was

not until much later (1912) that its crystal structure was determined by X-ray diffraction (Laue) studies determining the atomic positions (W.H. Bragg and W.L. Bragg). In the 1930's with the increased understanding of chemical bonding and wave mechanics, it was proposed that carbon, through sp^3 hydbridization, would allow tetrahedral bonding to occur. Infrared (IR) studies (Robertson, Fox, and Martin - 1930's), Raman Scattering (Raman - 1927), and continued X-Ray studies (K. Lonsdale - 1945) deduced the diamond structure to be face-centered cubic (FCC) with a two atom basis and having covalent sp^3 tetrahedral bonding between carbon atoms.

It wasn't until more recently that surface studies were performed on diamond. The adsorption of various gases on diamond powders were performed by Sappok and Boehm[7] (1968). Both physical adsorption and chemical adsorption were performed. It was found that for gases such as H_2, O_2, N_2, Cl_2, F_2, and Br_2 at elevated temperatures, irreversible adsorption onto the diamond surface occurred. Infrared spectroscopic studies (Eischens[8] (1972), Thomas[9] (1975)) on powders later confirmed this.

Single face crystal studies started as early as 1962 by Marsh *et al.* Later, Lander and Morrison[10] (1966) successfully observed the (111) surface patterns using Low Energy Electron Diffraction (LEED). They were able to observe the surface in the bulk geometry and the surface reconstruction upon heating. Later, Lurie and Wilson[11] (1977) used more standard surface spectroscopic techniques such as LEED, Auger Spectroscopy, and Electron Energy Loss Spectroscopy (EELS) to study several diamond specimens. The first direct evidence of hydrogen termination was found by Waclawski *et al.*[12] (1982) using High Resolution Electron Energy Loss Spectroscopy (HREELS). With the explosion of recent techniques[13] for surface studies, a plethora of experimental and accompanying theoretical diamond surface studies ensued, propelled by commercial interests in CVD diamond. This was also fueled by parallel efforts with other group IV

elements, such as Ge and the much studied Si. The relevant details, discussion, and background references are later presented within each chapter.

A more versatile spectroscopic technique would be needed to fulfill the requirement of the ongoing fundamental and applied studies of the diamond growth process. An optical spectroscopy would be ideal as it can provide in-situ analysis, high spectral resolution, and time resolution for dynamic studies. For the diamond surface, this need can be fulfilled using the novel surface-sensitive nonlinear optical spectroscopies of Second Harmonic Generation (SHG) and Infrared-Visible Sum Frequency Generation (SFG).[14]

SHG and SFG have been shown to be versatile probes to study a variety of interfaces with submonolayer sensitivity. Using SFG vibrational spectra,[15] one can deduce the presence and orientation of chemical species occupying the surface. For the study of diamond surfaces, SFG is particularly useful because few other techniques are available, especially when the experiments need to be performed under ultra-high vacuum (UHV) conditions.

In this article, the surface of natural diamond is studied by nonlinear optical spectroscopy (SHG and SFG). As mentioned above, the presence of hydrogen as the dominant gas species in CVD diamond growth is crucial. It is also believed that methyl radicals may be an important prerequisite for growth on (111), (100), and (110) principle planes. Our work here reflects these thoughts. In Chapter II, the basic theoretical and practical aspects of the SHG and SFG techniques are discussed. Chapter III, containing the majority of this work describes the interaction of hydrogen with the diamond C(111) surface. Furthermore, the bare surface and its surface reconstruction are explored. Chapter IV examines the more fundamental aspects of the CH bond on the fully hydrogenated C(111) surface. The CH bond anharmoncity and time-resolved vibrational dynamics are investigated using a pump and probe experiment. In Chapter V, we go

beyond atomic hydrogen to investigate the interaction of methyl radicals with the diamond C(111) surface. In Chapter VI, we go on to briefly investigate the diamond C(100) surface with hydrogen termination. Final closing remarks are made in Chapter VII.

References

1. J.E. Field, ed., *The Properties of Diamond* (Academic Press, San Francisco, 1979).
2. S. Vagarali, M. Lee, R.C. DeVries, Journal of Hard Materials, **1**, 233 (1990) and references therein.

   H.M. Strong, American Journal of Physics, **57**, 794, (1989) and references therein.
3. R. C. DeVries, Ann. Rev. Mater. Sci. **17**, 161 (1987).

   J. C. Angus and C. C. Hayman, Sci. **241**, 913 (1988).

   K. E. Spear, J. Am. Ceram. Soc. **72**, 171 (1989).
4. P. Bachmann, Physics World, **4**, 32 (1991) and references therein.
5. M.W. Geis, J.C. Angus, Scientific American (International Edition), **267**, 64 (1992).

   R.J. Trew, J.B. Yan, P.M. Mock, Proceeding of the IEEE, **79**, 598 (1991).
6. J. Van der Weide *et al.*, Phys. Rev. B, **50**, 5803 (1994) and references therein.
7. R. Sappok and H.P. Boehm, Carbon, **6**, 283 (1968).

   R. Sappok and H.P. Boehm, Carbon, **6**, 573 (1968).
8. R.P. Eischens, Accounts Chem. Res., **5**, 74 (1972).
9. J.M. Thomas and E.L. Evans, Suppl., Ind. Diam. Rev., 2 (1975) and references therein.
10. J.J. Lander and J. Morrison, Surf. Sci., **4**, 241 (1966).
11. P.G. Lurie and J.M. Wilson, Surf. Sci., **65**, 453 (1977).

    P.G. Lurie and J.M. Wilson, Surf. Sci., **65**, 476 (1977).

    P.G. Lurie and J.M. Wilson, Surf. Sci., **65**, 499 (1977).
12. B. J. Waclawski, D. T. Pierce, N. Swanson, and R. J. Celotta, J. Vacuum Sci. Technol. **21**, 368 (1982).
13. G.A. Somorjai, *Principles of Surface Chemistry* (Prentice-Hall, New Jersey, 1972).

G.A. Somorjai, *Chemistry in Two Dimensions: Surfaces* (Cornell University Press, Ithaca, 1981).

G.A. Somorjai, *Introduction to Surface Chemistry and Catalysis* (1994).

H. Ibach and D.L. Mill, *Electron Energy Loss Spectroscopy and Surface Vibrations* (Academic, New York, 1982).

A. Zangwill, *Physics at Surfaces* (Cambridge University Press, 1988).

A.W. Adamson, *Physical Chemistry of Surfaces* (Wiley, New York, 1990).

14. Y.R. Shen, Surface Science, **299/300**, 551 (1994) and references therein.

Y.R. Shen, Nature (London), **337**, 519 (1989) and references therein.

15. G. Herzberg, *Infrared and Raman Spectra of Polyatomic Molecules* (Van Nostrand, Princeton, NJ, 1945).

R.F. Willis, ed., *Vibrational Spectroscopy of Adsorbates*, Springer Series in Chemical Physics, Volume 15 (Springer, Berlin, 1980).

N.B. Colthup, L.H. Daly, and S.E. Wiberley, *Introduction to Infrared and Raman Spectroscopy* (Academic, New York, 1990).

II. Infrared-Visible Sum Frequency Generation & Second Harmonic Generation

For probing interfaces and surfaces with high sensitivity, techniques are needed where the surface signal can dominate over that of the bulk. Second order nonlinear optical spectroscopies of second harmonic generation (SHG) and sum frequency generation (SFG) satisfy this need because by symmetry, the processes are forbidden in a bulk medium with inversion symmetry but necessarily allowed at its surface.[1,2] Being optical techniques, they can be applied *in-situ* to any surface or interface accessible by light. This includes harsh environment conditions such as within a high pressure reactive chamber where all particle spectroscopies would fail.

The first experiments involving SHG showed excellent surface sensitivity with submonolayer resolution. Visible or near-infrared lasers were used in which the second harmonic signal was in the visible or ultraviolet range. This signal was then easily detected using sensitive photomultiplier tubes and photon counting techniques. This technique had the usefulness of characterizing the coverage and nature of the adsorption, desorption, or reaction processes at surfaces. It is also able to observe surface changes such as due to reconstruction or phase transitions.[3] However, resonant excitation often involves broad electronic transitions that may not be sufficiently resolved for uniquely identifying surface species. Ideally, one could use a vibrational spectroscopy which has the selectivity for identifying particular surface species. However, SHG using the necessary mid-infrared or far-infrared light would have its SHG signal in the infrared where detectors lack sufficient sensitivity. Fortunately, one can still use the general principle with vibrational selectivity by using infrared-visible sum frequency generation (SFG) spectroscopy.[1]

In the case of infrared-visible SFG spectroscopy, a tunable infrared beam is used to vibrationally probe surface species while the visible light "up-converts" the signal into the

visible range where the photomultiplier tubes are sensitive. This then allows the technique to exhibit submonolayer surface sensitivity to a particular surface species. The first successful experimental demonstration of infrared-visible SFG for vibrational spectroscopy was by X.D. Zhu *et al.* in 1987.[4] This initiated popularization of the vibrational technique for studying surface species at interfaces.

In this chapter, the basic theory of SHG and SFG is discussed as it applies to the study of the diamond surface and related systems. Details involving a particular analysis are presented individually within the relevant chapters.

A. Theory

A.1. Nonlinear Susceptibility in Second Order Nonlinear Processes

Both second harmonic generation (SHG) and sum frequency generation (SFG) can be described as three-wave mixing processes.[1] In both processes, two input electric fields interact with media to produce an output signal having a frequency that is the sum of the input fields. In SFG, the two input fields are taken to be different in frequency (ω_1, ω_2) which results in an output signal with a frequency of $\omega_{SF} = \omega_1 + \omega_2$. In the case of SHG, the input fields are degenerate to produce an output field with a frequency at the second harmonic (2ω).

For the following discussion, the two input fields are taken to be of the form: $\vec{E}(\omega_j, t) = \vec{E}_j \exp(-i\omega_j t) + \vec{E}_j^* \exp(i\omega_j t)$ where $j = 1,2$. In the electric dipole approximation, the induced polarization $\vec{P}(\omega_s)$ of the medium is given by:[1,2,5]

$$\vec{P}(\omega_s = \omega_1 + \omega_2) = \vec{\chi}_D^{(2)} : \vec{E}(\omega_1)\,\vec{E}(\omega_2)$$
$$P_i(\omega_s = \omega_1 + \omega_2) = \chi_{D,ijk}^{(2)}\, E_j(\omega_1)\, E_k(\omega_2) \qquad (2.1)$$

where $\vec{\chi}_D^{(2)}$ represents the second order susceptibility tensor in the medium in the dipole approximation limit. By symmetry, the susceptibility tensor belongs to the group reflecting the symmetry of the medium or interface. One can see that for bulk media with complete inversion symmtery (centrosymmetric) $\vec{\chi}_{D,Bulk}^{(2)} = 0$ for all tensor components as Eqn. 2.1 must be invariant under the inversion operation. However, at the surface, the inversion symmetry is broken so $\vec{\chi}_{D,Surface}^{(2)} \neq 0$ which gives second order nonlinear processes a high degree of surface specificity. Depending on the surface's symmetry, many terms of the surface susceptibility, $\vec{\chi}_{D,Surface}^{(2)}$ may vanish.

For bulk media without inversion symmetry but with some degrees of rotational symmetry some of the $\vec{\chi}_{D,Bulk}^{(2)}$ components may still vanish. This can be determined by symmetry operations which render Eqn. 2.1 invariant.

So far, only the polarization induced in the electric dipole approximation is considered. However, there may be singnificant higher-order (multipole) contributions which are allowed no matter what the bulk symmetry is. This will be discussed later.

A.2. Second Harmonic Generation Nonlinear Response

As mentioned above, SHG is very useful as an *in-situ* monitor of processes occurring in real-time, particularly for monitoring some physical modification of the surface. Resonant responses of SHG from the near-infrared to the ultraviolet generally

come from broad electronic resonances. Changes in the surface electronic responses by processes such as adsorption (physisorption or chemisorption) readily affect both resonant and nonresonant SHG. The overall surface susceptibility observed often consists of several contributions. For adsorption / desorption of molecules on a surface,[11] for example, we have

$$\vec{\chi}^{(2)}_{D,Surface} = \vec{\chi}_{ind} + \vec{\chi}_{int}(\Theta) + \vec{\chi}_{ads}(\Theta) \tag{2.2}$$

where Θ is the adsorbate coverage and $\vec{\chi}_{ind}$, $\vec{\chi}_{int}(\Theta)$, $\vec{\chi}_{ads}(\Theta)$ represents contributions from a bare surface, adsorbate-substrate interaction, and molecular adsorbates, respectively. Of course, a similar separation of the susceptibility contributions for other processes such as surface phase transitions may have terms dependent on the azimuthal angle, etc.

Unfortunately, the separate terms contribute to $\vec{\chi}^{(2)}_{D,Surface}$ with their own particular amplitude and phase with the result that the total response is a non-monotonic function of the adsorbate coverage. Moreover, since more than one kind of adsorbate may be present, the results are generally not easily interpreted unless the system is simple as confirmed by other supporting analytical techniques. As seen in chapter III, this problem is circumvented by the specificity of the SFG technique to identify the coverage of a single type of adsorbate.

If one has an isotropic surface, the number of tensor components in the susceptibility is small which can minimize the ambiguity stated above. For this isotropic surface, the contributing tensor components are:

$$\chi^{(2)}_{xxz} = \chi^{(2)}_{yyz}, \quad \chi^{(2)}_{zxx} = \chi^{(2)}_{zyy}, \quad \chi^{(2)}_{zzz} \tag{2.3}$$

where the x-z plane is the plane of incidence of the optical beams, z is the surface normal, and y is perpendicular to the plane of incidence along the surface. This is the convention that will be used throughout this thesis.

For an appropriate choice of input and output polarizations, a selected response of the corresponding susceptibility tensor terms is obtained. For p-in and p-out, the $\chi^{(2)}_{xxz}$, $\chi^{(2)}_{zxx}$, and $\chi^{(2)}_{zzz}$ terms are probed which may independently change with surface modifications and exhibit a complicated response due to the interference of the contributing terms. A better polarization combination is one that probes only a single tensor component, hopefully one that has good sensitivity to the experiment. The s-in and p-out polarization combination is the more logical choice probing only the $\chi^{(2)}_{zyy}$ term. An example is shown in chapter III with the resulting SHG response being easier to interpret in a complicated surface modification experiment.

If a surface of lower symmetry occurs, more surface tensor components remain nonvanishing and may contribute to the signal. In a more difficult situation, if the bulk is noncentrosymmetric, the appropriate choice of the polarization combination becomes even more critical in order to have even some degree of surface specificity. An example of this was for GaAs whose bulk symmetry is $\bar{4}3m$ and hence has a non-vanishing bulk susceptibility. In this case, surface sensitivity is possible by careful geometrical choices of the light polarization and surface orientations.[6]

A.3. Infrared-Visible Sum Frequency Generation Surface Nonlinear Susceptibility

In describing infrared-visible SFG, the formalism given shall apply to molecular species which are situated at an interface. In this case, the macroscopic surface

susceptibility $\vec{\chi}^{(2)}_{D,Surface} = \chi^{(2)}_{ijk}$ (where the extra indices have been dropped for brevity) can be related to the microscopic molecular polarizability, $\vec{\alpha}^{(2)}_{lmn,Q}$ by:

$$\chi^{(2)}_{ijk} = \sum_{Q} \chi^{(2)}_{ijk,Q} = \sum_{Q} N_{s,Q} \sum_{lmn} \left\langle (\hat{i}\cdot\hat{I})(\hat{j}\cdot\hat{m})(\hat{k}\cdot\hat{n}) \right\rangle \alpha^{(2)}_{lmn,Q} \tag{2.4}$$

where $N_{s,Q}$ represents the surface density of the species Q and the angular bracketed term denotes the molecular reference frame to the macroscopic lab frame coordinate transformation averaged over the molecular orientation distribution. From here forward, the indices ijk (or lmn) shall refer to the sum-frequency, the visible, and the infrared components, respectively. Although one can have a situation where the bulk contribution vanishes, by no means is the symmetry breaking limited to just a single monolayer at the interface as the wavelength of light enables a macroscopic contribution of several layers to be probed. In this case, Eqn. 2.4 is modified to include a macroscopic thickness in the z-direction:[7]

$$\chi^{(2)}_{ijk,Q} = \int_{z} \chi^{(2)}_{ijk,Q}\, dz = \langle n_Q \rangle N_{s,Q} \sum_{lmn} \left\langle (\hat{i}\cdot\hat{I})(\hat{j}\cdot\hat{m})(\hat{k}\cdot\hat{n}) \right\rangle \alpha^{(2)}_{lmn,Q} \tag{2.5}$$

where $\langle n_Q \rangle$ denotes the average number of layers or effective thickness of the contributing molecular film. Because of the limitations of separating the contributing effects to the overall response, $N_{s,Q}$, $\langle n_Q \rangle$, or $\left\langle (\hat{i}\cdot\hat{I})(\hat{j}\cdot\hat{m})(\hat{k}\cdot\hat{n}) \right\rangle$ cannot be determined uniquely. However, since in many systems only one monolayer is expected to occur,

$\langle n_Q \rangle \approx 1$ ML. Still one has to separate the relative contribution of the species surface density to the orientational average. As seen later, one may determine an average orientation of the surface species by measuring different components of the susceptibility tensor which must share the same orientational information. However, the general task of determining the absolute surface density and the orientational distribution remains difficult in all but the simplest systems.

A.4. (Microscopic) Nonlinear Molecular Polarizability

Here, the description of the origin of the microscopic susceptibility leading to the nonlinear response of a molecular species is described from second order perturbation theory.[8] The molecular susceptibility, $\tilde{\alpha}^{(2)}_{lmn,Q} = \tilde{\alpha}^{(2),NR}_{lmn,Q} + \tilde{\alpha}^{(2),R}_{lmn,Q}$, can be broken into two contributing terms, a non-resonant term, $\tilde{\alpha}^{(2),NR}_{lmn,Q}$ and a resonant term, $\tilde{\alpha}^{(2),R}_{lmn,Q}$. The resonant term is given by:[2]

$$\tilde{\alpha}^{(2),R}_{lmn,Q}(\omega_s) = \frac{1}{\hbar}\sum_{v}\sum_{v'}\left[\frac{\hat{\rho}_{gv',gv}\langle\psi_{gv'}|\mu_n|\psi_{gv}\rangle}{(\omega_{gv',gv}-\omega_{IR})-i\Gamma_{gv',gv}}\right]_Q \langle\psi_{gv}|\alpha^{(1)}_{lm}|\psi_{gv'}\rangle$$

$$= \frac{1}{\hbar}\sum_{v}\sum_{v'}\left[\frac{\hat{\rho}_{gv',gv}\langle\psi_{gv'}|\mu_n|\psi_{gv}\rangle}{(\omega_{gv',gv}-\omega_{IR})-i\Gamma_{gv',gv}}\right]_Q M_{lm} \qquad (2.6)$$

where

$$M_{lm} = \sum_{p}\left[\frac{\langle\psi_{gv}|\mu_l|\psi_p\rangle\langle\psi_p|\mu_m|\psi_{gv'}\rangle}{(\omega_{p,gv'}-\omega_{SF})} - \frac{\langle\psi_{gv'}|\mu_l|\psi_p\rangle\langle\psi_p|\mu_m|\psi_{gv}\rangle}{(\omega_{p,gv}+\omega_{SF})}\right]$$

where g represents the ground electronic state; v is the initial vibrational state; v' is the final vibrational state; $\hat{\rho}$ is the density matrix; $\langle \psi_{gv'} | \mu_n | \psi_{gv} \rangle$ is the electric infrared dipole transition matrix element from the ψ_{gv} to $\psi_{gv'}$ state; $\omega_{gv',gv} = (E_{gv'} - E_{gv})/\hbar$ is the vibrational frequency for the state energy difference between the gv state (E_{gv}) and the gv' state ($E_{gv'}$); $\Gamma_{gv',gv}$ is the phenomenological damping constant of the gv to gv' transition; $\alpha_{lm}^{(1)}$ is polarizability tensor; and ω_{IR} is the incident (infrared) laser field frequency; M_{lm} is the Raman matrix element describing the transitions between ψ_{gv} and $\psi_{gv'}$ through intermediate states ψ_p; and $\omega_{p,gv}$ is the frequency associated with the transition from the ψ_{gv} state to the ψ_p state; and ω_{SF} is the sum frequency.

The process can be described as the coupling of the incident ω_{IR} field to the infrared dipole transition which then is up-converted by the Raman process described by the Raman matrix, M_{lm}.

If one has conditions where the fundamental transitions (Q) are primarily excited and electronic resonances are sufficiently far away, then the following results:[9]

$$\alpha_{lmn}^{(2),R} = \sum_{Q} \frac{\Delta\rho_{Qg}\,\vec{A}_Q}{(\omega_Q - \omega_{IR} - i\Gamma_Q)} \quad \text{where} \quad \vec{A}_Q = \frac{1}{2\omega_Q}\frac{\partial\mu_n}{\partial q}\frac{\partial\alpha_{lm}^{(1)}}{\partial q} \qquad (2.7)$$

$\Delta\rho_{Qg}$ is the population difference between the ground and first-excited vibrational state Q, $\frac{\partial\mu_n}{\partial q}$ is the infrared dipole moment derivative, and $\frac{\partial\alpha_{lm}^{(1)}}{\partial q}$ is the Raman polarizability for the particular vibrational mode Q with respect to the normal coordinate q. A particularly important result of the above equation is that it provides the selection rules for the infrared-visible SFG process; namely, that it must be *both* infrared and Raman active. By symmetry considerations, only molecular groups lacking

centrosymmetry can be both infrared and Raman active[10], thereby being able to be detected with the SFG technique. Generally, since these chemical groups / molecules are observed at interfaces, this condition is almost always satisfied.

As $\omega_{IR} \rightarrow \omega_{gv',gv} = \omega_Q$, there is a vibrational enhancement in the sum-frequency spectrum giving a characteristic signature of the vibrational mode. Since the overall microscopic susceptibility term has the contribution of a non-resonant term which is added (with a phase) to the resonant term, the resulting spectrum may be significantly distorted from what would normally be a Lorentzian lineshape peak as for a linear IR spectrum. In some cases, the vibrational feature may appear as a dip upon a non-resonant background. In addition, as seen later, if the intrinsic lineshape is sharper than the characteristic linewidth of the laser infrared source, a "Voigt"-like lineshape results. In this case, the vibrational feature's central peak exhibits gaussian-like behavior but away from resonance, Lorentzian-like behavior ("wings") is seen. Obviously, if this is the case, the laser infrared linewidth must be deconvoluted from the spectra to obtain the true vibrational signature.

A.5. Output Radiation from the Induced Polarization

To predict the SFG signal detected, the output radiation field resulting from the induced polarization by the nonlinear process must be calculated. Initiating the process are two input fields impinging upon an interfacial region with an effective dielectric constant, $\varepsilon'(\omega_j)$ between medium 1 into medium 2. The optical field $\bar{E}_{SF}$ produced by the nonlinear macroscopic susceptibility, $\chi_s^{(2)}$, emitted back into medium 1 is given by:

$$\bar{E}_{SF} = \frac{2\pi i\,\omega_{SF}\sec(\Theta_{SF})}{c\sqrt{\varepsilon_1(\omega_{SF})}}\left(\bar{L}_{SF}\cdot\hat{e}_{SF}\;\vec{\chi}^{(2)}:\bar{L}_V\cdot\hat{e}_V\;\bar{L}_{IR}\cdot\hat{e}_{IR}\right)\times E_V\,E_{IR}\exp\left(i\,\bar{k}_1(\omega_{SF})\cdot\bar{r}-i\,\omega_{SF}t\right) \tag{2.8}$$

Here, $\hat{e}_{j=SF,V,IR}$ and $E_{j=SF,V,IR}$ are the unit vectors and amplitudes for the electric fields, respectively, $\varepsilon_1(\omega_{SF})$ is the dielectric constant in medium 1 for the sum-frequency beam, Θ_{SF} is the angle from the normal at which the output sum-frequency wavevector $\bar{k}_1(\omega_{SF})$ is radiated. These are determined by the phase-matching condition, $k_{SF,x} = k_{V,x} + k_{IR,x}$ where the parallel components of the wavevector along the interface (x-direction) are conserved. $\bar{L}_{j=SF,V,IR}$ are the Fresnel factors which relate the electric field strength in medium 1 to that within the interfacial region with dielectric constant ε' in which the nonlinear interaction takes place:[1,2]

$$\begin{aligned} L_{xx} &= \frac{2\varepsilon_1 k_{2z}}{\varepsilon_2 k_{1z} + \varepsilon_1 k_{2z}} \\ L_{yy} &= \frac{2k_{1z}}{k_{1z} + k_{2z}} \\ L_{zz} &= \frac{2\varepsilon_1 k_{1z}}{\varepsilon_2 k_{1z} + \varepsilon_1 k_{2z}}\left(\frac{\varepsilon_2}{\varepsilon'}\right) \end{aligned} \tag{2.9}$$

for which all components are evaluated for the appropriate field frequency.

The output field given by Eqn. 2.8 then enables the calculation of the SFG signal for the conditions of the experiment. For input beams with energies U_V and U_{IR} contained within an effective temporal overlap pulse duration, T, and spatial overlap area, A, the SFG signal produced is:[1,2]

$$S_{photons}(\omega_{SF}) = \frac{8\pi^2 \omega_{SF} \sec^2(\Theta_{SF})}{\hbar c^3 \sqrt{(\varepsilon_1(\omega_{SF})\varepsilon_1(\omega_V)\varepsilon_1(\omega_{IR}))}} \times \left| \bar{L}_{SF} \cdot \hat{e}_{SF} \, \tilde{\chi}^{(2)} : \bar{L}_V \cdot \hat{e}_V \; \bar{L}_{IR} \cdot \hat{e}_{IR} \right|^2 \frac{U_V U_{IR}}{AT} \tag{2.10}$$

The estimated SFG signal attainable with the laser system used for the diamond experiments have the following parameters. Laser pulses have energy 0.5 mJ for the 0.532 μm visible beam, 0.4 mJ for the infrared, a 20 psec temporal overlap, and a 0.4 mm diameter spatial overlap. The incident input and reflected output beam angles are approximately 45° which yield Fresnel factors on the order of unity for dielectric surfaces.

For an estimate of $\chi^{(2)}$, a momentary digression is needed. From the literature, the resonant molecular polarizability:[11]

$$\alpha^{(2),R} = \frac{c^2}{\hbar \sqrt{\omega_{SF} \omega_V^3}} \frac{\mu_Q}{\Gamma_Q} \sqrt{\frac{d\sigma}{d\Omega}} \tag{2.11}$$

can be determined knowing the infrared dipole transition moment[12] μ_Q, the differential Raman cross-section[13] $\frac{d\sigma}{d\Omega}$, and the linewidth Γ_Q of the vibrational mode $\omega_Q = \omega_{SF} - \omega_V$. From assorted references, the symmetric stretch vibration of a CH_3 group: $\mu_Q \approx 0.05\,D$ (1 Debye $= 10^{-18}$ esu), $\frac{d\sigma}{d\Omega} \approx 5 \times 10^{-30}$ cm^2/sr, $\Gamma_Q \approx 10$ cm^{-1}, $\omega_Q \approx 2875$ cm^{-1} giving $\omega_{SF} \approx 4.0 \times 10^{15}$ s^{-1} for $\omega_V \approx 3.5 \times 10^{15}$ s^{-1} (532 nm). A typical monolayer (Langmuir film) of fatty acid molecules on water containing these CH_3 tail

groups is $N_S \approx 5 \times 10^{14}$ cm^{-2}. The overall susceptibility of the layer is then $\chi^{(2),R} = N_S \alpha^{(2),R} \approx 10^{-15}$ esu.

From the above numerical values, an estimated ~$4x10^4$ photons per pulse results. The detection efficiency is ~5 % which still yields ~2000 photons detected. With a background dark count of < 0.001 photon counts per pulse from photomultiplier tubes, this is a more than adequate signal (S/N ~ 10^6) to detect < 1 % ML coverage. However, as discussed later, this may be difficult to achieve.

A.6. Higher-Order Multipole Bulk Contributions

As mentioned above, there can be significant contributions related to the bulk medium as it breaks the symmetry near the surface. Discontinuities of the fields and the nonlinear susceptibility at the interface force us to consider the higher-order multipole contributions to the SHG and SFG signals.[7,14,15]

In addition, resonances within the bulk media might have to be considered as the surface and the bulk may consist of similarly close resonances, whether or not they have similar chemical make-ups. An example would be a liquid surface in which the surface might be distiguished by an increased ordering with only a slight resonance frequency shift compared with the disordered (isotropic) bulk. In this article, the latter case was not encountered, but there was a case where the surface species vibrational frequency (CH bend) was close to bulk TO phonon resonances of diamond. Fortunately, as shall be shown in chapter III, these bulk resonances do not express themselves and are of no concern. Eqn. 2.1 can be expanded beyond the dipole term to include higher-order derivatives of the applied electric and magnetic fields:[14]

$$\vec{P}^{(2)} = P^{(2)} - \nabla \cdot \vec{Q}^{(2)} + \frac{c}{i\omega_s} \nabla \times \vec{M}^{(2)} + \quad \text{(higher - order terms)} \tag{2.12}$$

$$\begin{aligned} \vec{P}^{(2)} &= \vec{\chi}_D : \vec{E}_1 \vec{E}_2 + \vec{\chi}_{P_1} : \nabla \vec{E}_1 \vec{E}_2 + \vec{\chi}_{P_2} : \vec{E}_1 \nabla \vec{E}_2 \\ \vec{Q}^{(2)} &= \vec{\chi}_Q : \vec{E}_1 \vec{E}_2 \\ \vec{M}^{(2)} &= \vec{\chi}_M : \vec{E}_1 \vec{E}_2 \end{aligned} \tag{2.13}$$

where $\vec{P}, \vec{Q}, \vec{M}$ are the electric-dipole, electric-quadrupole, and magnetic dipole contributions. The $\vec{\chi}_D$ term in the electric dipole contribution is what is normally considered surface dominant. But, the $\vec{\chi}_{p_1}, \vec{\chi}_{p_2}, \vec{\chi}_Q$, and $\vec{\chi}_M$ are seen here to be nonvanishing for *any* crystal symmetry.

Since the scope of the experiments within this article do not invite a detailed analysis of the above mentioned bulk contributions, the discussion here of higher bulk contributions is not pursued further.

B. Experiment

In this section, the practical aspects relating to the SHG and SFG experiments are described. Details of the SHG / SFG system is described starting from the laser through to the detection system.

The power source of the system is an active-passive mode-locked Nd:YAG laser capable of producing 25 psec, ~40 mJ/pulse (#5 dye) or 35 psec, ~60 mJ/pulse (#9740 dye) with a 20 Hz repetition rate. The stability of the output at 1.064 μm is < 6 % rms shot-to-shot fluctuations.[16]

A KD^*P SHG generator produced the 532 nm green beam for the SHG or SFG up-conversion. For the infrared source, two sources of greatly different designs provided the tunable infrared light necessary for the infrared-visible SFG experiments. The first original infrared source was a $LiNbO_3$ optical parametric generator (OPG) and amplifier (OPA)[17]. The tuning range of this infrared source was from 2600 cm^{-1} to 4000 cm^{-1}, with linewidths of ~10 cm^{-1} to 50 cm^{-1}, respectively. The pulse energy is typically 400 μJ (#5 dye) or 600 μJ (#9740 dye). The second, much more sophisticated infrared generator (Fig. 2) was composed of two stages[18]. Green (532 nm) light generated in a temperature-tuned LBO crystal provided the pump for a Beta-Barium Borate (BBO) double-pass OPG / OPA stage incorporating a line-narrowing grating element reducing the linewidth of this stage to ~2 cm^{-1}. The output of this stage (700 - 2200 nm) contained the signal beam (< 1064 nm) and idler beam (> 1064 nm). The latter was then used to mix with a 1064 nm pump within a $LiNbO_3$ crystal to produce a difference frequency generation (DFG), narrow linewidth (~4 cm^{-1}) output similar in frequency range as the first infrared source except with ~200 μJ energy and 8 psec pulsewidth, (#5 dye). If a silver gallium sulfide ($AgGaS_2$) crystal was used instead, the range was greatly increased to span further into the far-infrared to the potential 12 μm phase-matching limit. However, due to absorption within the crystal, only a useable output to ~9 μm (1100 cm^{-1}) was possible. Typical energies (#5 dye) for the 8 psec pulses were: ~150 μJ at 2100 cm^{-1}; ~100 μJ at 1800 cm^{-1}; ~50 μJ at 1500 cm^{-1}; and ~40 μJ at 1300 cm^{-1}. The power curve over this large tuning range was shown in Fig. 3. By careful adjustment of the beam parameters, both infrared sources were brought into the saturation regime where the dependency of the output energy on the input energy was minimized. Details of the current system were described in Fig. 2 and Appendix A.

A zinc selenide (ZnSe) double Fresnel rhomb was used as a half-wave retardation device for the infrared beam. However, because of the high reflection losses, only ~45 %

of the energy was transmitted to provide s-polarized excitation. Since s-polarized infrared excitation generally produced weak spectra, a better scheme was used. Using a two-mirror, mutually orthogonal arrangement, the infrared light could change polarization with minimal loss of energy (T > 90 %) or polarization purity. The system was designed to change polarization in either arm reproducibly so that several changes within an experiment was feasible.

The green and the infrared pulses are brought together spatially and temporally using mirrors and delay stages. The visible and infrared beams were near 45° incidence with a 7° beam separation to allow convenient spatial separation of the SFG signal from the SHG and strong visible beam. A half-wave plate, polarizer, half-wave plate arrangement on the visible beam provided easy control of the input energy and the polarization. A telescope arrangement reduced the beam size with control over the convergence so that the reflected focus past the sample would allow easy spatial separation of the SHG / visible beams from the SFG beam. For the infrared beam, a CaF_2 lens (cut-off at ~8.5 μm) with a focal length of 15 cm with the sample near its focus provided imaging of the infrared source output crystal onto the sample. This would help to reduce the spatial displacement resulting from walk-off as the infrared source was tuned so that the overlap with the green beam on the sample remained stable. The green beam diameter was ~0.5 mm and the infrared beam diameter was ~0.3 mm.

The SHG signal along the reflected green beam path was passed through two Corning 7-54 filters each with a transmittance of ~70 % at 266 nm and ~10^{-6} at 532 nm, a Rochon (quartz) polarizer, monochromator, then to the photomultiplier tube (PMT).

The SFG signal was spatially selected and filtered with an iris to exclude as much scattered light since the SFG should be coherent and hence highly collimated and directional. A polarizer, two Raman edge filters (diffracting 532 nm light each with a ~70 % transmission at 460 nm and ~10^{-6} transmission at 532 nm), then a wide bandpass

monochromator to a photomultiplier tube. The use of the monochromator was imperative as the Raman edge filters (or other dielectric filters) had too broad a bandpass to suppress the strong background flourescence. Raman edge filters were crucial to transmit the SFG signal which was spectrally very close to the green (532 nm) light when using the far-infrared source. For the diamond experiment, the background fluorescence was orders of magnitude stronger than the dark count (~0.001 counts / laser pulse) of the PMT's yielding a disappointing ~0.1 photons/pulse background even with substantial spatial filtering. The final S/N ratio was then dominated by the fluctuations in the laser beams and the averaging of laser pulses.[19] For data acquisition with 400 pulses per data point, the maximum signal to background ratio of the spectra was ~200:1 for the strongest diamond signal.

The photomultiplier signals were then sent to gated electronics where the gated signals were recorded with a computer system. The computer also controlled the stepper motors for operating the tunable infrared sources. By photodiode monitoring of key beam parameters, windowing of the data set decreased the contribution from laser fluctuations. Because of the plentiful beam energies, the signals were generally very strong with the output signals out of the photon counting regime. Instead, the majority of spectra were taken with the integrated current from the PMT measured.

As a final discussion, it should be mentioned that assigning the vibration signatures of spectra may present some difficulties in complicated systems. Comparing directly to infrared or Raman spectra which generally represent bulk spectra is somewhat dangerous. The use of all the SFG configurations may be needed to solve some abiguities. Although the SFG technique has extemely good surface sensitivity, the SFG technique tends to have a limited dynamic range due in part to the fact that the signal responds to the square of the dipole transition and the presence of instrumentation noise and laser fluctuations. As in the usual infrared and Raman spectroscopies, the use of different chemical species and

isotopic substitution such as deuteration is commonplace to make assignments. It is the author's wishes that the future users of the technique have the best of luck in this regard.

References

1. Y.R. Shen, Surface Science, **299/300**, 551 (1994) and references therein.

   Y.R. Shen, Nature (London), **337**, 519 (1989) and references therein.

2. Y.R. Shen, The Principles of Nonlinear Optics, (Wiley, New York, 1984).

3. T.F. Heinz, M.M.T. Loy, and W.A. Thompson, Phys. Rev. Lett., **54**, 63 (1985).

4. X.D. Zhu, H. Suhr, and Y.R. Shen, Phys. Rev. B, **35**, 3047 (1987).

5. Y.R. Shen, Ann. Rev. Mat. Sci., 16, 69 (1986); Y.R. Shen, Ann. Rev. Phys. Chem., 40, 327 (1989).

6. T. Stehlin, M. Feller, P. Guyot-Sionnest, and Y.R. Shen, Opt. Lett., **13**, 389 (1988).

   R.W.J. Hollering, Opt. Comm., **90**, 147 (1992).

7. P. Guyot-Sionnest, W. Chen, and Y.R. Shen, Phys. Rev. B, **33**, 8254 (1986).

   P. Guyot-Sionnest and Y.R. Shen, Phys. Rev. B, **35**, 4420 (1987).

8. J.A. Armstrong, N. Bloembergen, J. Ducuing, and P.S. Pershan, Phys. Rev., **127**, 1918 (1962); E. Adler, Phys. Rev., **134**, A728 (1964).

9. R. Superfine, J.Y. Huang, and Y.R. Shen, Opt. Lett., **15**, 1276 (1990).

10. G. Herzberg, *Infrared and Raman Spectra of Polyatomic Molecules* (Van Nostrand, Princeton, NJ, 1945).

    R.F. Willis, ed., *Vibrational Spectroscopy of Adsorbates*, Springer Series in Chemical Physics, Volume 15 (Springer, Berlin, 1980).

    N.B. Colthup, L.H. Daly, and S.E. Wiberley, *Introduction to Infrared and Raman Spectroscopy* (Academic, New York, 1990).

11. X.D. Zhu, PhD Thesis, University of California - Berkeley, 1989 (unpublished).

12. R.G. Snyder, J. Chem. Phys., **42**, 1744 (1963).

13. H.W. Schotter and H,W. Klockner, *Raman Spectroscopy of Gases and Liquids*, A. Weber, ed., (Springer-Verlag, Berlin, 1979).

14. P. Guyot-Sionnest and Y.R. Shen, Phys. Rev. B, **38**, 7985 (1988).

15. P.S. Pershan, Phys. Rev., **130**, 919 (1963).

N. Bloembergen, R.K. Chang, S.S. Jha, and C.H. Lee, Phys. Rev., **174**, 813 (1968).

16. Continuum PY61C-20 laser system.

17. A. Laubereau, L. Greiter, and W. Kaiser, Appl. Phys. Lett., **25**, 87 (1974).

A. Seilmeier and W. Kaiser, Appl. Phys., **23**, 113 (1980).

W. Kranotzky, K. Ding, A. Seilmeier, and W. Kaiser, Opt. Comm., **34**, 483 (1980).

18. J.Y. Zhang, J.Y. Huang, Y.R. Shen, and C. Chen, J. Opt. Soc. Am., **10**, 1758 (1993).

H.-J. Krause and W. Daum, Appl. Phys. B, **56**, 8 (1993).

19. *Detection of Optical and Infrared Radiation*, R.H. Kingston, ed., (Springer-Verlag, New York, 1978).

Figures

Fig. 1. A typical geometry for the SHG and infrared-visible SFG experiments. The infrared beam arrived s- or p- polarized using a double Fresnel rhomb, half-wave retardation device or preferentially by successive orthogonally positioned mirrors. The beam was then focused to the sample using a CaF_2 lens. The visible beam power and polarization was controlled using a half-wave plate, polarizer, half-wave plate combination. Both beams were spatially and temporally overlapped on the sample. The SHG and SFG signals were extracted using appropriate spatial filtering, spectral filtering and PMT detection. A UHV chamber was used for the diamond experiments (not shown).

Fig. 2. Upper Figure: The simple two-stage angle-tuned OPG/OPA using $LiNbO_3$.
Lower Figure: The two-stage near-infrared to far-infrared source utilizing BBO and $AgGaS_2$ (or $LiNbO_3$) crystals pumped by green (532 nm) light. An in-line grating element narrowed the linewidth of the DFG output to ~4 cm^{-1}. Inset: alternative double-pass grating geometry. Refer to Appendix A for a detailed description of the operation.

Fig. 3. The idler output energy / pulse (μJ) versus frequency (cm^{-1}) for the $AgGaS_2$ DFG arm (solid line). The number of photons produced scales with $\frac{1}{f}$ of the output energy / pulse (dashed line - referenced to the output at the maximum frequency).

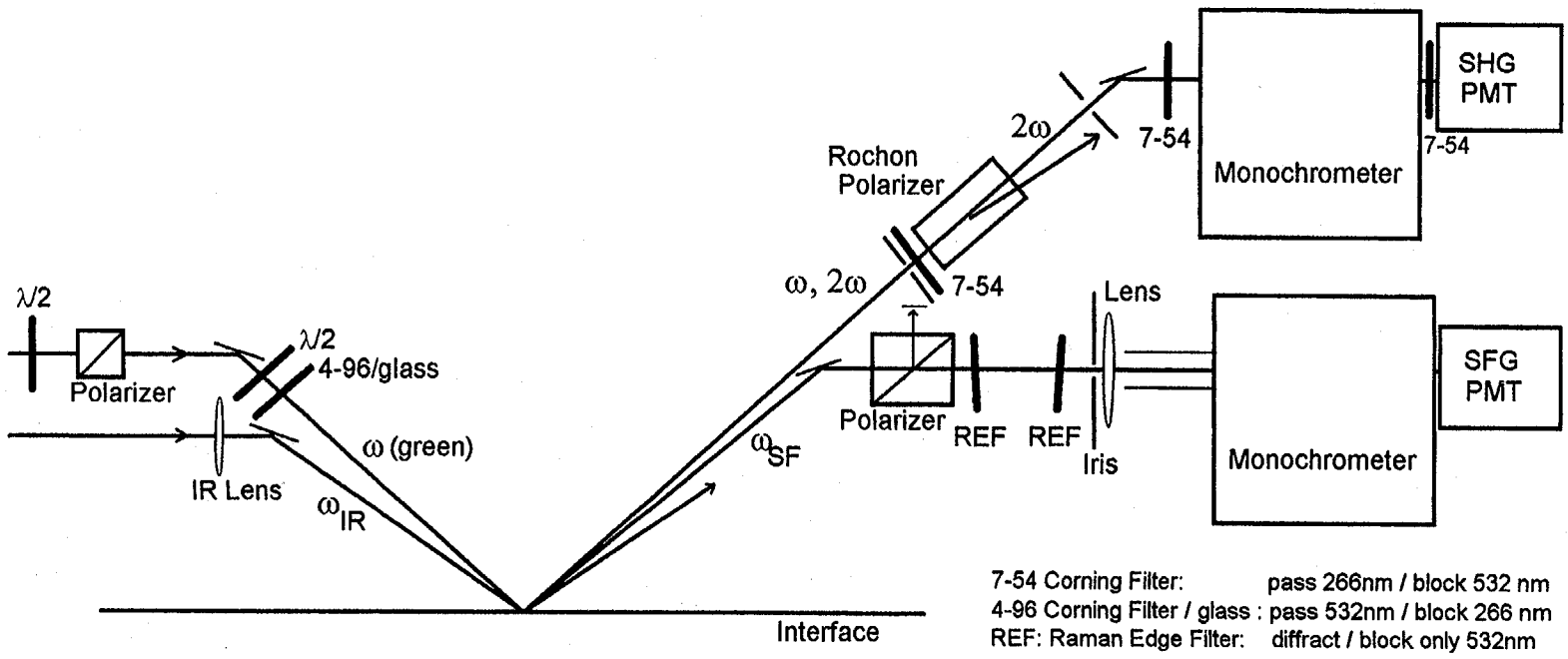
λ/2
Polarizer
λ/2
4-96/glass
ω (green)
IR Lens
ω IR
Interface
ω, 2ω
Rochon
Polarizer
2ω
7-54
Monochrometer
SHG
PMT
7-54
7-54
Lens
Polarizer
REF
REF
Iris
Monochrometer
SFG
PMT
ω SF
7-54 Corning Filter: pass 266nm / block 532 nm
4-96 Corning Filter / glass : pass 532nm / block 266 nm
REF: Raman Edge Filter: diffract / block only 532nm

Fig. 1

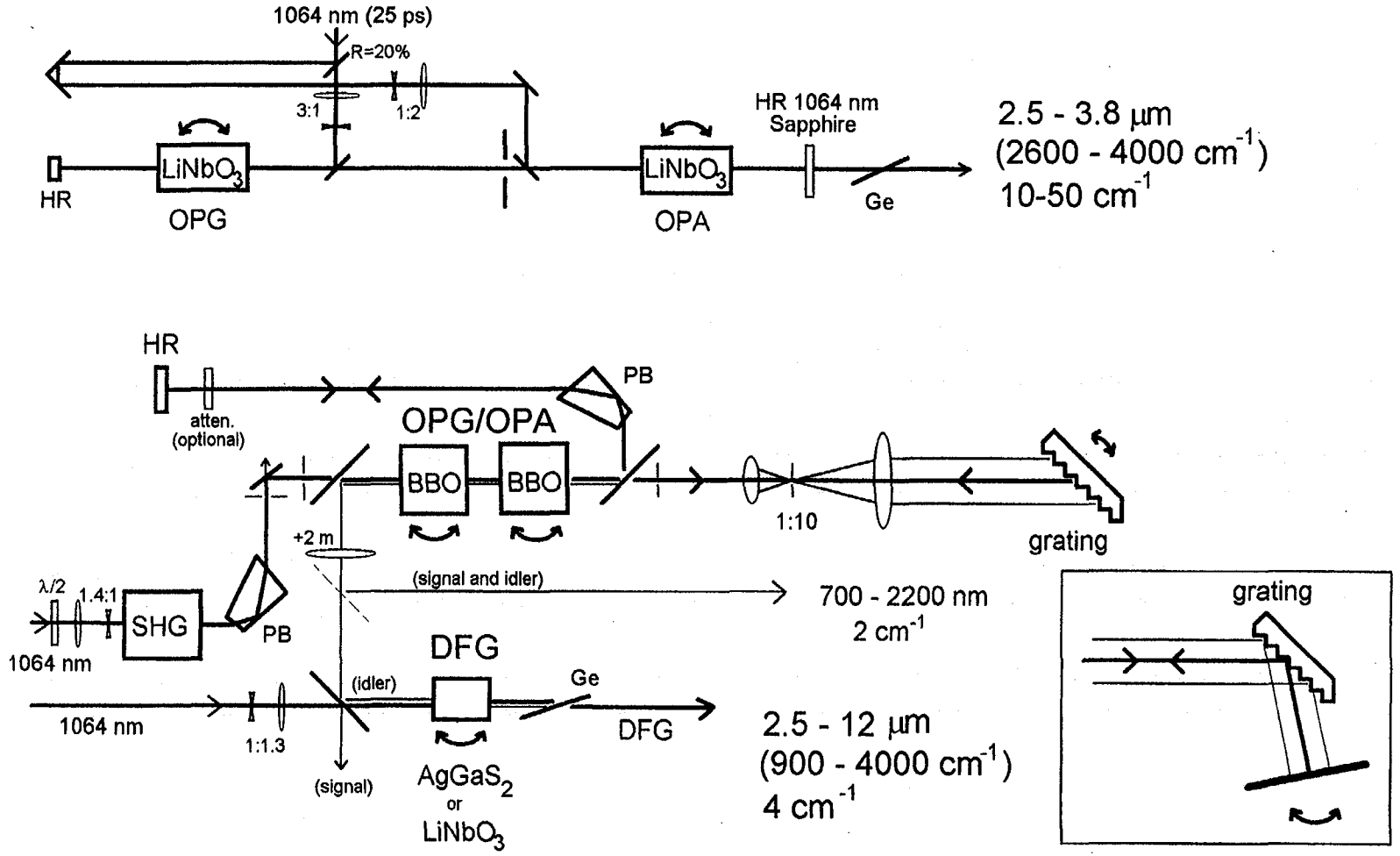
1064 nm (25 ps)
R=20%
3:1
1:2
HR
LiNbO3
OPG
LiNbO3
OPA
HR 1064 nm
Sapphire
Ge
2.5 - 3.8 μm
(2600 - 4000 cm-1)
10-50 cm-1
HR
atten.
(optional)
PB
OPG/OPA
BBO
BBO
1:10
grating
+2 m
(signal and idler)
700 - 2200 nm
2 cm-1
λ/2
1.4:1
SHG
PB
1064 nm
DFG
(idler)
Ge
1064 nm
1:1.3
DFG
2.5 - 12 μm
(900 - 4000 cm-1)
4 cm-1
(signal)
AgGaS2
or
LiNbO3
grating

Fig. 2

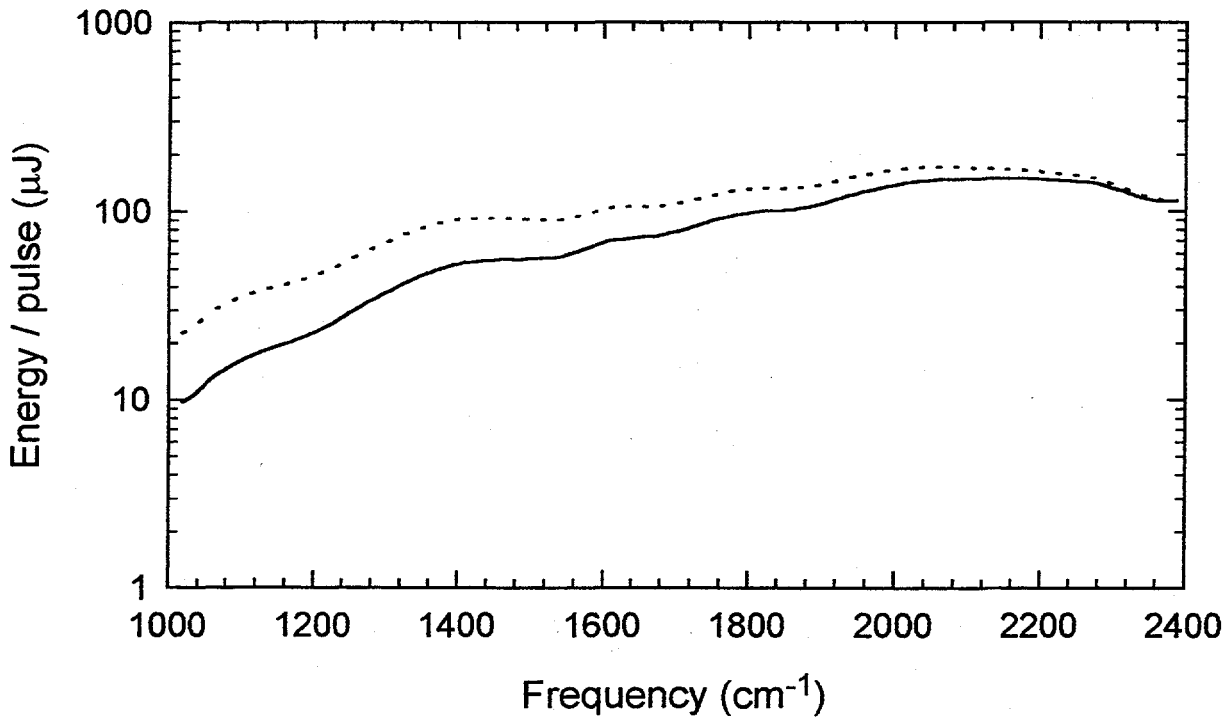
1000
100
10
1
Energy / pulse (μJ)
1000
1200
1400
1600
1800
2000
2200
2400
Frequency (cm-1)

Fig. 3

III. Interaction of Hydrogen with the Diamond C(111) Surface

A. Introduction

Diamond thin film growth by chemical vapor deposition (CVD), using thermal or plasma activation of gas phase species has proven to be successful and attracted a great deal of attention.[1] Although the conditions leading to good diamond growth are generally known, the detailed mechanisms are not yet clear. To improve the quality of CVD diamond films, especially for electronics applications, a good understanding of the diamond growth process is needed. For this, one must know what and how different reactive species appear on the diamond surface at various stages of the growth process and how they depend on the surface orientation. One also needs to learn how these species adsorb, desorb, and react. Most works reported in the literature have focused on gas composition and gas phase reactions in the CVD process. The results obtained could only provide indirect information about species and their reactions on the surface. Clearly, for a better study of the process, an in-situ monitoring of the surface with surface vibrational spectroscopy is most desirable. Indeed, electron energy loss spectroscopy (EELS) and more recently, sum-frequency generation (SFG) and Fourier-transform infrared (FTIR) spectroscopies have been employed for this purpose.

Atomic hydrogen adsorption on diamond seems to be a very important intermediate step in the diamond growth process. In the hot filament method of growth, for example, hydrocarbon gas is usually heavily diluted with hydrogen (such as <1% CH_4 in H_2) before passing through a hot filament and impinging on a high temperature substrate (~850°C).[2] This large fractional amount of hydrogen is found to be necessary in producing high quality diamond films. It is believed that atomic hydrogen facilitates

diamond growth by promoting the sp^3 hybridization of carbon, opening reactive sites, and removing graphitic materials. Thus, a study of hydrogen adsorption on diamond surfaces is paramount to the understanding of CVD diamond growth.

Several spectroscopic methods have been used to study diamond surfaces and hydrogen adsorption on diamond. Waclawski *et al.*[3] first used High Resolution Electron Energy Loss Spectroscopy (HREELS) to obtain the vibrational spectrum of an as-polished C(111) surface and concluded that the surface was terminated by CH_3. Lee *et al.*[4] studied hydrogen adsorption on C(111). From their HREELS spectra, they identified the presence of surface phonons on the bare reconstructed C(111) surface, and suggested a plethora of different hydrogen termination for hydrogen adsorption on C(111). Aizawa *et al.*[5] used HREELS to study the C(111) surface of diamond homoepitaxially grown by chemical vapor deposition (CVD) under microwave plasma-assisted deposition conditions. They interpreted the spectrum as due to the presence of CH_3 termination on the surface. In other cases, Hamza *et al.*[6] used time-of-flight mass spectrometry to study desorption of hydrogen from C(111) and C(100) and the resulting surface reconstruction. Mitsuda *et al.*[7] used low energy electron diffraction (LEED), Auger, and X-ray photoemission (XPS) to study the C(111) surface reconstruction with H adsorption. They showed that only a small hydrogen coverage (~5% ML) is already sufficient to convert the surface to the (1x1) bulk-terminated geometry. Sum frequency generation (SFG) spectroscopy has obtained vibrational spectra of hydrogen adsorption on C(111).[8] It was found that only a single peak in the CH stretch region was observed, indicating the presence of only a single monohydride species on the surface. This has been confirmed by the work of Hamza *et al.* using electron stimulated desorption ion angular distribution (ESDIAD) and by Butler *et al.*[9] using surface Fourier Transform Infrared Spectroscopy (FTIR). Second harmonic generation (SHG), also a second order nonlinear optical process has been employed to investigate the surface as an in-situ real-time optical surface

sensitive probe. This was especially valuable during real-time in-situ processes such as adsorption.

All these experiments seem to be consistent with the following picture: hydrogen appears to terminate the as-polished or atomic-hydrogen-dosed C(111) surface; the (1x1) bulk-termination stabilizes the surface at sufficiently low temperatures (<1150 K); upon hydrogen desorption at high temperatures (>1450 K), the surface undergoes a reconstruction to the (2x1) geometry. The form of the hydrogen termination however still remains a controversy. Some studies suggest the domination of monohydride surface species while others advocate the presence of other hydride species such as aliphatic $CH_{X=2,3}$ or olefinic CH_2. Sample preparation, dosing conditions, and limitations of individual spectroscopic techniques may be the cause of these discrepencies. Small sizes of diamond often limit the sensitivity of electron spectroscopies, thermal desorption spectrometry, and FTIR studies. HREELS as a vibrational spectroscopy has the advantage of a wide energy range and good sensitivity but suffers from relatively poor resolution. Conversely, FTIR has good resolution but poor surface sensitivity.

Infrared-visible sum-frequency generation (SFG) with unique capabilities for surface vibrational spectroscopy and second harmonic generation (SHG) have recently been demonstrated to be a versatile surface probes.[10] Being second-order nonlinear optical process, these are highly surface sensitive at the interfaces of centrosymmetric bulk media. For infrared-visible SFG, it has a transform-limited spectral resolution and a spectral range limited only by the infrared source. The polarization dependence of the spectrum permits deduction of molecular orientations of surface species. It is clear that the technique possesses enough desired advantages for studying hydrides on the diamond surface and resolving the above-mentioned controversy. This in-situ technique can also be adapted to realistic growth conditions in which the electron spectroscopies generally fail.

Here, the recent studies of the interaction of atomic hydrogen on the diamond C(111) surface using SFG and SHG spectroscopy are presented. Section B discusses how the surface nonlinear susceptibility contributes to the observed signal and how information about H/C(111) can be derived. Section C describes the experimental apparatus and sample preparation. Section D presents the experimental results for the hydrogen terminated surface, the adsorption / abstraction / desorption of hydrogen, and the reconstructed surface, and their respective interpretations are given in Section E.

B. Second Harmonic Generation and Sum Frequency Generation

Infrared-visible SFG for surface vibrational spectroscopy and second harmonic generation (SHG) spectroscopy have been described in earlier publications.[10,11,12] These second-order processes, in the electric-dipole approximation, are forbidden in the bulk of centrosymmetric media but are allowed at their interfaces where the inversion symmetry is necessarily broken.

The case for SFG is described here with an adaptation for SHG explained later. In the case of a monolayer of adsorbates on a centrosymmetric substrate, the macroscopic nonlinear surface susceptibility $\vec{\chi}_S^{(2)}$ of this layer can be related to the nonlinear molecular polarizability $\vec{\alpha}^{(2)}$ by a coordinate transformation from the molecular axes denoted by $\hat{l}, \hat{m}, \hat{n}$ to the lab axes denoted by $\hat{i}, \hat{j}, \hat{k}$:

$$\begin{aligned} \chi_{S,ijk} &= N_S \sum_{l,m,n} \left\langle (\hat{i}\cdot\hat{l})(\hat{j}\cdot\hat{m})(\hat{k}\cdot\hat{n}) \right\rangle \alpha^{(2)}_{lmn} \\ &= N_S \left\langle \alpha^{(2)} \right\rangle_{ijk} \end{aligned} \tag{3.1}$$

if interactions between molecules are neglected, where N_S is the surface molecular density, and the angular brackets $\langle\ \rangle$ denote the orientational average. The non-zero independent elements of $\vec{\chi}_S^{(2)}$ (the S is omitted from now on for brevity) can be deduced by measuring the signals for different polarizations of the incident and output beams.

Consider for example, a (111) surface with C_{3V} (3m) symmetry lying in the XY plane and having the mirror plane in XZ where X,Y, and Z are the laboratory coordinates. It should have five independent surface nonlinear susceptability elements: the anisotropic terms $\chi^{(2)}_{YYX} = \chi^{(2)}_{YXY} = \chi^{(2)}_{XYY} = -\chi^{(2)}_{XXX}$, and the isotropic terms $\chi^{(2)}_{ZYY} = \chi^{(2)}_{ZXX}$, $\chi^{(2)}_{YYZ} = \chi^{(2)}_{XXZ}$, $\chi^{(2)}_{YZY} = \chi^{(2)}_{XZX}$, and $\chi^{(2)}_{ZZZ}$. The sub-indices here refer to the directions of the field components of the sum-frequency output, visible input, and infrared input, respectively. If the plane of incidence is chosen to coincide with the YZ plane and the output/input polarization combination as pss (sum-frequency output, visible input, and infrared input, p-, s-, s- polarized, respectively), one can deduce from the SFG measurement the element $\chi^{(2)}_{ZXX}$. With the ssp, sps and sss combinations, $\chi^{(2)}_{XXZ}$, $\chi^{(2)}_{XZX}$, and $\chi^{(2)}_{XXX}$, respectively are readily obtained. Finally, with the ppp combination, one can find $\chi^{(2)}_{ZZZ}$ from the SFG measuremnt, knowing $\chi^{(2)}_{XXZ}$, $\chi^{(2)}_{XZX}$, and $\chi^{(2)}_{XXX}$.

For the case of SHG, the macroscopic surface susceptabilities $\chi^{(2)}_{ijk}$ listed above can be applied with the j and k indices representing the degenerate inputs of the visible light, in this case, 532 nm with the i index representing the SHG output at 266 nm. In this case, the polarization combinations generally used are s-in p-out and p-in p-out, which is analogous to ssp and ppp polarization combinations used for SFG.

The effective surface susceptibility for the SFG process near vibrational resonances can usually be written as the sum of a resonant term $\vec{\chi}_R^{(2)}$ and a nonresonant term $\vec{\chi}_{NR}^{(2)}$: [13]

$$\vec{\chi}_S^{(2)} = \vec{\chi}_{NR}^{(2)} + \vec{\chi}_R^{(2)}$$

$$\vec{\chi}_R^{(2)} = N_S \sum_Q \left\langle \vec{\alpha}^{(2)} \right\rangle_Q = N_S \sum_Q \left\langle \frac{\vec{A}_Q}{\omega_{IR} - \omega_Q + i\gamma_Q} \right\rangle \qquad (3.2)$$

$$\text{where } \vec{A}_Q = \sum_n \langle g|\vec{\mu}|n\rangle\langle n|\vec{M}|g\rangle / \hbar$$

Here, Q refers to the resonance mode with its frequency and damping constant denoted by ω_Q, and γ_Q, and its contribution to the SFG is proportional to A_Q which is a product of the infrared dipole matrix element $<g|\vec{\mu}_k|n>$ term and the Raman matrix element $<n|\vec{M}|g>$. With the SF output proportional to $\left|\vec{\chi}_S^{(2)}\right|^2$, the resonant enhancement of $\vec{\chi}_S^{(2)}$ as ω_{IR} scans over ω_Q yields the desired surface vibrational spectrum.

To see how the determination of $\chi_{R,ijk}^{(2)}$ can yield information about the orientation of a molecule or a bond at a surface consider the stretch mode of carbon monohydride (CH) distributed isotropically on a surface. The relevant elements of $\vec{\chi}_R^{(2)}$ are related to the molecular polarizability $\alpha_{\zeta\zeta\zeta}^{(2)}$ of the CH bond by:

$$\chi_{R,YYZ}^{(2)} = N_S \alpha_{\zeta\zeta\zeta}^{(2)} \left[\frac{1}{2}(1-r)\left\langle \sin^2\theta \cos\theta \right\rangle + r\langle \cos\theta \rangle\right]$$

$$\chi_{R,YZY}^{(2)} = \chi_{R,ZYY}^{(2)} = \frac{N_S}{2} \alpha_{\zeta\zeta\zeta}^{(2)} (1-r)\left\langle \sin^2\theta \cos\theta \right\rangle \qquad (3.3)$$

$$\chi_{R,YYX}^{(2)} = \chi_{R,YXY}^{(2)} = \chi_{R,XYY}^{(2)} = 0$$

where θ is the orientation angle of the CH relative to the surface normal, $r = \alpha^{(2)}_{\eta\eta\zeta} / \alpha^{(2)}_{\zeta\zeta\zeta}$ (≈ 0.14) is the ratio of transverse and longitudinal Raman polarizability associated with a CH bond[14], η and ζ are the axes perpendicular and parallel to the bond axis, respectively, and $\langle\ \rangle$ denotes the orientational average of the CH bonds on the surface. From Eqn. (3.3), it is now possible to determine the polar bond angle (assuming an orientational distribution) from $\chi^{(2)}_{R,YYZ}$ and $\chi^{(2)}_{R,YZY}$.

For the bare, reconstructed surface C(111)-(2x1), the π-bonded chains are aligned along the (2x1) domains. With such domains oriented in three equivalent directions, the surface is sometimes referred as the C(111)-(2x1)/(2x2) surface. For this reconstructed surface, a particular bond with azimuthal angle ϕ has a matching bond with an opposite azimuthal angle $-\phi$, thereby effectively yielding azimuthal isotropy with $\chi^{(2)}_{R,YYX} = 0$.

In a similar manner, the terms for the CH bending mode can be derived using Eqn. (3.1). Further, other hydride configurations, such as for aliphatic CH_2 and CH_3, and olefinic $=CH_2$ can also be derived.

C. Experimental Apparatus and Sample Preparation

The experimental setup has been described elsewhere.[11,12] In the present experiment, the laser system produces picosecond visible (0.532 μm, 17 psec) and tunable infrared pulses for the SFG experiment. Tunable infrared pulses (~17 psec) at ~3.5 μm with a 12 cm^{-1} linewidth were generated from a $LiNbO_3$ Optical Parametric Generator/Amplifier (OPG/OPA) producing 400-500 μJ per pulse at 15 or 20 pulses per second. A second, more sophisticated BBO OPG/OPA seeding a $AgGaS_2$ Difference

Frequency Generation (DFG) system generated broadly tunable (~8 psec) infrared pulses (3.5-10 μm) with 100 μJ at ~5 μm and ~50 μJ at ~7 μm, with a 4 cm^{-1} linewidth.[15] The visible and infrared beams were overlapped on the diamond surface with beam diameters of ~600 μm and ~300 μm, respectively. A 7° angular separation between the input beams (46° for the visible and 53° for the infrared beam) permitted spatial separation of the second harmonic and sum frequency output signals as determined by the phase matching conditions. Both signals were simultaneously measured with separate detection arms using sensitive gated photon counting techniques. Polarization combinations normally used for SFG were: ssp (s-SFG, s-Visible, p-IR), pss, ppp, and sps. Spatial filtering of the SFG was imperative for suppressing the background fluorescence (and possibly SFG) caused by the the molybdenum heater below the transparent diamond substrate.

The tunable infrared sources were calibrated to within 2 cm^{-1} with polystyrene / mica references and a calibrated monochrometer. All SFG spectra were normalized against a non-resonant SFG signal from for example, a crystalline quartz to minimize effects due to IR energy changes, beam overlap variations, and detector responsivity during scans. The peak positions (ω_q), strengths (A_o), and widths (γ_q) of a resonance $\chi_R^{(2)}$ and the nonresonant background $\chi_{NR}^{(2)}$ were determined by a fit of the SFG spectrum to Eqn. (3.2).[13]

For SHG of the 532 nm beam yielding the 266 nm signal, three 7-54 Corning color filters (T(532 nm)~10^{-6}, T(266 nm)~70 %) and a monochrometer were employed to remove the 532 nm light.

A natural type-IIa diamond cut to within 3° of the (111) surface was mechanically polished with 0.25 μm diamond abrasive in olive oil to produce a hydrogen saturated surface.[16] Cleaning was accomplished using an acid bath (1 part HNO_3 : 3 parts H_2SO_4 @ 100°C for 10-20 hrs.), followed by a rinse in distilled water and then in methanol. The sample was mounted on an all molybdenum resistive heater within an

ultrahigh vacuum chamber with a base pressure of ~$5x10^{-10}$ torr. No tantalum metal was used as this had been found to cause a substantial contamination on diamond especially with hydrogen adsorption. During the bakeout, the sample was kept at 500°C to keep the sample clean and to outgas the heater. The sample temperature was measured using a 0.005"ϕ type-G thermocouple in intimate contact with the diamond but not with the heater. A 1800°C (5 mm x 10 mm x 0.001") tungsten filament,[17] 12-16 mm from the diamond surface, was used to dissociate molecular hydrogen for atomic hydrogen dosing. The sample during dosing was initially at room temperature but rose to ~200°C after an extended period of dosing (>30 min.) due to radiative heating. An optical pyrometer reading, compensated for emissivity and viewport biases, was used to determine the hot filament temperatures. The pressure of H_2 for dosing was typically $5x10^{-7}$ - $1x10^{-5}$ torr.

Mostly the SFG spectra (ssp) associated with $\chi^{(2)}_{YYZ}$ in the CH stretch region is measured because this arrangement yields the strongest SFG signal from a hydrogen-saturated C(111)-(1x1)-H surface.[8] For the H-terminated surface, a single CH stretch peak was observed. With the sample mildly annealed at ~600°C, the peak became slightly narrower (~6-10 cm^{-1} FWHM) and stronger by 10-50%. If the sample was dosed at ~800-850°C with ~$1x10^{-5}$ torr H_2 for 5-10 minutes and then stopped at a 750°C substrate temperature as the sample quickly cooled, the stronger and narrower peak signal was immediately attained. This latter procedure was extremely effective at reliably reproducing a well-prepared H-terminated C(111) surface characterized by the single, strong and narrow CH stretch peak. Once hydrogen terminated, the signal remained unchanged after 20 hours of storage in vacuum (<10^{-9} torr).

D. Experimental Results

D.1. Hydrogen Terminated Surface C(111)-(1x1)-H

A clean, well-ordered C(111)-(1x1)-H surface should exhibit a simple truncated bulk structure.[6,7,16] The monohydride surface layer is expected to yield a single CH stretch mode and a single CH bend mode. The inital SFG studies[8] gave a ssp SFG spectrum of a H-saturated C(111) surface and indeed showed a *single* CH stretch peak at ~2830 cm^{-1} (Fig. 4). Using the narrow-linewidth, better calibrated, and more broadly tunable infrared source, the ssp SFG spectrum shows the single stretch peak[18] at 2838 cm^{-1} and a *single* CH bending mode peak at 1331 cm^{-1} (Fig. 5 and 6). For the sps spectrum, the bending mode peak was strong but the stretch mode peak was essentially absent. No other spectral features were discernible in the range of 1100 cm^{-1} to 3300 cm^{-1}. These results are expected from the on-top adsorption of H on C(111). It is coincidental that this has nearly the same frequency as the zone-center phonon mode of the substrate (1332.5 cm^{-1}),[19] as determined by Raman spectroscopy. To be sure that the observed peak at 1331 cm^{-1} was indeed the CH bending mode, the surface was dosed with deuterium to replace hydrogen. Now, the 1331 cm^{-1} peak was completely suppressed as the CD bending mode should appear at ~900 cm^{-1} instead and the corresponding CH stretch peak at 2838 cm^{-1} was replaced by the CD stretch peak at 2115 cm^{-1}. The latter is presented in Fig. 9 for a C(111) surface saturated by deuterium. The observed CD stretch frequency (2115 cm^{-1}) is about 0.75 times the CH stretch frequency (2838 cm^{-1}). This can be compared with the approximate theoretical ratio of $1/\sqrt{2} = 0.71$, the ratio of 0.75 for $\underline{DC}Cl_3$ (2255 cm^{-1}) versus $\underline{HC}Cl_3$ (3019 cm^{-1}),[20] and the ratio of 0.71 for $\underline{DC}(CD_3)_3$ (2063 cm^{-1}) versus $\underline{HC}(CD_3)_3$ (2887 cm^{-1}).[21]

The beam polarization dependence[8] of the stretch peak gives information about the orientation of the CH bond. The polarization dependence of the 2830 cm^{-1} peak is depicted in Fig. 4. It is seen that while the ssp SFG spectrum exhibits the peak clearly, the sps and pss spectra are barely detectable. This immediately suggests that the CH bonds must be mainly along the surface normal since then only the p-polarized infrared input can excite the CH stretch vibration. An analysis of the spectra of Fig. 4 using Eqn. (3.3) yields a mean angular spread of the bond orientation of ~60° if the average bond direction is taken to be along the surface normal. This agrees with the conclusion derived from electron-stimulated ion desorption by Hamza *et al.*. The polarization dependence of the 2860 cm^{-1} peak is very similar to that of the 2830 cm^{-1} peak, indicating that the CH bonds responsible for this peak must also be along the surface normal.

The above results strongly support the picture of atomic H adsorbed on top sites of C(111)-(1x1). An estimate of the frequency for such a surface CH stretch mode from the known CH stretch frequency (2992 cm^{-1}) of CHD_3 in the gas phase. Assuming that the spring constants for the CH vibration of the two cases are the same and the diamond surface can be approximated by a rigid wall with an infinite mass, one finds $\nu_{CH} = 2875\ cm^{-1}$ for the surface CH stretch along the surface normal. This is close to the observations. The corresponding CH bond length is estimated to be 1.11 Å following Ref. 20. A much more sophisticated total-energy calculation predicting the CH vibrational frequency and the anharmonicity for H/C(111)-(1x1) has been carried out by Zhu and Louie.[22]

The observation that the p-polarized infrared light could excite the CH stretch more strongly than the s-polarized infrared light indicates that the CH bond is lying preferentially along the surface normal. The analysis yielded a 30° distribution about the surface normal. A similar analysis for the bending mode yielded nearly equal intensities

for s- and p-polarized infrared beams as the dipole moment is essentially now parallel to the surface.

D.2. Temperature Dependence of the CH Stretch Frequencies and Linewidths

The experimental apparatus only allowed heating of the sample above room temperature. But, high temperature SFG spectra of the hydrogen-dosed C(111) surface for both the CH stretching and bending modes were possible. Figure 6 depicts two spectra at 300 K and 700 K. Both modes exhibit, a temperature-dependent shift in the peak position and broadening of the peak width. For the CH bend and stretch modes, the peak positions change from 1330 to 1324 cm^{-1} and from 2837 to 2833 cm^{-1}, respectively, as the temperature increases from 300 to 700 K, while the corresponding peak halfwidths change from 5 to 7 cm^{-1} and from 7 to 9 cm^{-1}, respectively. The halfwidths were deconvoluted from the data in Fig. 6 with a 4.5 cm^{-1} (FWHM) gaussian infrared laser lineshape.

The increase of peak widths with temperature suggests that the peaks are homogenously broadened. This is supported by the CD spectrum in which the CD stretch peak exhibits a ~40 cm^{-1} halfwidth. Since the chemical environment (ie. the chemical structure and binding) should be the same for this isotopic H to D substitution, the change (increase) in the linewidth cannot be attributed to inhomogeneous broadening. It is most probable that the linewidth is dominated by dephasing broadening.

D.3. Adsorption, Desorption, and Abstraction of Hydrogen

Second harmonic generation (SHG) can be used to follow the response of the bare reconstructed diamond (111) surface to atomic hydrogen dosing.[7] With LEED[23] and optical second harmonic generation spectroscopy, it was found that adsorption of only a few percent of a full monolayer of H was sufficient to induce the (2x1) to (1x1) phase transformation. The CH stretch mode observed on a freshly formed (1x1) surface at a low H coverage without annealing, however, showed up as a peak at a higher frequency (2860 cm^{-1}) suggesting the freshly formed surface might not be fully relaxed. The full surface relaxation could be effected by either high-temperature annealing (without hydrogen desorption) or higher surface coverage of H.

For the clean C(111) surface, the LEED pattern revealed a (2x1) surface structure. When the surface was dosed to an H coverage of ~5% of a monolayer, both the LEED pattern and the optical second harmonic signal from the surface indicated that the surface had begun to convert from (2x1) to (1x1). The latter was indicated by a sudden spike in the SHG signal in both the p-in p-out (Fig. 2a) and s-in p-out (Fig. 2b) spectra. The SFG measurement also started to register a peak at 2860 cm^{-1} (peak positions, widths, and strengths reported here and in the following are values obtained from the fit to the observed spectra using Eqn. (3.2), spectral resolution was limited (at this time) to 10 cm^{-1} by the infrared source.

With continuous H dosage, the SHG signal after the (2x1) to (1x1) transition showed a gradual response. Figure 2 shows that the p-in p-out spectrum (Fig. 2a) appears to be more complicated than the s-in p-out spectrum (Fig. 2b). This can be explained by the fact that the former probes more susceptibility components where they can interference with each other whereas the latter probes only one component ($\chi^{(2)}_{YYZ}$) as the surface mirror plane symmetry was in the XZ plane.

For the SFG spectrum, the 2860 cm^{-1} peak first increased in strength, reached a maximum at ~42% monolayer H coverage, and decreased afterward to nearly zero at full monolayer H coverage. In the meantime, a new peak at ~2830 cm^{-1} showed up and grew monotonically with increase of H coverage. The SFG spectral variation described above is illustrated in Fig. 7. It should be noted that the vibrational spectra reported here were very different from that obtained by EELS. The strength of the 2860 cm^{-1} peak could be transferred to the 2830 cm^{-1} peak by annealing the sample at ~700°C. Annealing not only eliminated the former completely, but also made the latter narrower, presumably due to a relief of surface strain set in by the surface structural transformation. After the (1x1) surface was annealed, the 2860 cm^{-1} would not appear again with further desorption or readsorption of H or with any H coverage on the surface. The strength of the ~2830cm^{-1} peak could then be used to estimate the H surface coverage.

Figure 8, for example, shows how the H surface coverage decreases by thermal desorption as reflected in the reduction of the 2830 cm^{-1} peak in the SFG spectrum. A close examination of the spectra as a function of H surface coverage remaining reveals an approximately linear shift of the peak from full coverage and is given by $\Delta\nu_{CH} \approx -6.6(1-\Theta)\,cm^{-1}$ with $0<\Theta<1$ denoting the H coverage in terms of the fraction of a full monolayer. Following the SHG signal after each thermal cycle enables one to follow in a similar manner as for the adsorption case. Figure 3 shows the SHG signal also indicates the phase transition, in this case, the (1x1) to (2x1) reconstruction.

The observation of the 2860 cm^{-1} mode, which can be annealed away, suggests that there may exist a metastable (1x1) phase on C(111) resulting from H-adsorption-induced phase transition from (2x1) to (1x1). A π–bonded chain model has been proposed to be the most energetically favorable structure for the (2×1) surface. A conversion from the π–bonded chain structure to the bulk-truncated (1x1) surface would involve a rather complicated rearrangement of bonds. It is conceivable that a metastable

(1×1) phase might exist with slightly different bond angles and bond lengths from the truncated (1×1), although the exact configuration of that structure is not known. Apparently, both annealing and sufficiently high H coverage can cause this surface to relax to the more stable bulk-truncated (1x1) surface, whereas transition in the reverse direction seems impossible. To obtain the metastable (1x1) structure, the surface must be first reversed back to (2x1) by desorbing all H and then dosed with a small amount of H to induce the surface restructuring.

Atomic hydrogen adsorbs readily to the bare diamond surface. From CVD growth experiments, a large amount of hydrogen is often needed to produce high-quality films. Presumably the stable surface of diamond is mostly covered by hydrogen. The studies now investigate how hydrogen adsorption and abstraction affect the equilibirum H coverage on the C(111) surface. SFG spectroscopy was used to monitor in-situ the surface coverages of hydrogen and deuterium when a D-terminated surface was dosed by atomic H, assuming that the binding energies of H and D to the surface are the same.

Figure 9 illustrates the occurence of H (D) abstraction. As atomic hydrogen was dosed ($2x10^{-6}$ torr H_2 with the hot filament) onto the deuterium-covered surface, the CD peak at 2115 cm^{-1} decreased in strength while the CH peak at 2838 cm^{-1} increased. After ~10 minutes, the spectrum was totally dominated by the CH peak. It is apparent that atomic hydrogen was very effective at abstraction. Repeatedly, molecular hydrogen had no effect on either the bare reconstructed surface or the deuterium-terminated surface. Only atomic hydrogen appeared to react with the surface.

From the CH peak strength, the H coverage on the surface is deduced. Figure 10 shows the surface coverage of H on C(111) at room temperature as a function of dosing time at an H_2 pressure of $5x10^{-7}$ torr with atomic hydrogen dosed on a bare reconstructed surface and on a deuterium-covered surface. The adsorption on the bare surface appears to proceed faster than on the deuterium-covered surface as one would expect since in the

latter case, the surface deuterium must be abstracted from the surface by atomic hydrogen before hydrogen adsorption is to occur. From the difference in the two rates, one can deduce roughly the ratio of the rate of abstraction, K_{abs}, versus the rate of adsorption, K_{ads}. For dosing of the bare surface, the rate of change of the hydrogen coverage (Θ_H) is given by:

$$\begin{aligned} &\frac{d\Theta_H}{dt} = K_{ads}(1-\Theta_H) - K_{abs}\Theta_H \\ &\text{At } t=0: \quad \Theta_H = 0 \\ &\text{At } t \to \infty: \quad \frac{d\Theta_H}{dt} = 0 \qquad \Theta_H = \Theta_{eq} = \frac{K_{ads}}{K_{ads}+K_{abs}} \end{aligned} \tag{3.4}$$

For H dosing of the deuterium-covered dosed surface, the rate equations for hydrogen (Θ_H) and deuterium (Θ_D) coverages are:

$$\begin{aligned} &\frac{d\Theta_H}{dt} = K_{ads}(1-\Theta_H-\Theta_D) - K_{abs}\Theta_H \qquad \frac{d\Theta_D}{dt} = -K_{abs}\Theta_D \\ &\text{At } t=0: \quad \Theta_H(t=0)=0 \qquad \Theta_D(t=0)=\Theta_D^0 < 1\,\text{ML} \\ &\text{At } t\to\infty: \quad \frac{d\Theta_H}{dt} = \frac{d\Theta_D}{dt} = 0 \qquad \Theta_H = \Theta_H = \frac{K_{ads}}{K_{ads}+K_{abs}} \qquad \Theta_D = 0 \end{aligned} \tag{3.5}$$

Here, the rate of abstraction of deuterium is assumed to be the same as for hydrogen.

By fitting the data in Fig. 10 with the above equations, the ratio $K_{abs}/K_{ads} = 0.2$ was found. This gives an equilibrium coverage of $\Theta_{eq} = K_{ads}/(K_{ads}+K_{abs}) = 83\,\%$ at room temperature. By comparing the strengths of the SFG signals, the hydrogen saturation coverage on C(111) at room temperature was ~80 % of that obtained with the high temperature (~800°C) sample treatment. This suggests that the rate of adsorption to the rate of abstraction must be higher at higher temperatures.

D.4. Determination of the Kinetic Parameters for Thermal Desorption of Hydrogen

Thermal desorption of H from C(111) can provide information about hydrogen desorption kinetics. In ultrahigh vacuum, with readsorption negligible, desorption of hydrogen can be assumed to obey the equation:

$$\frac{d\Theta_H}{dt} = -k\,\Theta_H^n \tag{3.6}$$

where n is the order of the reaction, $k = \nu \exp(-E_d / k_B T)$, ν is a pre-exponential factor, E_d is the desorption activation energy (ν and E_d are assumed not depend on coverage or temperature), k_B is the boltzman factor and T is the temperature which can be a function of time t. If n>1, Eqn. (3.6) is integrated to yield:

$$\frac{1}{(n-1)}\left(\frac{1}{\Theta_f^{n-1}} - \frac{1}{\Theta_i^{n-1}}\right) = \int_{t_i}^{t_f} dt\, \nu \exp(-E_d/k_B T) \qquad (n>1). \tag{3.7}$$

SFG was used to monitor the H coverage (Θ_H) following thermal desorption. The measurements were made each time after the surface was rapidly heated to a high goal temperature where desorption was appreciable and cooled back to room temperature (where practically no desorption occurred). The goal temperature of each heating cycle was varied from 700°C to 1000°C. The temperature profile, T(t), of each heating cycle was automatically recorded (every 0.5 secs.). Typically, heating to 800°C from room temperature required at least ~45 sec. and cooling to 500°C required at least ~200 sec. For lower goal temperatures (~750°C), the sample was held at the goal temperature for a

longer interval in order to have an appreciable change in the H coverage by thermal desorption.

As seen earlier, the SFG spectrum of the CH stretch would exhibit a complex lineshape change with the H desorption[8] resulting from interference of the resonant $\vec{\chi}_R^{(2)}$ with the nonresonant background, $\vec{\chi}_{NR}^{(2)}$. However, by a fit of the spectrum to Eqn. (3.2), $\vec{\chi}_R^{(2)}$ which is proportional to Θ_H is deduced. In the desorption measurements, the heating cycles used are described in Fig. 11 (solid lines). Starting with a saturated H coverage (normalized to 1) at the beginning of the first, sixth, and eighth cycles, the coverages, Θ_H were measured and presented in Fig. 11 (open squares). The theoretical fit by Eqn. (3.6) is also shown (dashed lines) in the figure for comparison using the measured temperature profiles T(t) and n, ν, and E_d as fitting parameters. (Cycles 6 and 8 were specifically chosen to desorb at a low temperature while cycles 4, 5, 7, and 9 were used to include low coverage data. This enabled a more precisely determined fit to the parameters with ν and E_d not strongly interdependent in the fitting). For the C(111)-(1x1)-H surface, the fit yielded $n = 1.3 \pm 0.3$, $\nu = 10^{15 \pm 2}\ s^{-1}$, and $E_d = 4.0 \pm 0.4$ eV. The uncertainty in the parameters reflects the experimental uncertainty in determining the coverage and the temperature.

One can use the desorption energy E_d to estimate the CH bond strength. Assuming E_d is equal to the heat of adsorption, the CH chemical bond energy can be obtained[24] using $2E_{C-H} = (E_d + E_{H-H})$, since a hydrogen molecule must dissociate with dissociation energy E_{H-H} to form two CH bonds with the surface. With $E_{H-H} = 4.42$ eV and $E_d = 4.0$ eV, $E_{C-H} = 4.2$ eV is obtained, which is about 10 % smaller than a typical aliphatic CH bond (~4.5 eV). This is commensurate with the observed lower frequency of the CH stretch mode on C(111) as compared to that of a molecule (such as $CH(CH_3)_3$), indicating a weaker CH bond for H on C(111).

D.5. The Reconstructed C(111)-(2x1) Surface

If the C(111)-(1x1)-H surface is heated to >1200°C, the surface reconstructs to the C(111)-(2x1)/(2x2) surface as indicated by LEED.[6,7,16] Under the same conditions, there was complete suppression of the 1331 cm^{-1} and 2838 cm^{-1} CH peaks indicating the disappearance of hydrogen by thermal desorption. In the low-frequency range (1300-1550 cm^{-1}), however, new peaks appeared (Fig. 12). They must represent the surface phonons of the C(111) surface. It must be emphasized that very little hydrogen (~0.05 ML) is needed to hold the (1x1) phase and essentially complete hydrogen desorption must occur to cause the above described phase transition and the resulting spectra. If a small amount of atomic hydrogen is dosed (~0.05 ML) onto the (2x1) reconstructed surface, the surface phonon features completely disappear leaving a featureless spectrum; the CH bending mode is below the detection limit.

SFG is forbidden in the bulk of diamond because of existence of inversion symmetry. Near the H-terminated C(111)-(1x1) surface, although the C-C bonds might experience a broken symmetry, their contribution to SFG was not observed; only the CH bending (1331 cm^{-1}) and stretching (2838 cm^{-1}) modes appeared in the spectrum for H coverages of 0.05-1 ML. However, if hydrogen is fully desorbed, the reconstruction of the diamond surface involves a radical rearrangement of the surface carbon atoms. The current accepted model for the C(111) reconstruction is the Pandey (2x1) π-bonded chain model.[25] This results in a surface structure (Fig. 13) composed of a topmost layer of carbon chains with mostly sp^2 character and a next layer of carbon chains with mostly sp^3 character. This structure is highly asymmetric, allowing its vibrational modes observable by the infrared SFG technique.

Figure 12 shows two major bands of the SFG spectrum of the C(111)-(2x1) reconstructed surface between 1300 and 1500 cm^{-1}: a low frequency one around 1350 cm^{-1} observed with the IR input p-polarized and a second one 1475 cm^{-1} observed with both p- and s-polarized IR input. In principle the bond orientations can be deduced from the ratios of the peaks in the ssp and sps SFG spectra using Eqn. (3.3), and assuming that surface vibrations are localized to bonds. However, for C-C bonds, the transverse polarizabilities are not known making the deduction of the bond orientations difficult.

With some simplifying assumptions, some qualitative information is obtained about the bond orientations. From Eqn. (3.3), a ratio $|\chi_{YYZ}/\chi_{YZY}| \approx 1$ would indicate $\Theta \sim 90°$ for $r = \alpha^{(2)}_{\eta\eta\zeta}/\alpha^{(2)}_{\zeta\zeta\zeta} < 0.1$ This is the case for the observed ~1475 cm^{-1} band as seen from Fig. 12, suggesting that the C-C bonds responsible for the band must lie close to the surface plane. For the ~1350 cm^{-1} band, from Fig. 12, $|\chi_{YYZ}/\chi_{YZY}| \approx 3$. If $0 < r < 0.1$ (knowing $r = 0.14$ for CH bonds), Eqn. (3.3) yields $0° < \Theta < 35°$. This indicates that the corresponding C-C bonds must be leaning fairly close along the surface normal. The discussion how the picture fits with the surface structure in Fig. 13 is presented in the next section.

As seen in Fig. 12, the ~1350 cm^{-1} band is composed of two peaks at 30 cm^{-1} apart. The ratios of $|\chi_{YYZ}/\chi_{YZY}|$ for the two peaks are similar. These observations suggest the presence of two types of C-C bonds having nearly the same polar orientation (presumably not far away from the surface normal). For the ~1475 cm^{-1} band, one could regard it as a broad feature with a full width of ~60 cm^{-1} or imagine also two overlapping peaks with half the full width. In the latter case, the corresponding two types of C-C bonds would both lie nearly flat on the surface.

E. Discussion

E.1. Hydrogen Adsorption, Desorption, and Abstraction on the C(111) Surface

Waclawski *et al.*[3] first studied hydrogen adsorption on C(111) using HREELS. They concluded after comparing with the deuterated ethane spectra that -CH_3 must have terminated the surface. Their explanation for the presence of CH_3 species rather than the expected CH monohydride included: the possibility of surface defects not detected in the (1x1) LEED pattern; the corrosive action of hydrogen on diamond to create CH_2 and CH_3, similar to hydrogen on silicon[26]; and the break-up of the π-bonded chains during the adsorption process, leaving only singly-backbonded sp^3 hybridized carbons with the three remaining bonds occupied by hydrogen.

Recently, Lee *et al.*[4] similarly used HREELS, except with better resolution, to study hydrogen-terminated and bare (2x1)-reconstructed (111) and (100) surfaces. For surfaces with H adsorption, not only did they assign peaks to CH_3, they also believed in seeing evidence for other aliphatic (sp^3) and olefinic (sp^2) hydrocarbon species. They attributed the plethora of surface coordinations to the crude surface preparation with inherent multiple H adsorption sites and the propensity for carbon-carbon bond breaking in preference to hydrogen termination as in the case of silicon.[26]

In contrast, the SFG measurements of the as-polished and the atomic hydrogen exposed diamond C(111) surface with much better spectral resolution clearly show a *single* CH stretch at 2838 cm^{-1} and a *single* CH bend at 1331 cm^{-1} with linewidths narrower than 10 cm^{-1} and no other spectral features between 1100-3300 cm^{-1}. From the peak frequencies and the mode's polarization dependence, it is concluded that this peak must originate from a monohydride CH stretch with H sitting on top of C and not from other aliphatic $CH_{2,3}$ or olefinic CH_2 species.

Our conclusion that H terminates the C(111)-(1x1) surface in the CH monohydride form is consistent with the results of helium scattering and diffraction[27] and proton desorption (ESDIAD).[6] It has been suggested[4] that the discrepencies among works from different laboratories could be due to differences in the diamond samples and sample treatments. Our experience and others[28] with different diamond samples and various sample preparation techniques, show that this is indeed the case. The SFG technique is very surface sensitive, making it ideally suited to distinguish different types of hydrides on the surface and the degree of ordering as evidenced by the signal strength, and linewidth, and in principle, also the polarization dependence. For the C(111) diamond, consistently high-quality hydrogen-terminated surfaces necessitated the use of an acid bath for extended periods of time in order to remove graphitic carbon after polishing. Residual strain in the diamond sample appearing on the surface after repeated high-temperature heating processes could also cause difficulties, with spectral peaks excessively broadened by inhomogeneous broadening.

In hydrogenating the diamond surface for spectroscopic studies, it has been common to dose atomic hydrogen upon a bare substrate at or near room temperature. However, after repeated hydrogen dosing and desorption, the H-terminated surface often became less well-ordered, as evidenced by weaker and broader CH peaks and the appearance of features indicative of the presence of other hydrocarbon species. If the substrate was dosed by atomic hydrogen at 800-850°C as well as during cooling to ~750° C, the resulting H-terminated C(111) surface always appeared well-ordered. SFG spectra with strong and narrow CH stretch and bend peaks were observed even if the surface originally had been contaminated, for example, by activated methane, methyl iodide, or di-tert-butyl peroxide. Presumably, the aggressive replacement of unwanted hydrocarbon or carbon species by preferential hydrogen adsorption on the well annealed surface is the reason behind the successful surface treatment.

For the well-ordered H-terminated surface, the CH stretch and bend modes exhibited the minimum linewidths, 5 and 7 cm^{-1}, respectively, at room temperature. They are likely dominated by homogenous broadening resulting from the dephasing (T_2) mechanism. The lifetimes (T_1) of the CH stretch mode has been measured[18] (Ch. IV) to be ~19 psec, which corresonds to a broadening of only 0.25 cm^{-1}. Inhomogeneous broadening is presumably not of dominant importance because of the observation of temperature broadening of the peaks (from 5 to 7 cm^{-1} and 7 to 9 cm^{-1}, respectively, for the stretch and bend modes as the sample temperature changed from 300 to 700 K). Further evidence against inhomogeneous broadening comes from the observation that the CD stretch mode is ~8 times broader than that of CH while their physical and chemical environments giving rise to the inhomogeneous broadening are expected to be the same.

The observed monohydride CH stretch frequency (2838 cm^{-1}) on the C(111)-(1x1)-H surface is lower than that of a typical CH stretch mode of molecules in gas phase[29,37] (ν_{CH} ~2992 cm^{-1} for $\underline{HC}D_3$, ~2893 cm^{-1} for $\underline{HC}(CH_3)_3$, and 2887 cm^{-1} for $\underline{HC}(CD_3)_3$)[21]. This is believed to be mainly due to a change in the binding force although some difference can be attributed to the variation in reduced mass. Indeed, the bond between a hydrogen atom and a diamond surface carbon can have a very different charge distribution compared to a typical saturated CH bond[18]. The thermal desorption data yield a binding energy of 4.2 eV for H on C(111), which is about 10 % less than a typical saturated hydrocarbon bond in a molecule. This is consistent with the lower mode frequency for H on C(111).

When dosing with atomic hydrogen onto the bare C(111) surface, saturation of H coverage was seen after ~10 min. for the hot filament arrangement with $5x10^{-6}$ torr of H_2 in the chamber. Dosing of hydrogen onto the deuterium-terminated surface explicitly showed fast abstraction of D by H towards full coverage of H (Fig. 10). Similarly, an experiment starting with a fully H-terminated surface showed full conversion to the

D-terminated surface upon dosing of D with a similar rate (not presented here as these spectra are similar). Recently, Thoms *et al.*[30] calculated the rates at room temperature using their high resolution EELS data for adsorption of deuterium onto a bare diamond surface and a hydrogen-terminated surface. Their result gives a ratio of the two rates to be $K_{abs}/K_{ads} = 0.05$, which would yield a saturated D coverage of $\Theta_D = 0.95$. Although in the SFG experiment, the roles of H and D were interchanged, the rates are expected to be comparable. It seems that the abstraction rate was higher or the adsorption rate lower in this case. This could be due to the different dosing conditions as the hot filament geometry, position, and temperature were not likely to be the same.

The result on thermal desorption of hydrogen from C(111)-(1x1) was analyzed with the usual theory for thermal desorption. It yields nearly first-order kinetics within the coverage range studied. This seems to contradict the fact that hydrogen desorbed from C(111) should appear in the molecular form and therefore the desorption kinetics should be second-order. However, similar non-second-order thermal desorption has been observed for H desorption from Si surfaces. Sinniah *et al.* have measured a first-order desorption behavior of H from Si(100) and suggested that it may be due to irreversible excitations of adsorbed H atoms into delocalized band states before desorption.[31] There has also been experimental evidence of pre-pairing of H on Si(100), leading to the possibly observed first-order desorption.[32] Departures from second-order desorption have also been seen on Si(111)-(7x7) for low coverages; it is suggested that two binding sites may explain the behavior.[33] It is likely that thermal desorption of H from diamond behaves similarly as H from silicon, recognizing the close analog of the two cases in many respects.

E.2. The Reconstructed Surface

Although the bare C(111)-(2x1) reconstructed surface may not be of importance to the problem of CVD diamond growth, which typically involves a large amount of hydrogen-promoted (1x1) surface, its understanding is still of fundamental interest. This is particularly so because of close similarities between the equivalent Si, Ge, and α-Sn surfaces.

In their high-resolution EELS spectra for the reconstructed C(111)-(2x1) surface, Lee *et al.*[4] observed spectral features at 92 meV (740 cm^{-1}) and 153 meV (1235 cm^{-1}) and attributed them to stretch and rock surface phonons. The assignment was reached by comparing[34,35] with scaled-up surface phonon frequencies of Si(111) using the same scaling factor relating the bulk phonon frequencies of Si(111) and C(111). The required electric-dipole character was known to come from the surface reconstruction. The SFG spectra have much higher resolution than high-resolution EELS, and two well-resolved bands were observed at somewhat higher frequencies in the 1300-1550 cm^{-1} range. Still, they are within the range of stretch surface phonon frequencies predicted by Lee *et al.*[4] from scaling. As described in Sec. D.5, the low-frequency band seems to be associated with C-C bonds more inclined towards the surface normal and the high-frequency band with C-C bonds more inclined towards the surface. Each band appears to have two split components (Fig. 12). One may find some understanding of the spectra by referring to the reconstructed surface structures depicted in Fig. 13.

The structures in Fig. 13 are derived from the Pandey π-bonded chain model, which has been widely accepted for the (2x1) reconstructed surfaces.[6,16,25] There exist some variations of the model proposed by different researchers. In particular, buckling of the surface bilayer or dimerization of intrachain bonds that could reduce the configurational energy has been predicted. Bechstedt and Reichardt, have concluded

from a self-consistent, semi-empirical tight-binding calculation that the Pandey π-bonded chain model with slight buckling but undimerized chains in the surface layer would have the lowest energy. On the other hand, recent work by Iarlori *et al.* have predicted from a self-consistent *ab initio* molecular dynamics calculation that there should be dimerized π-bonded chains with no buckling in the surface layer.

From the structures described in Fig. 13 and the required broken symmetry for SFG, a surface phonon mode is expected to be associated strongly with C-C bonds connecting the sublayers of the surface bilayer and another with C-C bonds connecting the first two surface bilayers. It is known that the π-bonded chains of the top surface bilayer have strong sp^2 character, while the bonds connecting the top bilayer and the second bilayer have sp^2/sp^3 mixed character. Deeper into the bulk, the bonds should have more and more sp^3 bulk-like character. Raman measurements[19,36] on the bulk diamond (sp^3), graphite (sp^2), and amorphous carbon (sp^2/sp^3), yielded bulk phonon frequencies 1332.5 cm^{-1}, 1580 cm^{-1} and 1360-1560 cm^{-1}, respectively. Studies of various hydrocarbon molecules[37] also showed that C-C bonds with sp^2 character have higher stretch frequencies than those with sp^3 character. Therefore the high-frequency band (~1475 cm^{-1}) is assigned to surface phonons associated with the C-C bonds connecting the sublayers of the surface bilayer and the low-frequency band (~1350 cm^{-1}) to phonons associated with the C-C bonds between the first and second surface bilayers. This result is consistent with the result deduced from the polarization dependence of the spectral peaks that the high-frequency and low-frequency bands should be associated with bonds inclined, respectively, more towards the surface and more towards the surface normal.

Although the general assignment of the high and low frequency bands are made, the apparent splitting within each band has to be addressed. Of the two variations of the Pandey model, the one proposed by Bechstedt and Reichardt is the only one that can explain the fine structure. In this model, there are two different types of bonds within the

top bilayer (high frequency band) and also between the two top bilayers (low frequency band) due to buckling. This leads to a splitting within each band. The general agreement between the experimental results and the theoretical model lends credit to the model.

F. Conclusion

The diamond C(111) surface dosed by atomic hydrogen was studied using infrared-visible sum frequency generation (SFG) spectroscopy. The as-polished/dosed H-terminated surface spectra indicate a *single* monohydride peak (1331 cm^{-1} and 2838 cm^{-1}) with an orientation preferentially along the surface normal. Atomic hydrogen is shown to be aggressive in hydrogen (deuterium) abstraction. Thermal desorption spectroscopy of hydrogen suggests near first-order desorption with desorption energy of 4.0 eV. On the reconstructed (2x1) surface, CC features associated with the reconstruction of bilayers are readily observed at 1300-1500 cm^{-1} showing two major bands confirming the Pandey π-bonded chain model.

References

1. R. C. DeVries, Ann. Rev. Mater. Sci. **17**, 161 (1987).

   K. E. Spear, J. Am. Ceram. Soc. **72**, 171 (1989).

   J. C. Angus and C. C. Hayman, Sci. **241**, 913 (1988).

2. Y. Cong, R. W. Collins, G. F. Epps, and H. Windischmann, Appl. Phys. Lett. **58**, 819 (1991).

3. B. J. Waclawski, D. T. Pierce, N. Swanson, and R. J. Celotta, J. Vacuum Sci. Technol. 21, 368 (1982).

4. S.-Tong Lee and G. Apai, Phys. Rev. B. **48**, 2684 (1993).

5. Takashi Aizawa, Toshihiro Ando, Mutsukazu Kamo, and Yoichiro Sato, Phys. Rev. B **48**, 18348 (1993).

6. A. V. Hamza, G. D. Kubiak, and R. H. Stulen, Surf. Sci. **206**, L833 (1988).

   A. V. Hamza, G. D. Kubiak, and R. H. Stulen, Surf. Sci. **237**, 35 (1990).

   G.D. Kubiak, M.T. Schulberg, and R.H. Stulen, Surf. Sci., **277**, 234 (1992).

7. Y. Mitsuda, T. Yamada, T.J. Chuang, H. Seki, R.P. Chin, J.Y. Huang, Y.R. Shen, Surf. Sci. Lett., **257**, L633 (1991)

8. R.P. Chin, J.Y. Huang, Y.R. Shen, T.J. Chuang, H. Seki and M. Buck, Phys. Rev. B **45**, 1552 (1992).

9. J.E. Butler, Material Research Society Spring 1992 Meeting.

10. Y.R. Shen, Nature (London) **337**, 519 (1989) and references therein.

    Y.R. Shen, Surface Science, **299/300**, 551 (1994) and references therein.

11. J. H. Hunt, P. Guyot-Sionnest, and Y. R. Shen, Chem. Phys. Lett. **133**, 189 (1987).

12. P. Guyot-Sionnest, R. Superfine, J. H. Hunt, and Y. R. Shen, Chem. Phys. Lett. **144**, 1 (1988).

13. X. D. Zhu, H. Suhr, and Y. R. Shen, Phys. Rev. B **35**, 3047 (1987).

14. K. M. Gough, J. Chem. Phys. **91**, 2424 (1989).

15. System based upon: J.Y. Zhang, J.Y. Huang, Y.R. Shen, & C. Chen, J. Opt. Soc. Am. B, **10,** 1758 (Sept. 1993).

16. B. B. Pate, Surf. Sci. **165**, 83 (1986).

17. J. N. Smith, Jr. and W. L. Fite, J. Chem. Phys. **37**, 898 (1962).

18. R.P. Chin, X. Blase, Y.R. Shen, and S.G. Louie, to be published.

19. S.A. Solin and A.K. Ramdas, Phys. Rev. B, **1**, 1687 (1970).

20. D. C. McKean, J. L. Duncan, and L. Batt, Spectrochimica Acta **29A**, 1037 (1973).

21. J.K. Wilmshurst and H.J. Berstein, Can. J. Chem. **35**, 969 (1957).

22. Xuejun Zhu and Steven G. Louie, Phys. Rev. B, **45**, 3940 (1992).

    R.P. Chin, X. Blase, Y.R. Shen, S.G. Louie, to be published.

23. A concurrent system studying the diamond (111) surface by conventional UHV techniques of Low Energy Electron Diffraction (LEED), Auger spectroscopy, X-ray Photoemission Spectroscopy (XPS), and Temperature Programmed Spectroscopy (TPD) using mass spectrometry were performed by T.J. Chuang and H. Seki at the IBM Almaden Research Center, San Jose, CA.

24. B. G. Koehler, C. H. Mak, D. A. Arthur, P. A. Coon, and S. M. George, J. Chem. Phys. **89**, 1709 (1988).

25. K.C. Pandey, Phys. Rev. B, **25,** 4338 (1982).

    D. Vanderbilt and S.G. Louie, Phys. Rev. B, **30**, 6118 (1984).

    F. Bechstedt and D. Reichardt, Surf. Sci., **202**, 58 (1988).

    G.D. Kubiak and K.W. Kalasinski, Phys. Rev. B, **39,** 1381 (1989).

    S. Iarlori, G. Galli, F. Gygi, M. Parrinello, and E. Tosatti, Phys. Rev. Lett., **69**, 2947 (1992).

26. H. Froitzheim, H. Lammering, & H.L. Gunter, Phys. Rev. B **27**, 2278 (1983).

27. G. Vidali and D.R. Frankl, Phys. Rev. B, **27**, 2480 (1983).

    G. Vadali, M.W. Cole, W.H. Weinberg, and W.A. Steele, Phys. Rev. Lett. **51**, 118 (1983).

28. G. D. Kubiak, J. Butler, private communications.

29. A. Kindness, D.C. McKean, and D. Stewart, J. Mol. Struct., **224**, 363 (1990) and references therein.

30. Brian D. Thoms, John N. Russell, Jr., Pehr E. Pehrsson, and James E. Butler, J. Chem. Phys., **100**, 8425 (1994).

31. K. Sinniah, M. G. Sherman, L. B. Lewis, W. H. Weinberg, J. T. Yates, and K. C. Janda, Phys. Rev. Lett. **62**, 567 (1989) ; J. Chem. Phys. 92, 5700 (1990).

32. John J. Boland, Phys. Rev. Lett. **67**, 1539 (1991).

M.L. Wise, B.G. Koehler, P. Gupta, P.A. Coon, and S.M. George, Surf. Sci. **258**, 166 (1991).

33. G.A. Reider, U. Höfer, and T.F. Heinz, J. Chem. Phys. **94**, 4080 (1991)

34. H. Ibach, Phys. Rev. Lett. **27**, 253 (1971).

N.J. DiNardo, W.A. Thompson, A.J. Schell-Sorokin, and J.E. Demuth, Phys. Rev. B **34**, 3007 (1986).

R.E. Shroder, R.J. Nemanich, and J.T. Glass, Phys. Rev. B **41**, 3738 (1990).

U. Harten, J.P. Toennies, and Ch. Woll, Phys. Rev. Lett. **57**, 2947 (1986).

35. O.L. Alerhand, D.C. Allen, and E.J. Mele, Phys. Rev. Lett. **55**, 2700 (1985).

O.L. Alerhand and E.J. Mele, Phys. Rev. Lett. **59**, 657 (1987); Phys. Rev. B **37**, 2536 (1988).

L. Miglio, P. Ruggerone, and G. Benedek, Phys. Rev. Lett. **62**, 3070 (1989).

L. Miglio, P. Ruggerone, and G,Benedek, J. Electron Spectrosc. Relat. Phenom. **44**, 281 (1987).

W. Goldammer and W. Ludwig, Phys. Lett. A **133**, 85 (1988).

W. Goldammer, W. Ludwig, W. Zierau, and C. Falter, Surf. Sci. **141**, 139 (1984).

36. S. Matsumoto, Y. Sato, M. Kamo and N. Setaka, Jpn. J. Appl. Phys. **21**, L183 (1982).

37. G. Herzberg, *Infrared and Raman Spectra of Polyatomic Molecules* (Van Nostrand, Princeton, NJ, 1945).

N.B. Colthup, L.H. Daly, and S.E. Wiberley, *Introduction to Infrared and Raman Spectroscopy* (Academic, New York, 1990).

Figures

Fig. 1. (a) The hydrogen terminated C(111) surface. (b) The reconstructed (2x1) surface.

Fig. 2. SHG signal versus atomic hydrogen exposure time with (a) P-in P-out and (b) S-in P-out polarization combination.

Fig. 3. SHG signal versus maximum desorption temperature for P-in P-out polarization geometry.

Fig. 4. SFG spectra of a well annealed H-terminated C(111)-(1x1) surface, obtained with different polarization combinations: solid squares for the s (sum-frequency, output) - s (visible, input) - p (infrared, input) polarization combination, open squares for the pss combination, and open circles for the sps combination.

Fig. 5. SFG spectra of the H-terminated H/C(111)-(1x1) surface showing the CH bending mode (open circles) and the same surface dosed with atomic deuterium (open squares). Both curves are for ssp polarization geometry.

Fig. 6. SFG spectra (ssp) of CH bending and stretching modes for H/C(111) at 300 K (open circles) and 700K (open squares).

Fig. 7. SFG spectra of H/C(111) from a freshly formed (1x1) surface with different surface H coverages: 42% ML (open squares); 51% ML (open circles); 68% ML (filled triangles); 77% ML (filled circles). The (2x1) to (1x1) phase transition was induced by H adsorption. The H coverage were estimated from the overall strength of the resonant modes using the full H coverage as a reference.

Fig. 8. SFG spectra of H/C(111) from a fully relaxed (1x1) surface with different surface H coverages resulting from thermal desorption: 100% ML (solid squares); 49% ML (open squares); 29% ML (open circles); 14% ML (open triangles).

Fig. 9. (a) SFG spectra (ssp) showing gradual replacement of D by H upon atomic H dosing onto the fully D-terminated surface. Full D coverage (open squares), 3 min H dosing (open triangles), 8 min H dosing (solid triangles), 13 min H dosing (open circles), 18 min H dosing (solid circles). (b) Illustration of the two step abstraction and adsorption process for isotopic conversion of the surface.

Fig. 10. Surface coverage of H as a function of H dosing time for atomic H dosing onto a bare reconstructed (2x1) surface (open circles) and onto a fully covered deuterium surface (open triangles).

Fig. 11. Variation of surface coverage of H (open squares) in response to the prescribed thermal desorption cycle shown in the lower figure. The dashed lines represent the theoretical fit using Eqn. (3.6).

Fig. 12. SFG spectra of the bare, reconstructed C(111)-(2x1) surface for ssp (upper curve), ppp (middle curve), and sps (lower curve) polarization geometries. Spectral features come from C-C surface vibrational modes.

Fig. 13. (a) Schematic representation of the Pandey π-bonded chain model showing the CC bonds. (b) Dimerization (no buckling) in the Pandey π-bonded chain model proposed by Iarlori *et al.* (c) Slight buckling (no dimerization) in the Pandey π -bonded chain model proposed by Bechstedt and Reichardt.

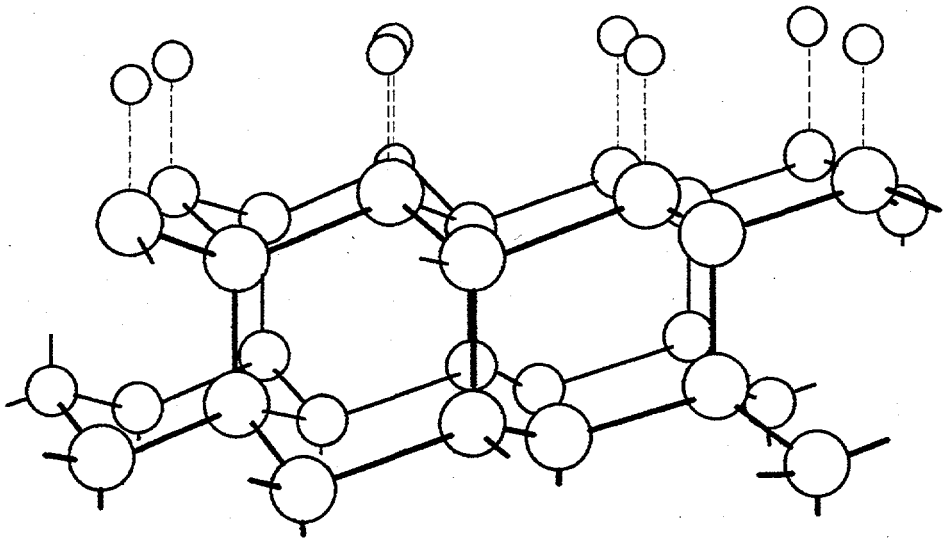

(a)

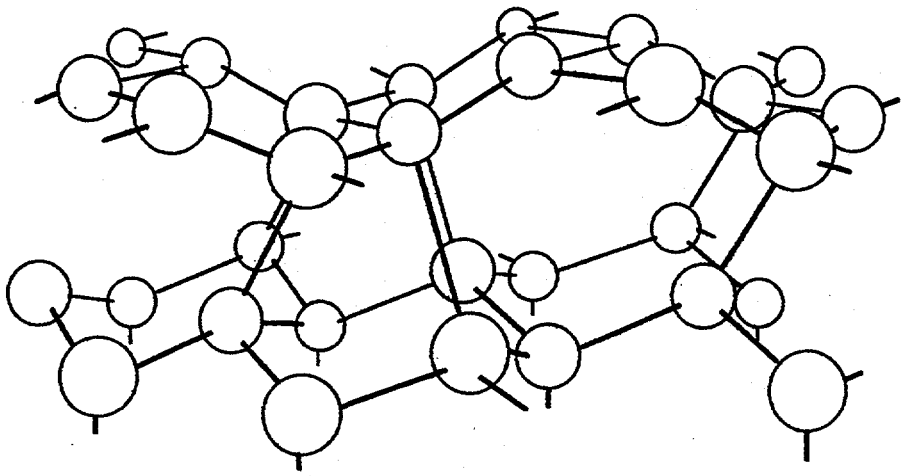

(b)

Fig. 1

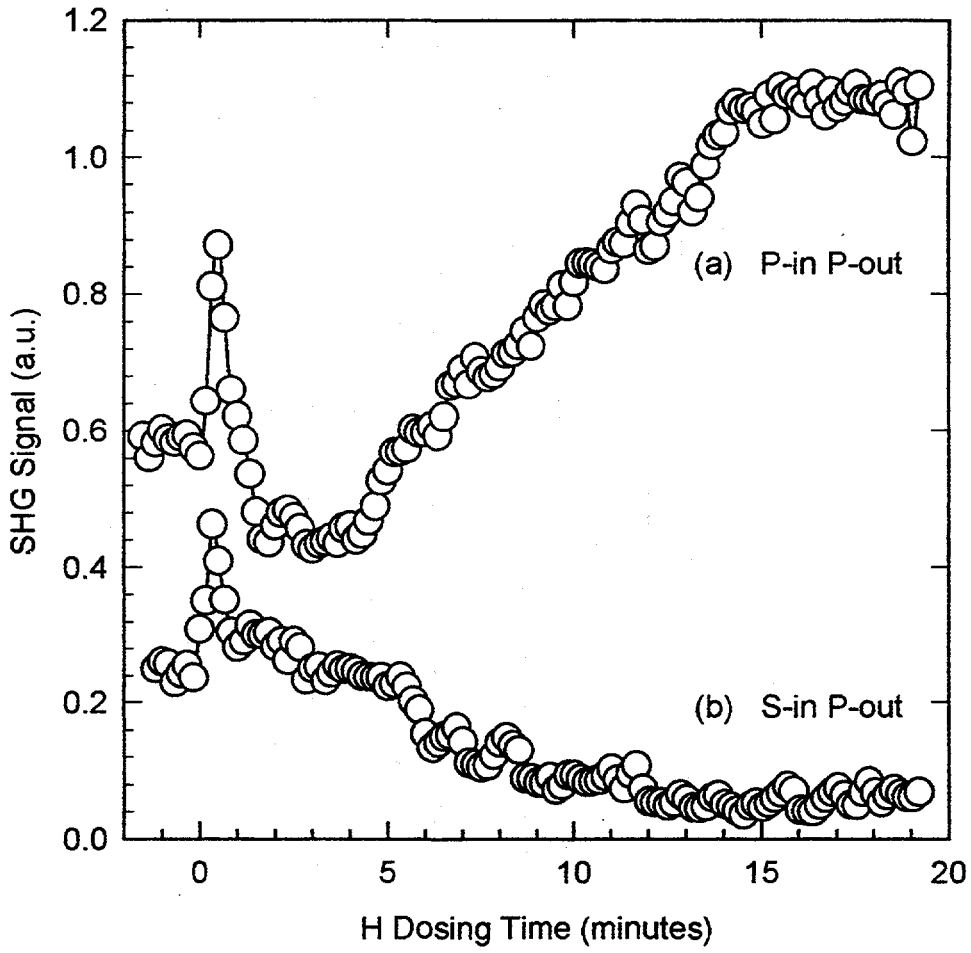
1.2
1.0
0.8
0.6
0.4
0.2
0.0
SHG Signal (a.u.)
0
5
10
15
20
H Dosing Time (minutes)
(a) P-in P-out
(b) S-in P-out

Fig. 2

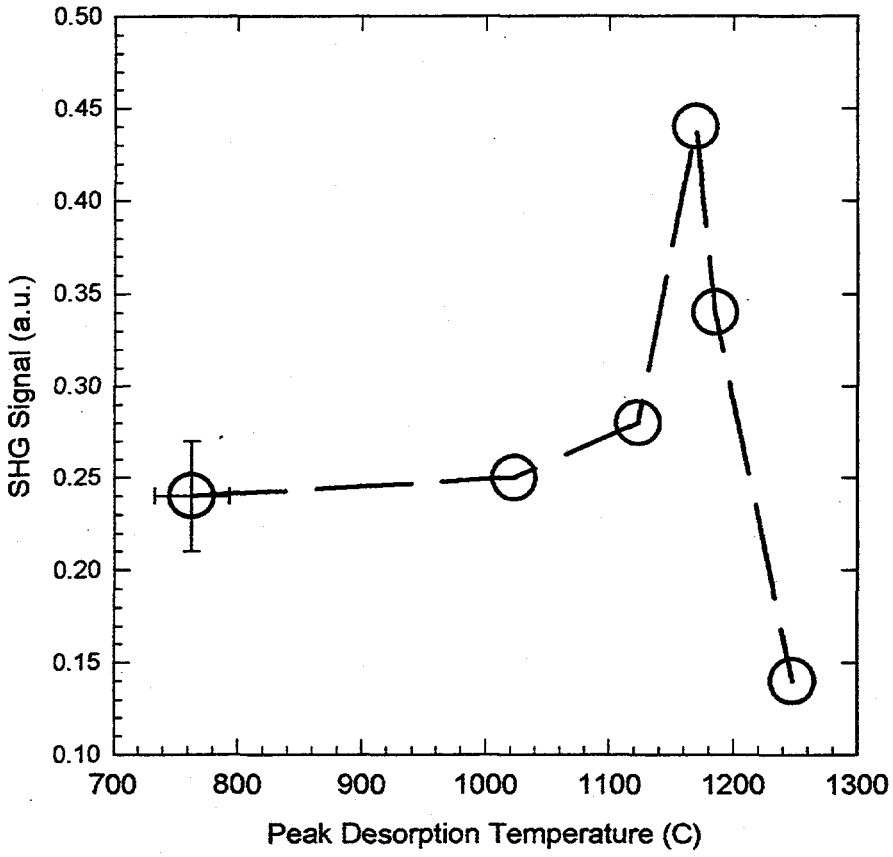
0.50
0.45
0.40
0.35
0.30
0.25
0.20
0.15
0.10
SHG Signal (a.u.)
700
800
900
1000
1100
1200
1300
Peak Desorption Temperature (C)

Fig. 3

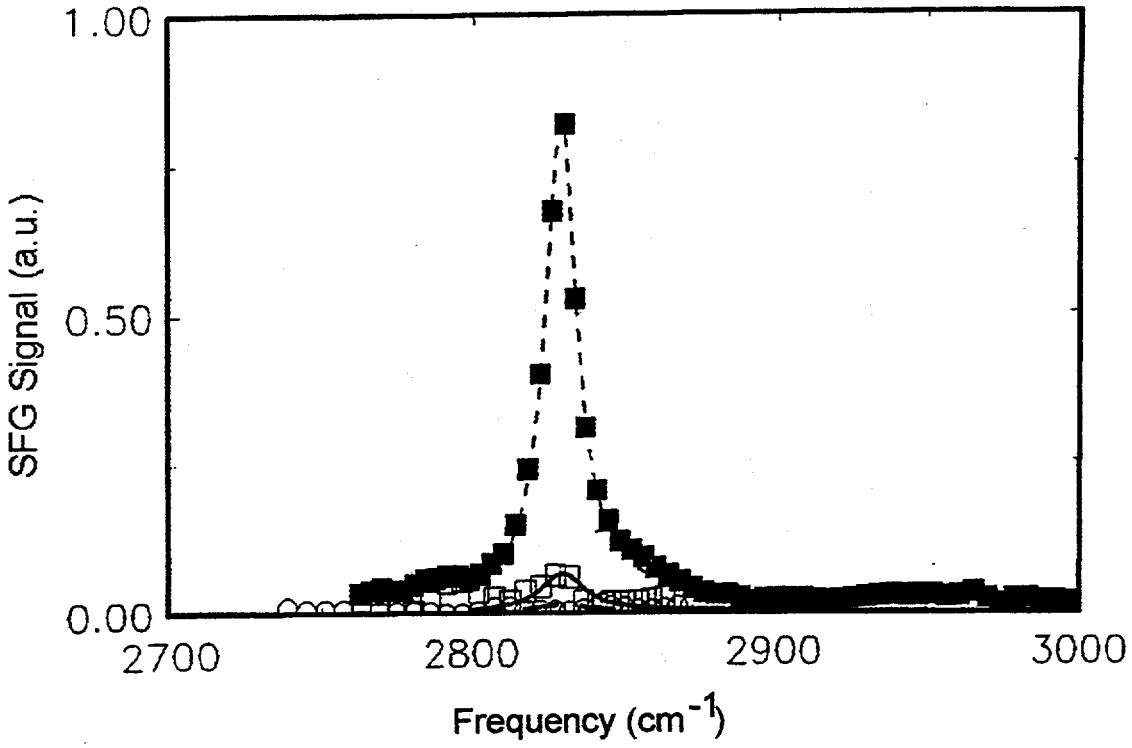

Fig. 4

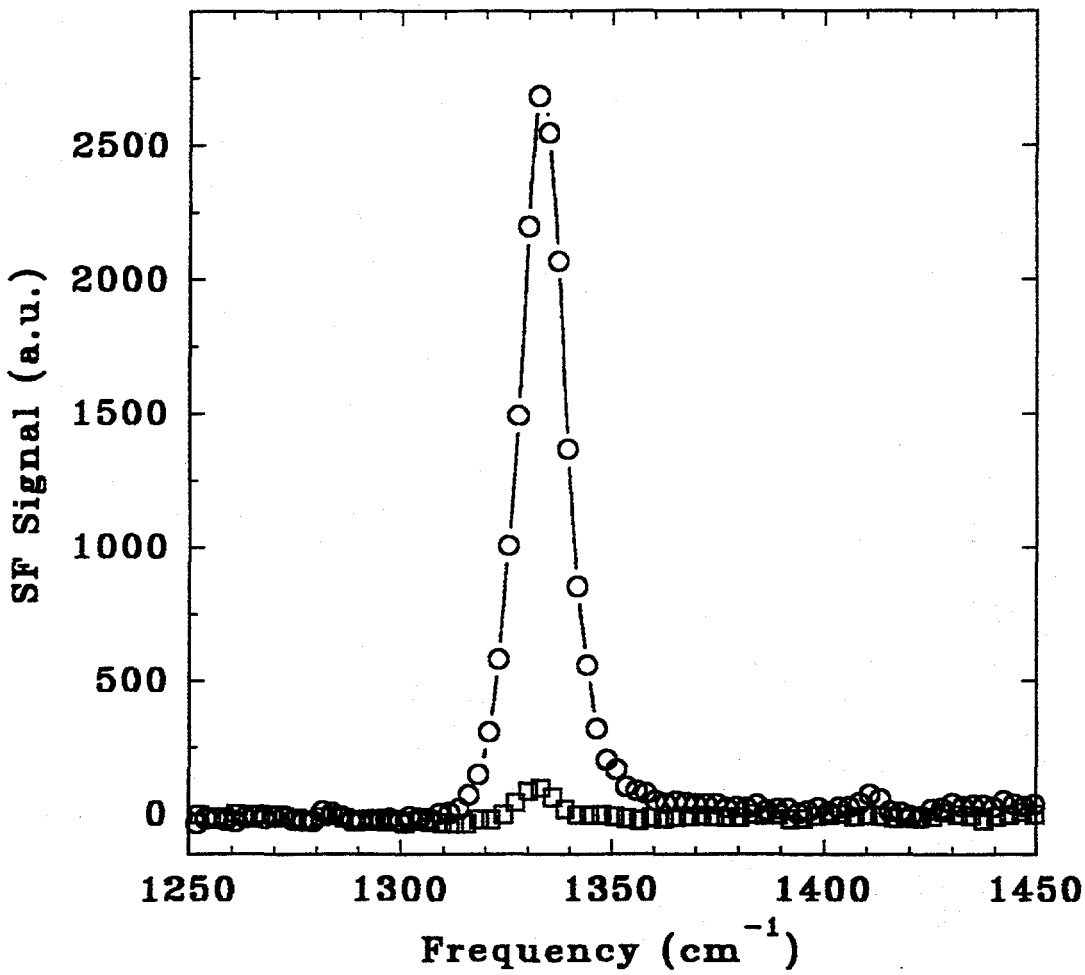
SF Signal (a.u.)
2500
2000
1500
1000
500
0
1250
1300
1350
1400
1450
Frequency (cm^{-1})

Fig. 5

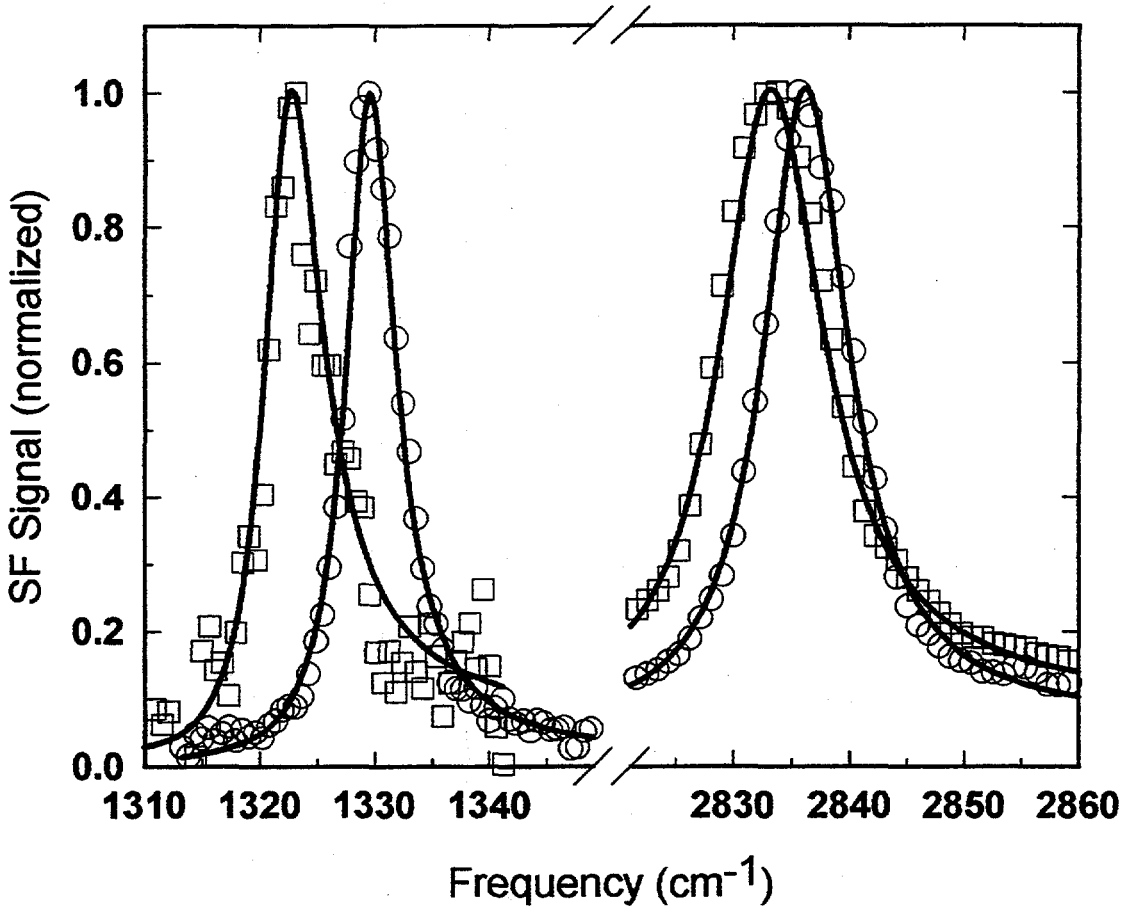
SF Signal (normalized)
1.0
0.8
0.6
0.4
0.2
0.0
1310
1320
1330
1340
2830
2840
2850
2860
Frequency (cm-1)

Fig. 6

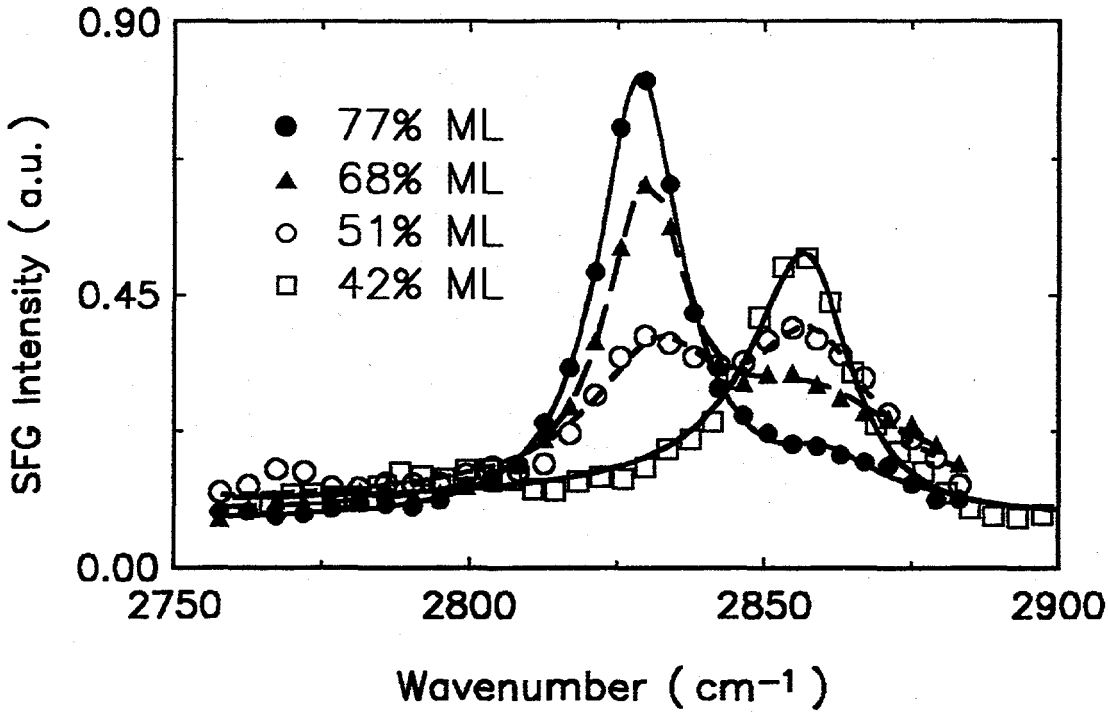
0.90
0.45
0.00
SFG Intensity (a.u.)
77% ML
68% ML
51% ML
42% ML
2750
2800
2850
2900
Wavenumber (cm^{-1})

Fig. 7

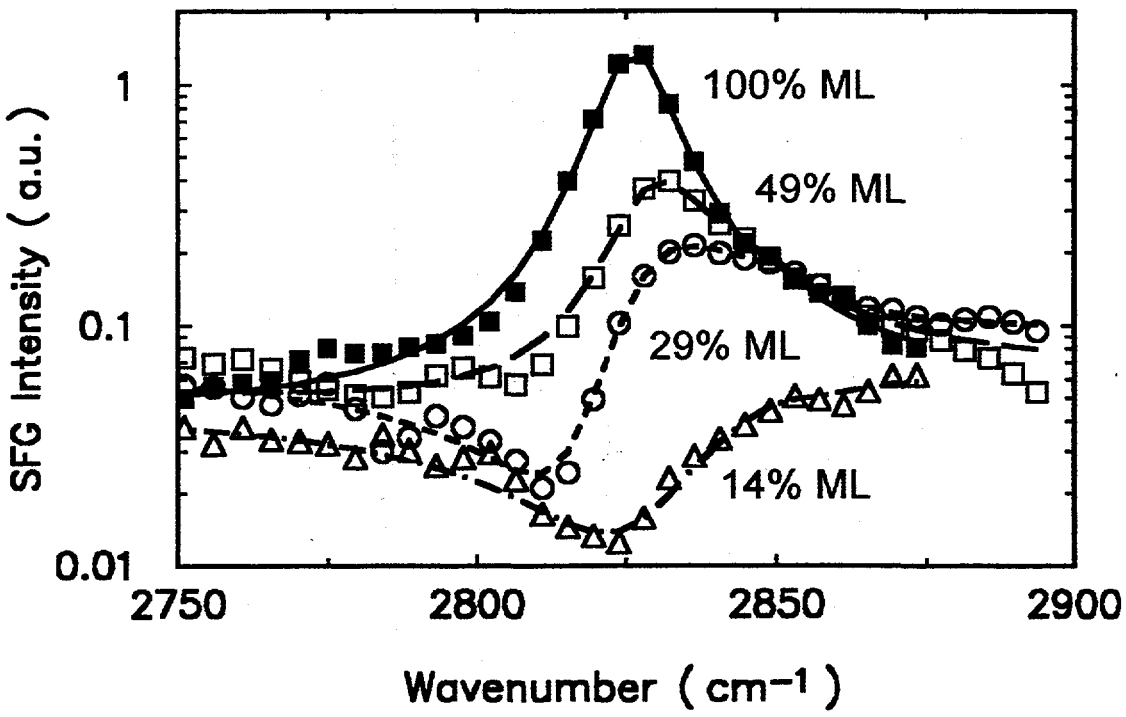
SFG Intensity (a.u.)
1
0.1
0.01
2750
2800
2850
2900
Wavenumber (cm^{-1})
100% ML
49% ML
29% ML
14% ML

Fig. 8

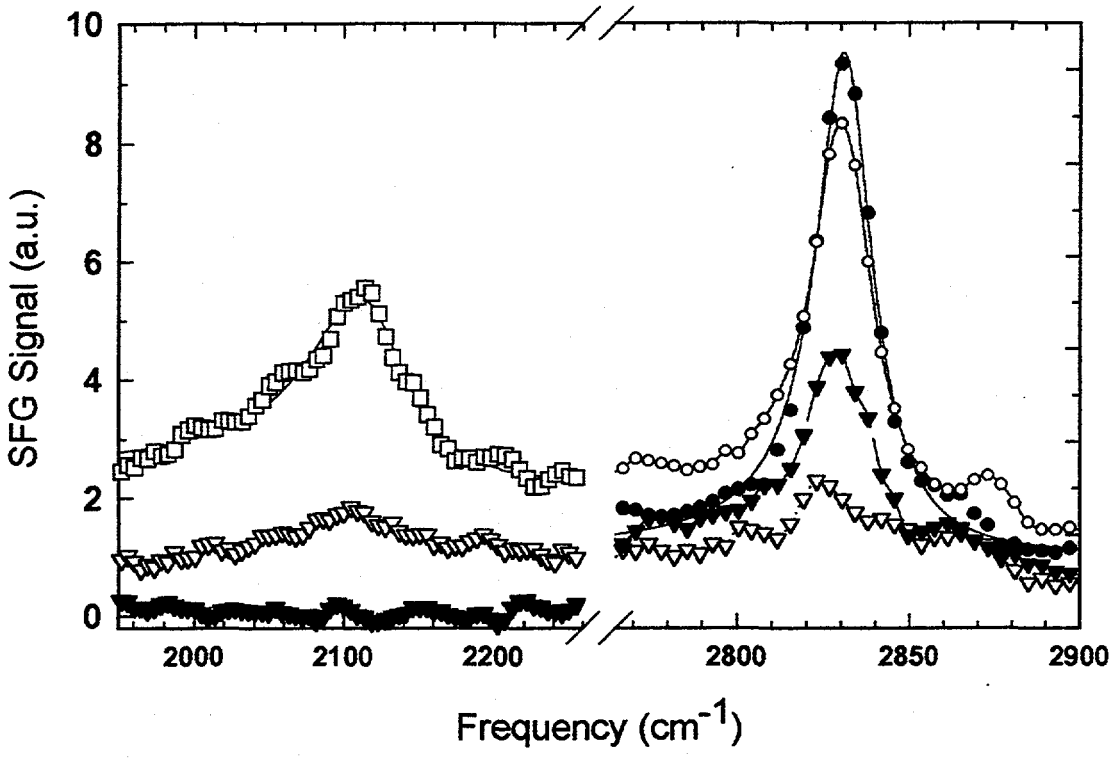
SFG Signal (a.u.)
10
8
6
4
2
0
2000
2100
2200
2800
2850
2900
Frequency (cm-1)

(a)

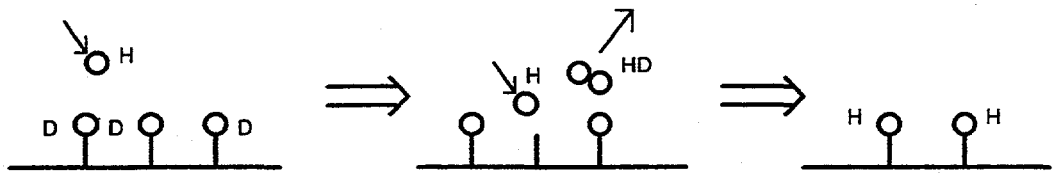
H
D
D
D
H
HD
H
H

(b)

Fig. 9

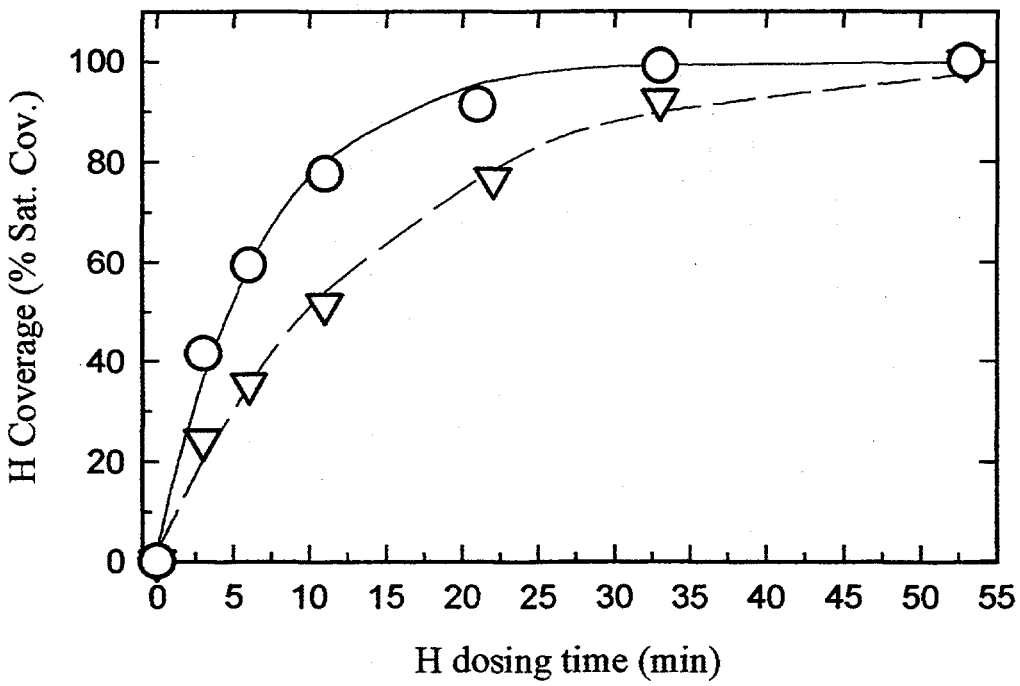
H Coverage (% Sat. Cov.)
100
80
60
40
20
0
0
5
10
15
20
25
30
35
40
45
50
55
H dosing time (min)

Fig. 10

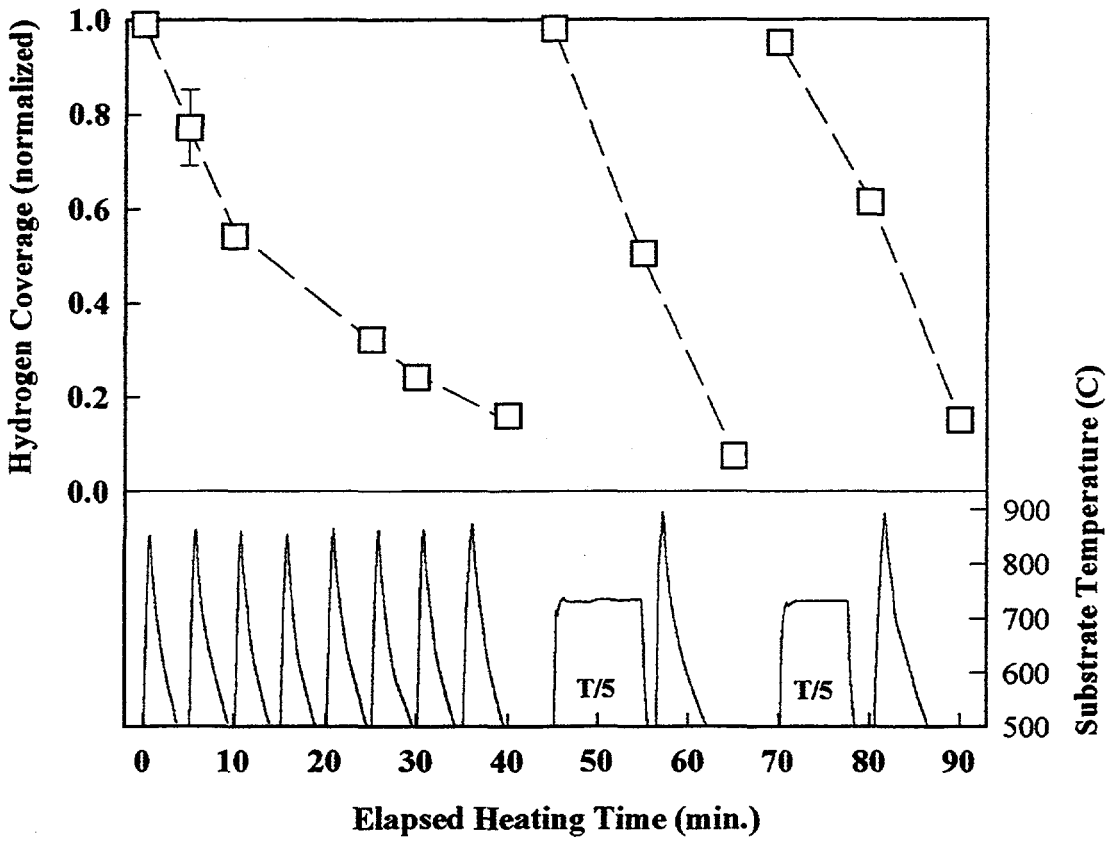
Hydrogen Coverage (normalized)
1.0
0.8
0.6
0.4
0.2
0.0
T/5
T/5
900
800
700
600
500
Substrate Temperature (C)
0
10
20
30
40
50
60
70
80
90
Elapsed Heating Time (min.)

Fig. 11

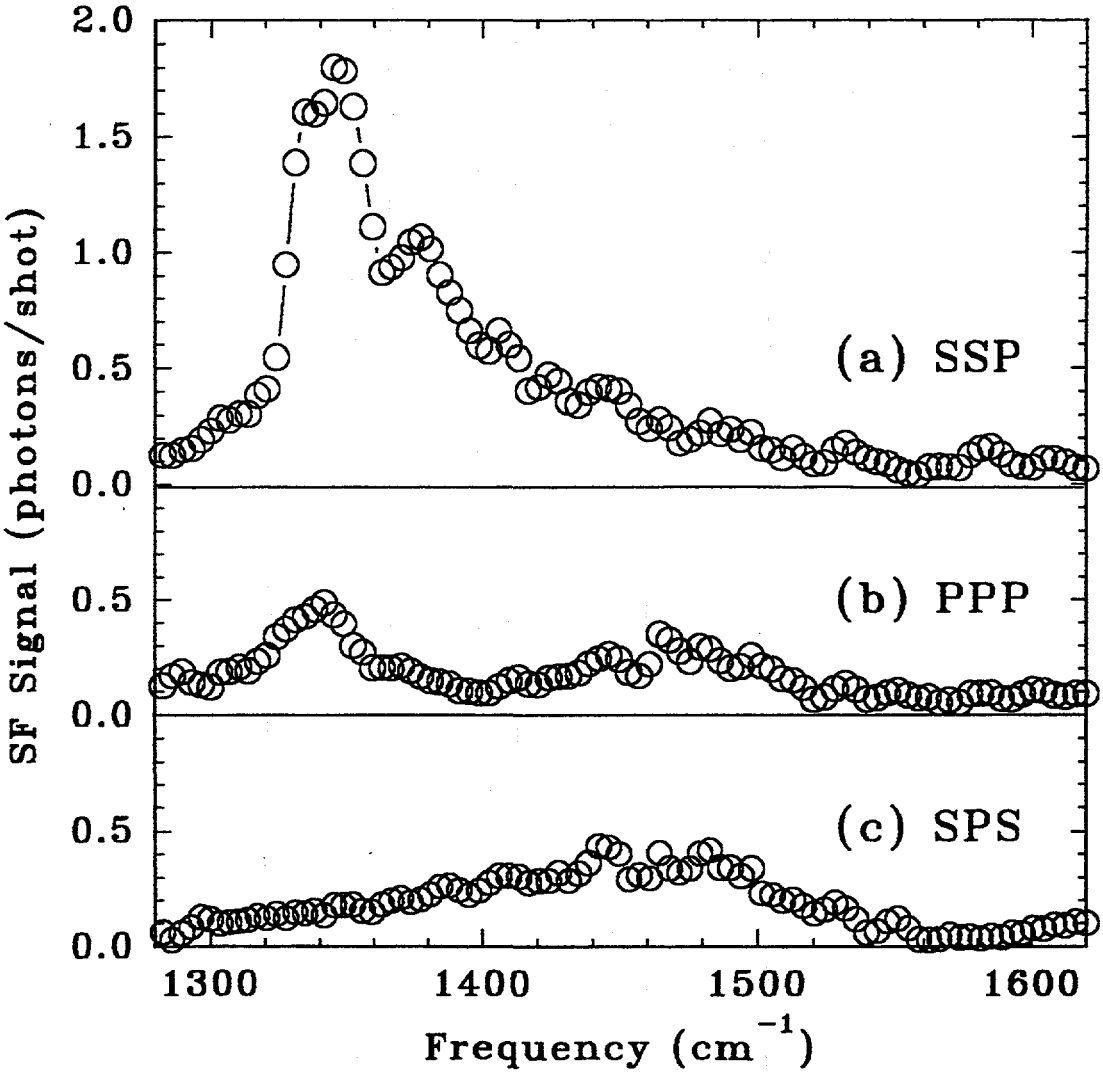
2.0
1.5
1.0
0.5
0.0
SF Signal (photons/shot)
(a) SSP
0.5
0.0
(b) PPP
0.5
0.0
(c) SPS
1300
1400
1500
1600
Frequency (cm^{-1})

Fig. 12

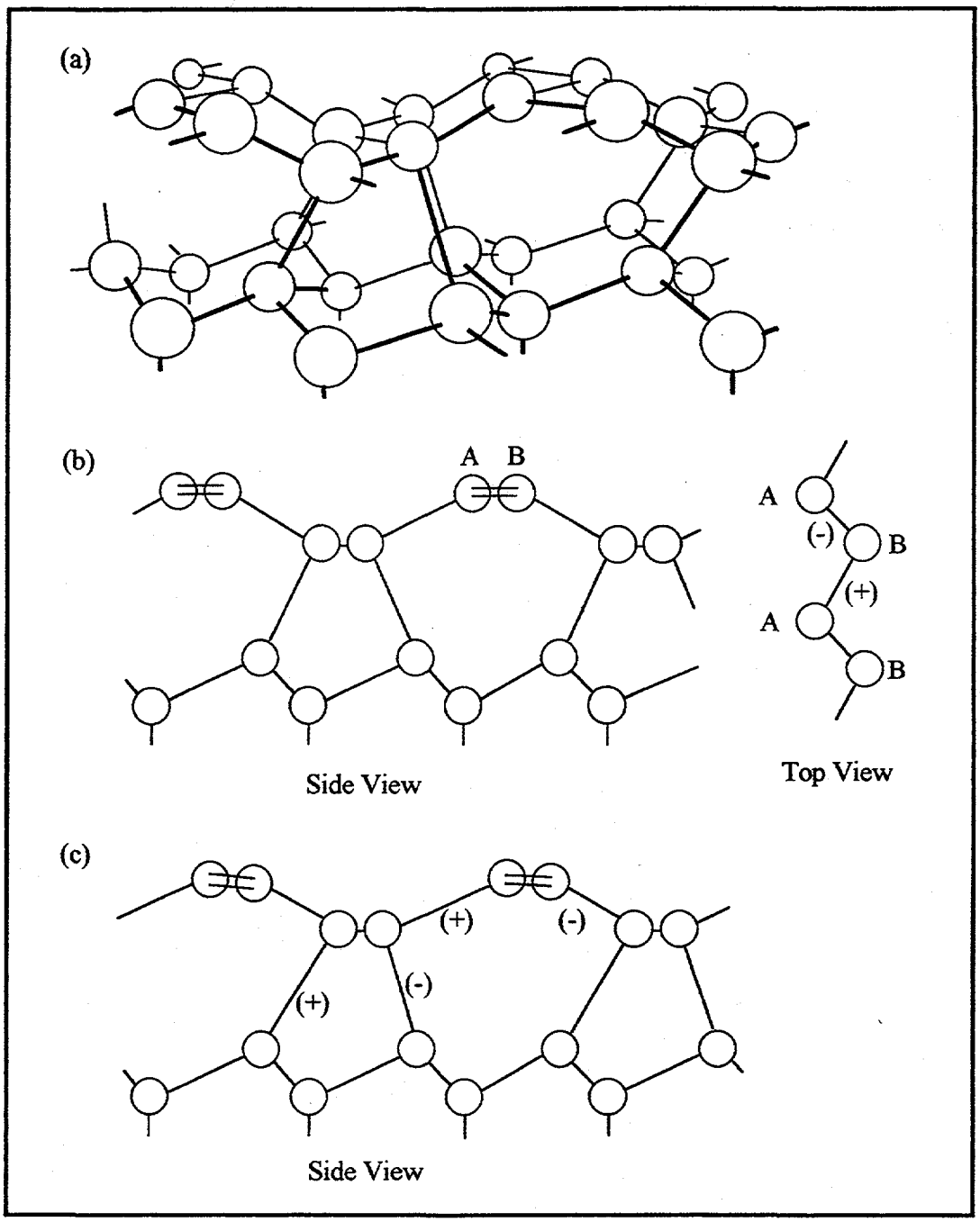

Fig. 13

IV. Anharmonicity and Lifetime of the CH Stretch Mode on Diamond H/C(111)-(1×1)

A. Introduction

Hydrogen on diamond has been a subject of great interest owing to the major role it plays in chemical vapor deposition of diamond thin films.[1] Vibrational spectra of hydrogen on various faces of diamond are considered most important as they yield direct information about the surface structure and binding of the adsorbate. However, because of the limitations of available techniques, they have not yet been well studied. Infrared spectroscopy seems to have hardly enough sensitivity to obtain such spectra from ordinary diamond samples. Electron energy loss spectroscopy (EELS) has the needed sensitivity, but its poor resolution makes interpretation of the spectra difficult. On the H/C(111) surface, *single* resonant peaks for the CH stretching (2838 cm^{-1}) and wagging (1331 cm^{-1}) modes were observed (Ch. III), indicating that H was adsorbed at diamond top sites. Assessment of the fundamental normal modes by infrared sum frequency generation spectroscopy has given much information about the surface binding sites and configuration. However, since chemical reactions are dynamical processes involving the making and breaking of chemical bonds, characteristics such as the bond's dissociation energy and its energy relaxation need to be investigated. In this chapter, extensions of the SFG measurements were performed to study the anharmonicity and vibrational relaxation of the CH stretch. For both surface sensitivity and high resolution, we use an infrared pump and probe scheme where the higher vibrational levels are probed exploiting the highly surface sensitive infrared SFG technique.

The CH bond energy may be measured by techniques such as temperature programmed desorption.[2] By infrared spectroscopy alone, the determination of the bond

energy may be estimated by the bond's anharmoncity[3]. This traditionally required the probing of higher vibrational levels using overtone or combination band spectroscopies. Unfortunately, these tend to be weak due to their higher order processes and are essentially undetectable for monolayers. EELS has shown high surface sensitivity but its poor resolution cannot distinguish the higher level overtones from the multiple losses processes.[4]

These characteristics give an indication as to the possibility of a two-phonon bound state such as observed on the H/Si(111) surface.[5] A two-phonon bound state where two vibrational quanta are localized over only a few neighboring bonds is favored for a large anharmonicity and small lateral interaction (dispersion).[6] With the high resolution spectroscopy, these characteristics may be quantified to predict the existence of a two-phonon bound state.

Here, experimentally an anharmonicity of 110 cm^{-1} was observed which is much larger than the expected interaction energy between two neighboring CH vibrations. Thus, the observed "$\nu = 1 \rightarrow 2$" peak should correspond to an excitation of the two-phonon bound state. Also, the excited vibrational energy was found to relax directly to the ground state with a relaxation time of 19 psec. The results are compared with theoretical calculations. Agreement between theory and experiment provides confidence to the surface potential for H on C(111) used in the calculation. Important surface properties such as the desorption energy and mobility of H can then be deduced from this surface potential.

The determination of the energy relaxation time (T_1) of the adsorbate-substrate vibration may not be so easily assessed. Originally, the linewidth of the adsorbate-substrate vibration was thought to be dominated by the T_1 lifetime. However, subsequent temperature dependence measurements revealed the linewidth can be dominated by pure dephasing. Moreover, there can be additional broadening due to inhomogeneous

mechanisms.[7] The separation of the contributions to obtain the T_1 relaxation item is difficult at best. A direct determination of the T_1 lifetime is then desirable. This is accomplished using a picosecond time-resolved infrared pump *then* probe arrangement.

B. Experiment

The experimental setup have been described elsewhere.[8] In the present experiment, three beams of picosecond pulses, one visible and two tunable-infrared around 3.5 μm, one (17 psec, 12 cm^{-1} linewidth) for pumping, and the other for probing (8 psec, 4.5 cm^{-1} linewidth) were used. They were overlapped on the surface with beam diameters (energy densities) of ~500 μm (~10 GW/cm^2), ~300 μm (~25 GW/cm^2), and ~260 μm (~10 GW/cm^2), respectively. The SFG signals associated with the IR pump and probe were spatially separated. Details of the sample preparation were described in Chapter III.

C. Anharmonicity and Lifetime Determination

Once the hydrogen terminated surface was prepared, the usual CH monohydride peak was observed at ~2838 cm^{-1}. Before the two-color experiment below was performed, the saturation of the SFG CH peak signal for a single infrared beam for the ssp polarization combination (SF output, visible input, IR input are s-, s-, and p-polarized, respectively) was observed. This would indicate a significant population transfer from the ground $\nu = 0$ state to the upper $\nu = 1$ vibrational state. This effect would be expected only if the vibrational relaxation time was long-lived and the infrared intensity was

sufficient enough. As Fig. 1 illustrates, a very high infrared intensity was needed to cause saturation to occur. Figure 2(a) illustrates the SFG process when the probe is resonant with the fundamental or the hot band transitions.

The SFG vibrational (probe) spectra of the H-covered C(111) in the CH stretch region, obtained by the ssp polarization combination were presented in Fig. 3(a). Without the IR pump excitation, a single sharp peak with an intrinsic 4 cm^{-1} halfwidth appears at 2838 cm^{-1}. This peak has been previously identified as the fundamental CH stretch vibration of monohydrides arising from the H-terminated C(111)-(1x1) surface.[9] With the IR pump excitation to populate the v=1 state of the CH stretch mode, the 2838 cm^{-1} peak reduces in strength, but an additional peak appears at 2728 cm^{-1} with a 20 cm^{-1} halfwidth. It was obvious that the 2728 cm^{-1} peak corresponds to the $v=1 \rightarrow v=2$ overtone transition of the CH stretch mode. This yields an anharmonicity of 110 cm^{-1} for the CH stretch. As shall be explained later, the v=2 state here can be identified as a two-phonon bound state. The spectra in Fig. 3(a) can be fit by the expression:

$$S \propto \left|\chi_S\right|^2 = \left|\chi_{NR} + \sum_q \frac{A_q}{(\omega_{IR} - \omega_q - i\Gamma_q)}\right|^2 \qquad (4.1)$$

convoluted with a gaussian laser lineshape of 4.5 cm^{-1} in full width at half maximum, where χ_S is the surface nonlinear susceptability responsible for the SFG, χ_{NR} is the nonresonant contribution to χ_S, and A_q, ω_q, and Γ_q are the amplitude, frequency, and damping coefficient, respectively, of the q^{th} resonant mode contributing to χ_S. From the fits to both spectra shown in Fig. 3(a) (solid lines), the parameters for the CH fundamental and overtone vibrational resonances were deduced, as shown in the table below.

	A_{01}	A_{12}	ω_{01} (Γ_{01})	ω_{12} (Γ_{12})
Without IR Pump	1	—	2838 ± 2 cm^{-1} (6 cm^{-1})	—
With IR Pump	0.6	0.2	2836 ± 2 cm^{-1} (7 cm^{-1})	2728 ± 3 cm^{-1} (20 cm^{-1})

Knowing the fundamental frequency (2838 cm^{-1}) and the anharmonicity (-110 cm^{-1}) of the CH stretch mode, the dissociation energy of the bond can be estimated assuming a Morse potential[3] $V(R) = D_e\{1-\exp[-a(R-R_e)]\}^2$, where D_e is the dissociation energy for $R\rightarrow\infty$ and the potential energy is zero at $R=R_e$. This yields a dissociation energy of 4.9±0.2 eV which is slightly more than a typical aliphatic CH bond (4.6 eV). For comparison, the thermal desorption spectroscopy experiments (CH. III) yielded a dissociation energy of 4.0 (±0.4) eV.

One can find the population excited to the $v=1$ level by the IR pump from the ratio of A_{12} and A_{01}, where the sub-indices 12 and 01 denote the overtone and fundamental vibrational resonances, respectively. From the microscopic expression of χ_S, it is known that for the $v=j\rightarrow v=j+1$ vibrational transition:

$$A_{j,j+1} \propto \left(\frac{\partial\mu}{\partial x}\right)_{j,j+1}\left(\frac{\partial\alpha}{\partial x}\right)_{j,j+1}(\rho_j-\rho_{j+1}) \qquad (4.2)$$

Here, $\left(\frac{\partial\mu}{\partial x}\right)_{j,j+1}$ and $\left(\frac{\partial\alpha}{\partial x}\right)_{j,j+1}$ are infrared dipole moment and Raman polarizability for the transition, respectively, and ρ_j is the population of the $v=j$ level. Both $\left(\frac{\partial\mu}{\partial x}\right)_{j,j+1}$ and $\left(\frac{\partial\alpha}{\partial x}\right)_{j,j+1}$ are proportional to $(j+1)^{1/2}$ in the harmonic oscillator approximation for the vibration. Then, one finds with IR pump excitation, $A_{12}/A_{01}=2\rho_1/(1-2\rho_1)$. In reference to the strength A_{01}^o in the absence of IR pump, we have $A_{12}/A_{01}^o=2\rho_1$ and

$A_{01}/A_{01}^{o} = 1 - 2\rho_1$. The values of A_{01}^{o}, A_{01}, and A_{12} in the above table yield consistently an average excited state population of $\rho_1 = 0.13 \pm 0.05$ obtained under 17 psec IR pump excitation of 25 GW/cm^2.

Monitoring how the population distribution after pumping returns to thermal equilibrium allows us to measure the vibrational lifetime T_1 of the $v = 1$ excited state as well as the recovery time T_1' of the ground-state population. In the experiment, the former was obtained by probing the decay of resonant SFG from the $v = 1 \rightarrow v = 2$ transition as a function of time delay between IR pump and probe, and the latter by probing the recovery of resonant SFG from the $v = 0 \rightarrow v = 1$ transition. In an ideal case, the pump and probe pulses are much shorter than the relaxation. This then results in a clear response for the fundamental and the hot band transitions reflecting their respective populations after the inital pump (as illustrated in Fig. 2(b)). The experimental results were presented in Fig. 4. For the $v = 1 \rightarrow v = 2$ transition, $A_{12}(t) \propto \int_{-\infty}^{t} I_{pu}(t') \exp[-(t-t')/T_1]\, dt'$ with $I_{pu}(t')$ being the intensity of the IR pump pulse. Substituting $A_{12}(t)$ for A_q in Eqn. (4.1) and calculating S(t) by convoluting $|\chi_S(t)|^2$ with the temporal profiles of the IR and visible probe pulses, the data was fit as shown in Fig. 4 with T_1 as the adjustable parameter. This yields $T_1 \approx 19 \pm 5$ psec.

To fit the data for the $v = 0 \rightarrow v = 1$ transition, the same procedure could be used. However, in this case, the coherent artifact that arises from coherent interactions[10] between the IR pump and probe should affect $A_{01}(t)$ and hence the SFG signal around zero time delay. It is known that if the vibrational dephasing time T_2 is less than half of the pump pulsewidth τ_p, the coherent artifact becomes negligible after a pump / pulse delay time of $\sim \tau_p$. In our case, we have $T_2/\tau_p \approx 0.1$ assuming the 2836 cm^{-1} resonance is homogeneously broadened because the peak was found to broaden with temperature as

shown in Chapter III. By fitting the data points at longer time delays, we obtain $T_1' = 19 \pm 2$ psec. The result of $T_1 \cong T_1'$ shows that the excited $v = 1$ population must have relaxed directly to the $v = 0$ state without having spent an appreciable time in intermediate states.

D. Discussion

The experimental results have shown there is a very large anharmonicity suggesting the existence of a two phonon bound state where two vibrational quanta can be localized on one bond site to minimize their total energy. There are two prerequisites for the existence of a two phonon bound state: a large anharmonicity of the bond and a small lateral interaction (dispersion).

In order to confirm this, theoretical calculations were performed by X. Blase *et al.* First, their theoretical calculations used a slab model to study the vibrational modes of a full monolayer of H on the C(111)-(1×1) surface witihin an ab-initio pseudopotential LOA method. Technical details for the slab geometry, energy cut-off and pseudopotentials are described elsewhere.[11] Results for the theoretical[12] and experimental wagging and stretching frequencies are shown in Table I together with the overtone frequency -2Γ.

To study the extended and localized collective modes of the surface 2D hexagonal lattice of interacting C-H bonds, a Hubbard-like model[13] was used. The "negative U" on-site energy which induces the localization of two phonons on the same CH bond was taken to be Γ. The hopping parameter t, which originated in the CH bond-bond lateral interaction, was calculated within a first nearest neighbor tight-binding model for the hexagonal C-H bond surface lattice. In the model, $\omega(\overline{\Gamma}) - \omega(\overline{M}) = 8t$, where $\omega(\overline{\Gamma})$ and $\omega(\overline{M})$ are the one-phonon mode frequencies at the zone center ($\overline{\Gamma}$) and at the zone edge

($\overline{M}$). Through frozen-phonon calculations, they found that t = 0.25 cm^{-1}. The values of Γ and t yields a ratio Γ/t to be large for the H/C(111) surface. This suggests a strongly bound two-phonon bound state should exist in the present system.[6]

The inversion of the Hubbard equation was standard[14] and, for excitations with wavevector **Q**, yields (N-1) energies in the quasi-continuum of unbound two single-particle states $\omega_2(\mathbf{Q}) = \omega_1(\mathbf{k}) + \omega_1(\mathbf{Q}-\mathbf{k})$ and one (bound) solution $\omega_2(\mathbf{Q})$ out of this continuum. With the calculated values of t and Γ, the latter solution[12] was found to be located 110 cm^{-1} below the energy of two single phonons at $\overline{\Gamma}$. This corresponds to the two-phonon binding energy E_b for the H/C(111)-(1x1) surface. The observed peak at 110 cm^{-1} below the fundamental vibrational transition must therefore be associated with this excitation from the one-phonon state to the two-phonon bound state at $\overline{\Gamma}$. The agreement with experiment was excellent (see Table I). The dispersion of the two-phonon bound state band was calculated[12] to be 0.01 cm^{-1}. Both the large binding energy and the very small dispersion indicates a very localized two-phonon bound state.

For the vibrational lifetime of the v=1 CH vibration of H/C(111), Sun *et al.*[15] recently calculated a value of 60 psec at 300K. This is much faster than that of H/Si(111).[5,16,17] In the latter case, the longer lifetime (1.7 nsec theoretical, 0.8 nsec experimental) is attributed to a higher-order coupling (1:4 resonance) of the SiH stretch with one substrate phonon (~210 cm^{-1}) and three Si-Si-H bending quanta. In the case of H/C(111), the decay of the CH stretch vibration involves a lower-order coupling (1:3 resonance) with two C-C-H bending quanta and one substrate phonon mode of ~250 cm^{-1}. In the calculation, the CH bending mode frequency of 1290 cm^{-1} (from EELS data) was used, which was somewhat different from the value of 1331 cm^{-1} measured by SFG. A re-calculation of the $v = 1$ lifetime using the 1331 cm^{-1} bending mode frequency should yield a closer 1:2 resonance between CH stretching (2838 cm^{-1})

and bending frequencies and hence a shorter $v = 1$ lifetime which may agree better with the experimental result.

E. Conclusion

In conclusion, the hot band transition and anharmonicity of the first overtone of the CH stretch mode of the H/C(111)-(1×1) surface was observed. Agreement between theory and experiment provided strong evidence for the existence of a strong two-phonon bound state on the hydrogenated diamond (111) surface. By time-resolved pump and probe spectroscopy, the lifetime of the v=1 state was found to be 19 psec with a similar recovery time for the ground state population.

References

1. R. C. DeVries, Ann. Rev. Mater. Sci. **17**, 161 (1987); K. E. Spear, J. Am. Ceram. Soc. **72**, 171 (1989); J. C. Angus and C. C. Hayman, Sci. **241**, 913 (1988).
2. J.B. Miller, H.R. Siddiqui, S.M. Gates, J.N. Russel, Jr., J.T. Yates, J.C. Tully, and M.J. Cardillo, J. Chem. Phys. **87**, 6725 (1987).
3. G. Herzberg, *Infrared and Raman Spectra of Polyatomic Molecules* (Van Nostrand, Princeton, NJ, 1945).

   N.B. Colthup, L.H. Daly, and S.E. Wiberley, *Introduction to Infrared and Raman Spectroscopy* (Academic, New York, 1990).

   R.A. Alberty, *Physical Chemistry,* (Wiley, New York, 1987).
4. H. Ibach & D. Mills, *Electron Energy Loss Spectroscopy and Surface Vibrations* (Academic, San Francisco, 1982).
5. P. Guyot-Sionnest, Phys. Rev. Lett. **67**, 2323 (1991).
6. F. Bogani, J. Phys. C **11**, 1283 (1978); *ibid*, **11**, 1297 (1978).

   F. Bogani, R. Giua, V. Schettino, Chem. Phys. **88**, 375 (1984).

   J.C. Kimball, C.Y. Fong, and Y.R. Shen, Phys. Rev. B **23**, 4946 (1981).

   T. Holstein, R. Orbach, and S. Alexander, Phys. Rev. B **26**, 4721 (1982).
7. R.G. Tobin, Surf. Sci. **183**, 226 (1987).
8. J. H. Hunt, P. Guyot-Sionnest, and Y. R. Shen, Chem. Phys. Lett. **133**, 189 (1987).
9. R.P. Chin, J.Y. Huang, Y.R. Shen, T.J. Chuang, H. Seki and M. Buck, Phys. Rev. B **45**, 1552 (1992).
10. A.L. Harris and L. Rothenberg, J. Chem. Phys. **94**, 2449 (1991).
11. Xuejun Zhu and Steven G. Louie, Phys. Rev. B **45**, 3940 (1992).
12. R.P. Chin, X.Blase, Y.R. Shen, S.G. Louie, to be published.
13. X.-P. Li and David Vanderbilt, Phys. Rev Lett. **69**, 2543 (1992).
14. L. N. Cooper, Phys. Rev. **104**, 1189 (1956).

15. Ying-Chieh Sun, Huadong Gai, and Gregory Voth, J. Chem. Phys. **100**, 3247 (1994).

16. P. Guyot-Sionnest, P. Dumas, Y.J. Chabal, and G.S. Higashi, Phys. Rev. Lett. **64,** 2156 (1990).

17. P. Dumas, Y.J. Chabal, and G.S. Higashi, Phys. Rev. Lett. **65**, 1124 (1990).

Tables

	Theory	Experiment
Stretching Frequency ω_z	2740 cm^{-1}	2838 ± 2 cm^{-1}
Wagging Frequency ω_x	1189 cm^{-1}	1331 ± 2 cm^{-1}
-2Γ	107 cm^{-1}	
E_b	-110 cm^{-1}	-110 ± 5 cm^{-1}

Table I. Theoretical and experimental stretching (ω_z) and wagging (ω_x) frequencies, together with the overtone frequency -2Γ and the two-phonon bound state energy E_b. (1 meV = 8.04 cm^{-1})

Figures

Figure 1. SFG CH stretch peak signal versus infrared excitation intensity (GW/cm^2).

Figure 2. (a) Energy level diagram illustrating the SFG process for the $\nu_{0\rightarrow 1}$ fundamental transition and the $\nu_{1\rightarrow 2}$ hot band transition. (b) Ideal pump and probe response indicating the ground state and first excited state populations for $\tau(\text{laser pulse}) << \tau(\text{relaxation})$.

Figure 3. (a) SFG spectra of CH stretch vibrations of H/C(111)-(1x1) with (solid squares) and without (open circles) the IR pump excitation of the resonance at 2838 cm^{-1}. (b) Theoretical absorption spectrum for the same vibrational system visually shifted to correspond to (a). The relative peak height is arbitrary. (Supplied by X. Blase)

Figure 4. SFG probe signal for the $\nu_{0\rightarrow 1}$ fundamental transition (upper curve) and the $\nu_{1\rightarrow 2}$ hot band transition (lower curve) as a function of time delay between pump and probe pulses. The solid lines are theoretical fits.

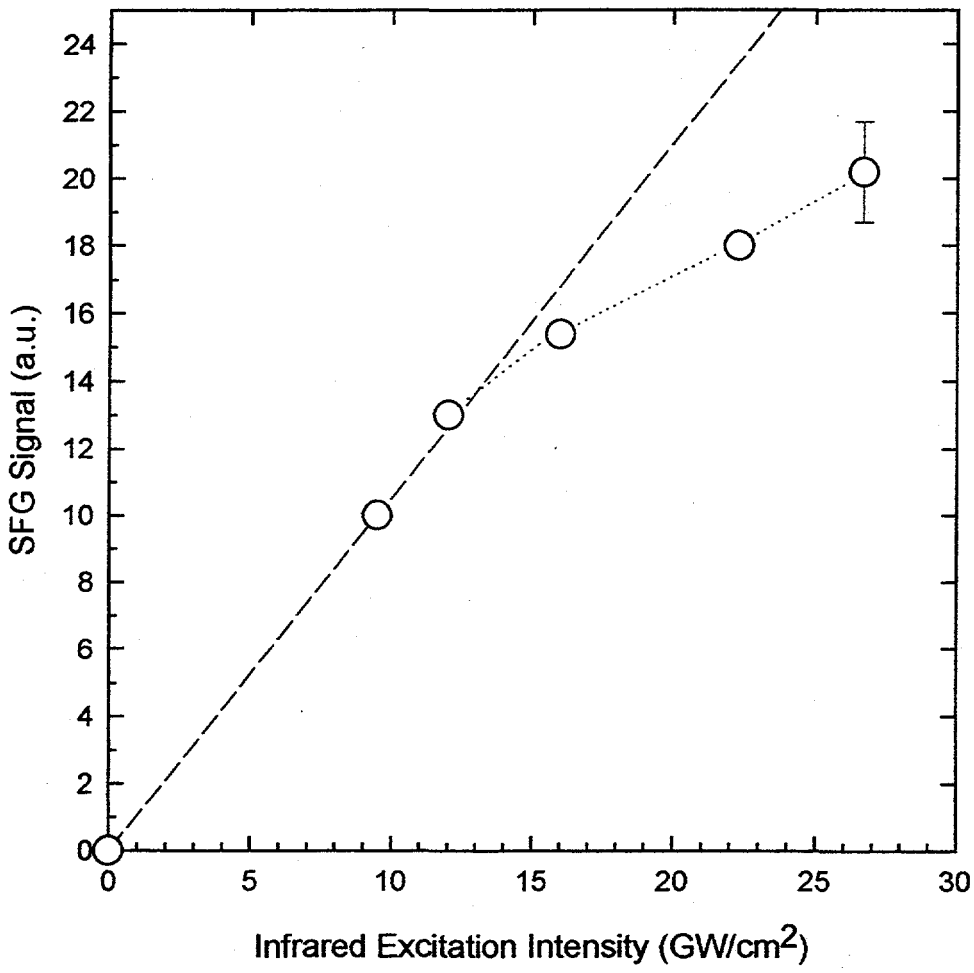
SFG Signal (a.u.)
0
2
4
6
8
10
12
14
16
18
20
22
24
0
5
10
15
20
25
30
Infrared Excitation Intensity (GW/cm2)

Fig. 1

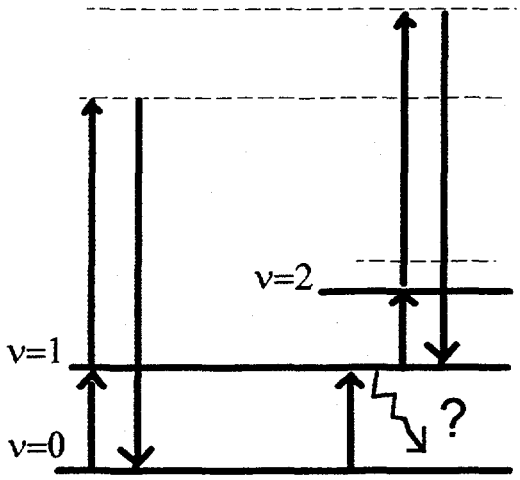
ν=2
ν=1
ν=0
?

(a)

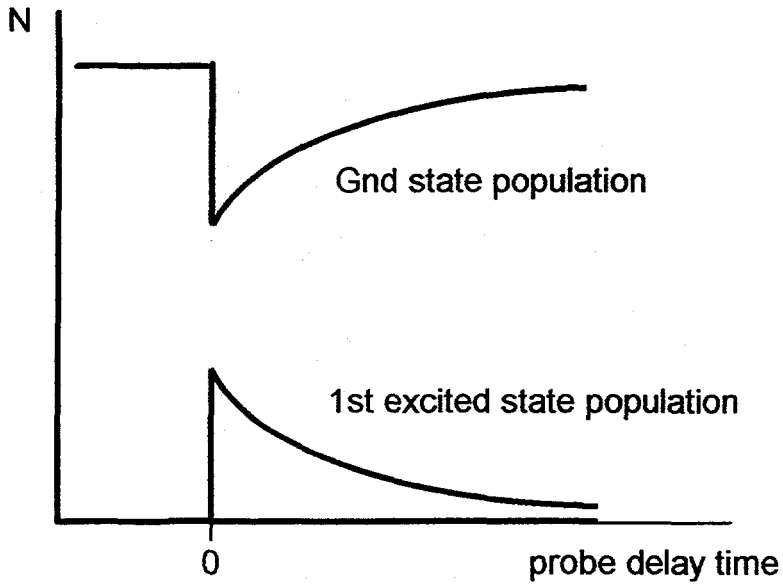
N
Gnd state population
1st excited state population
0
probe delay time

(b)

Fig. 2

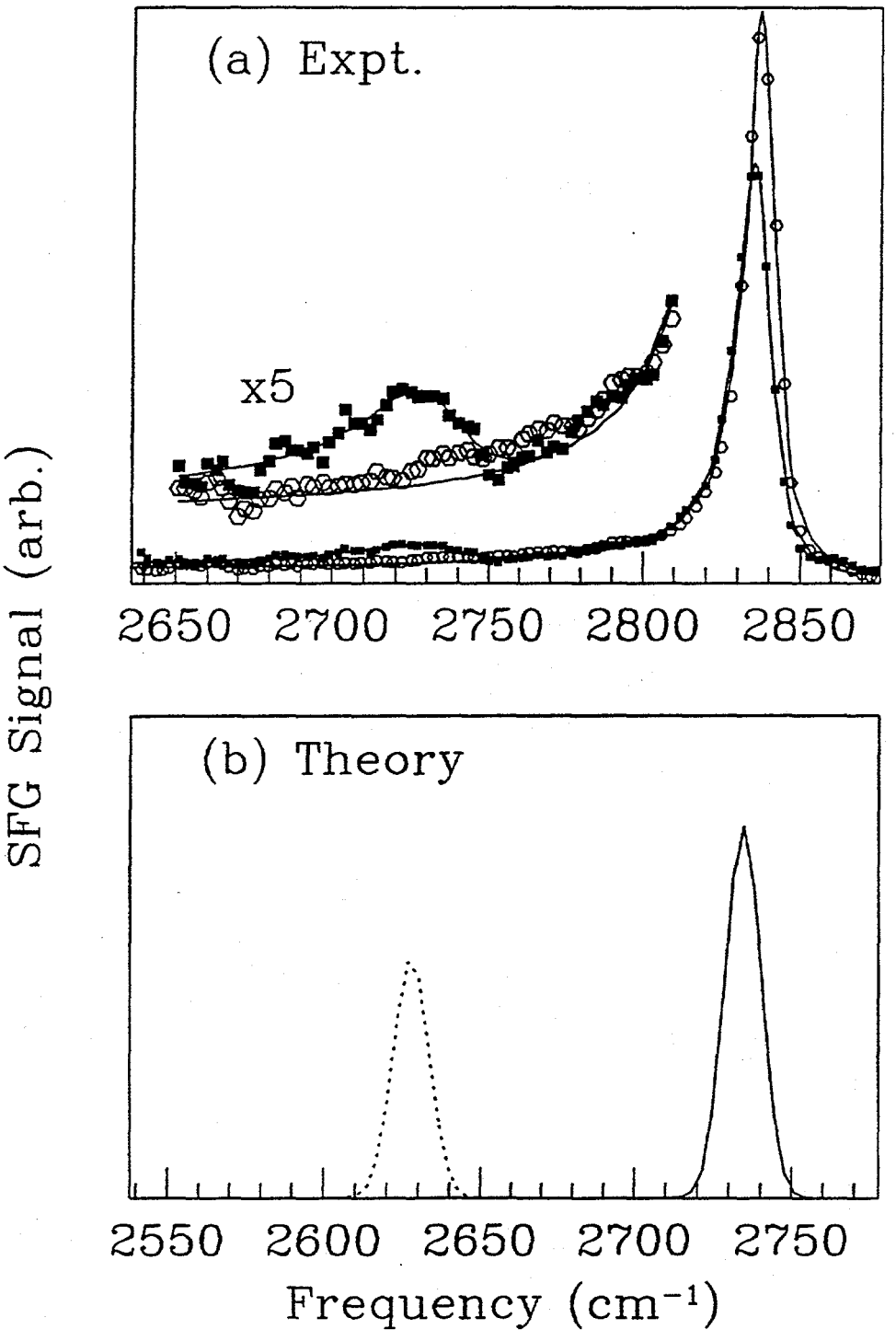
(a) Expt.
x5
2650 2700 2750 2800 2850
(b) Theory
SFG Signal (arb.)
2550 2600 2650 2700 2750
Frequency (cm⁻¹)

Fig. 3

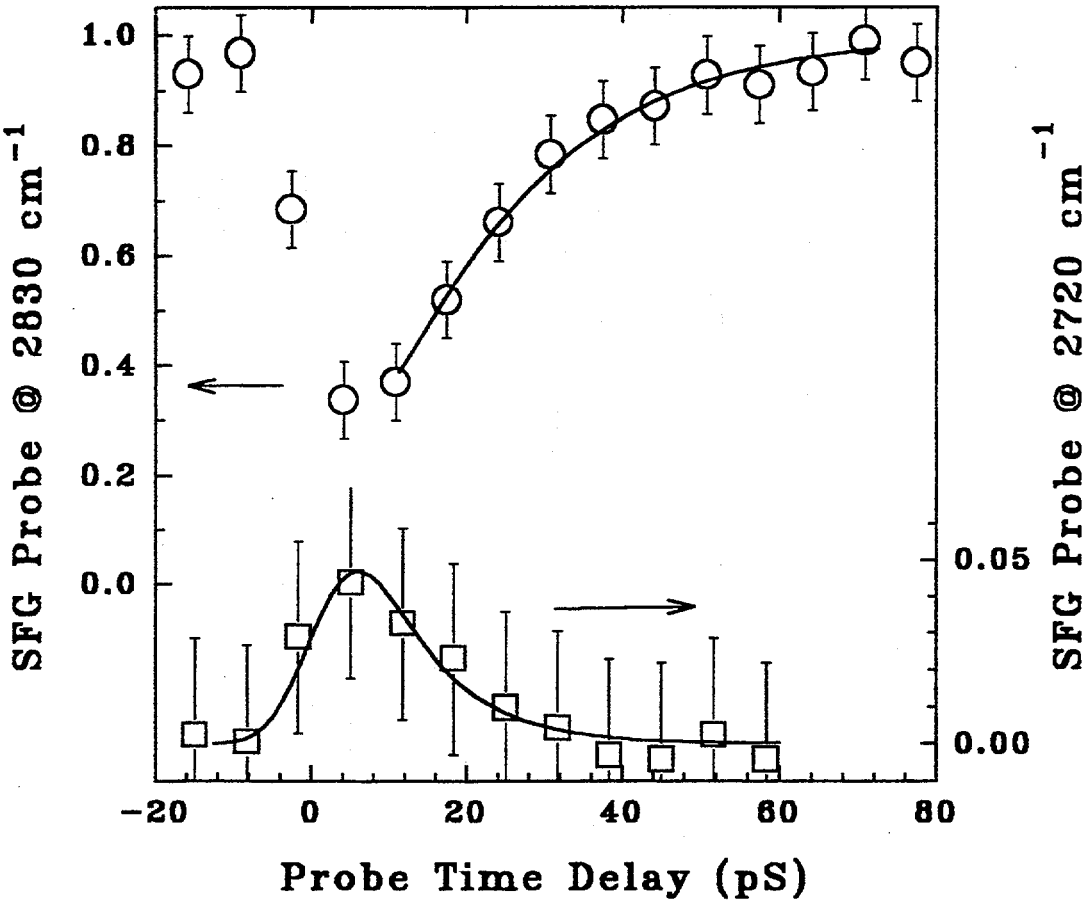
SFG Probe @ 2830 cm^{-1}
SFG Probe @ 2720 cm^{-1}
1.0
0.8
0.6
0.4
0.2
0.0
0.05
0.00
−20
0
20
40
60
80
Probe Time Delay (pS)

Fig. 4

V. Interaction of Methyl Radicals with the Diamond C(111) Surface

A. Introduction

For CVD diamond thin film growth[1] using thermal or plasma activation of gas phase species, the conditions leading to good diamond growth are generally known but the detailed mechanisms are not yet clear. Although a great deal of work has been done in the investigation of the gas composition and gas phase reactions present under CVD conditions, very little is known about the interfacial region where diamond grows. In an attempt to determine the actual gas phase species near the surface, various techniques have been used, such as near-surface resonance-enhanced multiphoton ionization (REMPI)[2] and substrate microprobes[3]. Still, the data is indirect and difficult to intepret since a multitude of surface reactions are possible. Clearly, for a better study of the process, an in-situ probe involving surface vibrational spectroscopy is desirable. Indeed, electron energy loss spectroscopy (EELS), Fourier-transform infrared (FTIR) and more recently, sum-frequency generation (SFG)[4] spectroscopies have all been employed for surface studies. However, the requirement of high sensitivity, high resolution, and surface specificity is satisfied only by infrared-visible SFG vibrational spectroscopy.

Among the spectroscopic methods used to study the hydrogen termination of diamond surfaces, there persists the conclusion that methyl termination exists. Waclawski *et al.*[5] first used High Resolution Electron Energy Loss Spectroscopy (HREELS) to obtain the vibrational spectrum of an as-polished C(111) surface and concluded that the surface was terminated by CH_3. Lee *et al.*[6] studied hydrogen adsorption on C(111). From their HREELS spectra, they identified the presence of surface phonons on the bare reconstructed C(111) surface, and suggested a plethora of different hydrogen terminations for hydrogen adsorption on C(111). Aizawa *et al.*[7] used

HREELS to study the C(111) surface of diamond homoepitaxially grown by chemical vapor deposition (CVD) under microwave plasma-assisted deposition conditions. They interpreted the spectrum as due to the presence of CH_3 termination on the surface.

In chapter III, the interaction of atomic hydrogen with the diamond surface was investigated as hydrogen seemed to play a critical role for diamond growth. The SFG and second harmonic generation (SHG) probes proved to be extremely powerful. So far, hydrogen appears to terminate the as-polished or atomic-hydrogen-dosed C(111) surface; the (1x1) bulk-termination stabilizes the surface at sufficiently low temperatures (<1150 K); upon hydrogen desorption at high temperatures (>1450 K), the surface undergoes a reconstruction to the (2x1) geometry.

However, in diamond growth there must be a carbon source from which the diamond film can grow. In the hot filament method of diamond growth, for example, hydrocarbon gas such as methane is usually heavily diluted with hydrogen (usually <1% CH_4 in H_2) before being passed through a hot filament and exposed to the high temperature substrate (~850°C).[8] The successful use of methane in diamond growth suggests that the methyl radical may play an inportant role. Extension of studies to the methyl radical is now in order. If a methyl species is able to sit at top sites, the characteristic vibrational signature should be distinctly different from that of the monohydride. This would add confidence that the earlier assignment of the monohydride termination was indeed correct.[9] Here, the preliminary interpretation of this work is presented.

B. SFG Vibrational Signature of a Methyl Termination

To observe the methyl species on the diamond surface, infrared-visible sum-frequency generation (SFG) and second harmonic generation (SHG) were employed again.[4]

In Chapter III, the case for the monohydride termination of the diamond C(111) surface was presented. There, the macroscopic surface susceptibility was derived from the molecular hyperpolarizability of the CH bond. In this chapter, the vibrational signature of the methyl group is addressed. Hirose *et al.*[10] has derived in detail the susceptibility for the CH_3 methyl termination and applied this to determine the degree of anisotropy for multilayered Langmuir-Blodgett films. Recently, Wolfrum *et al.*[11] observed the SFG spectrum of hexadecanol on the water surface. In that study, the destructive interference of adjacent vibrational modes to the SFG intensity was seen. Both s- and p- polarized infrared beams were used to observe the methyl (CH_3) group vibrational modes. In their sps and ppp polarization combination spectra, they observed three positive going peaks in the spectrum. These were assigned to the symmetric CH_3 stretch (2875 cm^{-1}), the fermi resonance (FR) (2936 cm^{-1}) of a bending overtone with the symmetric CH_3 stretch, and the asymmetric CH_3 stretch (2958 cm^{-1}). However, in the ssp polarization spectrum, they observed a dip where the asymmetric mode would appear. They explained this as due to the interference of the shoulder of the FR peak with the asymmetric CH_3 stretch which had an opposite phase in the contribution to the overall susceptibility. In their analysis, the formalism of Hirose *et al.* was applied. This allowed for azimuthal isotropy about the methyl group symmetry axis and for azimuthal isotropy of the methyl group about the surface normal with some polar dependence.

Here, a similar situation is possible. As with the monohydride on C(111)-(1x1), azimuthal isotropy is allowed within the surface plane. If the methyl group bonds in a

similar manner as hydrogen on the C(111) surface then the methyl group would be expected to have the freedom to rotate about the CC bond axis although it may have a different polar tilt angle (θ) distribution. This *geometry* is similar to the hexadecanol on water measured by Wolfrum *et al.*, and so here the same formulae applies so one might expect a similar ssp spectrum for the methyl terminated C(111) surface.

In the analysis, the ssp polarization probes the $\chi^{(2)}_{YYZ}$ term if the surface mirror plane lies in the XZ plane of incidence. The symmetric and the asymmetric vibrational modes yield the following terms with opposite sign in amplitude of the susceptibility:[11]

$$\begin{aligned}\chi^{(2)}_{R,YYZ}(\nu_s) &= N_S\alpha^{(2)}_{\zeta\zeta\zeta}\left[(r+1)\langle\cos\theta\rangle+(r-1)\left\langle\cos^3\theta\right\rangle\right]\\ \chi^{(2)}_{R,YYZ}(\nu_d) &= -\frac{N_S}{2}\alpha^{(2)}_{\zeta\eta\eta}\left[\langle\cos\rangle-\left\langle\cos^3\theta\right\rangle\right]\end{aligned} \tag{5.1}$$

where $\hat{\zeta}$ and $\hat{\eta}$ are the directions parallel and perpindicular to the CH_3 symmetry axis, respectively, $r=\alpha^{(2)}_{\zeta\zeta\zeta}/\alpha^{(2)}_{\eta\eta\zeta}$, and θ is the polar tilt angle of the methyl group CC axis with the surface normal.

From Eqn. (5.1) above, the two modes were shown to exhibit opposite phase to one another. In the experiment by Wolfrum *et al.*[11], the Fermi resonance has the same phase as the symmetric stretch which destructively interfered with the asymmetric mode. In their case, the effect was difficult to observe since the overlap of the two modes was slight. However, if the vibrational modes can destructively or constructively interfere with a sufficiently large nonresonant background contribution, the effect can be obvious. The signal would then be close to proportional (linear) to the resonant susceptibility contribution as the signal is proportional to the square of the susceptability:

$$SF \propto \left|\chi^{(2)}\right|^2 \propto \left|\chi^{(2)}_{NR} + \chi^{(2)}_{R,s} + \chi^{(2)}_{R,FR} - \chi^{(2)}_{R,d}\right|^2 \quad (5.2)$$

where $\chi^{(2)}_{NR}$ is the nonresonant background contribution and $\chi^{(2)}_{R}$ is the resonant contribution of the symmetric (s), Fermi resonance (FR) and asymmetric (d) modes with the latter explicitly indicated as negative. On the diamond surface, as shall be seen, a nonresonant background does exist with sufficient strength to exhibit this behavior for the methyl termination occurs.

C. Experiment

The experimental setup was essentially the same as for the hydrogen experiments described in Ch. III. Both SFG and SHG were performed on the diamond surface under a variety of substrate temperatures, dosing conditions, and subsequent processing.

The sample preparation was similar as with the hydrogen experiments of Ch. III. However, there were some differences. For the natural type-IIa diamond, after polishing,[12] the sample produced well-ordered surfaces as determined by the SFG spectra. The primary prerequisite for the following experiments was a high quality, single, narrow linewidth peak at 2838 cm^{-1} of sufficient signal indicating a saturation coverage of the CH monohydride. This was particularly important as the spectra from these experiments were quite weak and there was concern that the surface could support the coordination of other hydrides that could dominate the spectra. The latter concern was valid as the well-ordered hydrogen terminated surface was not able to be recovered after several methyl radical dosing events. This was even after repeated high temperature, atomic hydrogen "cleaning" treatments. At this point, the sample had to be repolished and acid etched.

The (5 mm x 10 mm x 0.001") tungsten filament,[13] 12-16 mm from the diamond surface was used to produce reactive species for the experiments. The production of the methyl radical using CH_4 ($E_{C-H} = 435$ kJ/mole) required a similar hot filament temperature (1800°C) as for the atomic hydrogen case ($E_{H-H} = 436$ kJ/mole). Additionally, two other methyl radical production processes allowed a much lower (~800°C) hot filament temperature. Methyl iodide (CH_3I) ($E_{C-I} = 234$ kJ/mole) can produce a methyl radical but produces as a side product an iodine atom. Di-tert-butyl peroxide ($(CH_3)_3COOC(CH_3)_3$) (DTBP) allows a low temperature breaking of the peroxide bond[14] which produces an unstable intermediate which then forms a stable acetone molecule while ejecting a methyl radical (Fig. 1). In this case, only a single reactive product was generated, namely the methyl radical. To determine the possible effects of the acetone byproduct, dosing with acetone under similar conditions with the hot filament was found not to cause any changes to the covered or bare diamond surface on the time scale of the usual dosing. Further, only if the hot filament temperature was raised ~150°C more did an effect occur, presumably from activation of the acetone molecule. Considering that the concentration of the acetone byproduct from the DTBP pyrolysis would be orders of magnitude smaller, the effects of acetone during the DTBP dosing can be dismissed. Total dosing pressures for the gases were typically $1x10^{-5}$ torr. For the methyl iodide, DTBP, and acetone liquids discussed above, a freeze-pump-thaw method was performed to remove dissolved volatiles. A check was performed to rule out the effects of the ion pressure gauge filament during dosing of the (CH_3I) or DTBP. Even though there was no evidence that the ion gauge posed a problem, the minimum emission setting (lowest filament temperature) was used during the dosing and was turned off during the subsequent processing and measurements as an extra precaution. For "room temperature substrate" dosing, the ~800°C hot filament barely heated the sample, but for the 1800°C hot filament, the substrate temperature rose to a maximum of ~150°C.

The SFG spectra used was the ssp polarization combination (unless noted otherwise), as this gave the strongest signal.[9]

D. Methyl Radical Adsorption and Decomposition

As seen in the hydrogen case (Ch. III), the substrate temperature and atomic hydrogen dosage were the chief parameters for that study. In the methyl radical experiments here, many more parameters may be involved, either intentionally or incidentally. In dosing with methane (methyl iodide), there was the side product of producing the atomic hydrogen (iodine) in addition to the intended methyl radical. For DTBP, the side product of the acetone production seemed "safe" as described above. Other parameters included the substrate temperature, the hot filament temperature, and the starting conditions of the substrate. The latter could be chosen to be totally bare, nearly bare with some hydrogen remaining to preserve the (1x1) surface structure, or near full hydrogen termination.

The majority of the experiments performed started with a "nearly bare" surface with the substrate at room temperature. In experiments performed with LEED and SHG[15], activated methane adsorption onto the bare surface did not match the rapid (2x1) to (1x1) phase transition as for atomic hydrogen dosing. The LEED and TPD results showed that it took up to ~0.3 ML coverage before the (1x1) unreconstructed surface phase appeared. Likewise, the SHG results showed only a slow variation of the signal with the maximum ocurring only after more substantial dosing (Fig. 2). In the SFG spectrum, activated CH_4 or CH_3I dosed onto the bare reconstructed (2x1) surface showed only a very weak signal. This may be due to an overwhelming inhomogeneous broadening, disordering of the surface species, or the blocking of adsorption sites by the

propensity of carbon on the surface. In the earlier paper, it was proposed that the formation of bridge bonded carbon atop the π-bonded chains could hinder the surface phase transition from the reconstructed (2x1) surface to the (1x1) surface.[15]

It is logical that some hydrogen *should* be left on the surface of the diamond to preserve the (1x1) structure before dosing the methyl radical. This surface with ~10 % hydrogen as determined by the SFG CH stretch signal shall be referred to as the "nearly bare" surface for the duration of this chapter. The amount of hydrogen needed to maintain the (1x1) structure is indeed very little and may be much smaller than the 5 % coverage as determined by the LEED experiments. Unfortunately, the dynamic range of the present SFG apparatus does not permit this fine a measurement which would require S/N > 500:1. The nearly bare surface was achieved by thermal desorption of hydrogen starting from a well-ordered hydrogen terminated surface. Calibration by SHG and the presence of CC stretch modes were performed in the past to determine a critical coverage needed to hold the (1x1) surface. The choice of Θ~10 % was set because it was the limit of the SFG signal detection from full coverage so the (1x1) surface was guaranteed with what should be ~90 % vacant sites.

DTBP has been proven as an excellent methyl radical source.[14] Azomethane[16] has been shown to also be a good source since the pyrolysis would generate only methyl radicals and a harmless N_2 molecule. However, the logistics of an on-site synthesis rendered this inaccessible due to its explosive nature. Still, the use of the DTBP seemed satisfactory. The activated DTBP was dosed on the nearly bare surface for a saturation effect with the final spectrum presented in Fig. 3(a).

In this spectrum, a four peak fit to Eqn. (3.2), was performed even though some inhomogeneous broadening may be present. However, the fits seemed satisfactory. At first glance, the small peak at ~2830 cm^{-1} is expected to occur as the small amount of hydrogen on the surface is now made visible by the amplifying term of the main peak at

~2900 cm^{-1}. A one, two, three, or even a four peak fit with only in-phase resonant terms was impossible to fit the data as the dip occurring at ~2965 cm^{-1} was too strongly pronounced. A satisfactory fit only occurred when a peak at (~2965 cm^{-1}) had an opposite phase to the others. Although the spectrum above (ssp polarization combination) showed distinct features, no obvious features were seen in the sps polarization combination spectrum.

On the diamond surface, a methyl radical can also be adsorbed onto the nearly bare diamond surface using activated methyl iodide. The spectra of the diamond dosed with activated CH_3I is similar to the one dosed with DTBP although the peaks are shifted lower in frequency by ~20 cm^{-1} and it seems as though the Fermi resonance has weakened. The latter has probably shifted in accordance with the shifts of the symmetric and bending modes.

In summary, the assignment of the features on the diamond (111) surface dosed by activated DTBP (CH_3I) is as follows. The ~2830 cm^{-1} peak is the usual monohydride seen before and is expected to be present to a small degree. The peak at ~2895 cm^{-1} (~2910 cm^{-1}) peak is assigned to the symmetric CH_3 stretch mode. The fermi resonance of the symmetric stretch with the ovetone of the bending mode is at ~2930 cm^{-1} (~2880 cm^{-1}). The asymmetric stretch mode is represented as a "negative" peak at ~2970 cm^{-1} (~2950 cm^{-1}) which seems to be essential to fit the spectra. When one compares the diamond spectra with the hexadecanol on water spectrum, there are some differences. In that spectrum, the fermi resonance was located close to the asymmetric mode with the result being that there was destructive interference that was barely detectable. In the diamond case, the presence of a strong non-resonant background clearly showed the interference effect.

The consistency of the fit showing the opposite phase of the asymmetric CH_3 mode and the similarity of the diamond spectrum to that of acetone (which has only CH_3

groups) suggests that the assignment is probably correct. However, at this time there is no explanation for the absence of the asymmetric peak in both the diamond and the acetone sps spectra. Geometrical factors at the surface may dictate a suppression of the asymmetric modes in the SFG spectrum. As for the possibility of the occurrence of a methylene CH_2 group, this seems unlikely from geometrical considerations on the (111) surface which represents a very closed surface. At step sites, CH_2 species might exist but the fractional coverage would be small. In addition, from the hydrogen dosed surface, only the narrow linewidth monohydride peak was seen with no evidence of CH_2 or CH_3.

If either of the above methyl terminated diamond surfaces were heated, some surprising results are seen. Figure 4 shows the DTBP dosed, methyl terminated surface undergoing a conversion of the surface species as the substrate temperature was raised. (In all the spectra, the sample was heated to the stated temperature for 10 minutes then cooled for the SFG measurement). The methyl group signatures gradually disappears with the emergence of a 2860-2870 cm^{-1} peak and a stronger ~2830 cm^{-1} CH monohydride peak. With further heating (>700°C), the ~2830 cm^{-1} CH monohydride peak dominates. At even higher temperatures, thermal desorption of hydrogen occurs. Obviously, the final monohydride indicates that hydrogen was supplied by the methyl groups originally terminating the surface.

In a similar manner, Fig. 5 shows the CH_3I dosed, methyl terminated surface showing a similar behaviour and resulting in the same conversion process concluding in the usual CH monohydride.

That such a low temperature (<350°C) could cause the conversion of the methyl group is rather surprising as one would normally think that much higher temperatures are required to break the CH bonds. In the two cases above, a stable methyl species was shown to be able to exist on the diamond C(111) surface only at lower temperatures.

The use of DTBP or CH_3I was necessary for CH_3 adsorption. This may not be possible with the use of methane because the required hot filament temperature might create methyl radicals with high kinetic and high internal energy. These energetic methyl radicals may possess enough energy to open channels for surface reactions to occur before thermalizing with the substrate. In addition, decomposition of activated methane would generate energetic atomic hydrogen that has been shown to be very aggressive at abstraction and adsorption (Ch. III) and Ref. 17. To show that there may be some effects of highly energetic radicals upon the diamond surface, CH_3I dosing with the hot filament heated to the usual ~1800°C was used. Since the CI bond has half of the bond strength of the CH bond in methane, the probability of atomic hydrogen production should be low. With this dosing, the spectrum in Fig. 6(b) shows very little signature of a methyl termination. Instead, it seems as though the surface had been heated to 350°C, although the substrate temperature never rose above ~150°C. The only explanation for this behavior is that the incoming radicals had sufficient energy to initiate the conversion process to yield the features at ~2870 cm^{-1} and ~2830 cm^{-1}.

In the case for activated methane, one would expect a similar behaviour with the added effect that atomic hydrogen is also present. In Fig. 7(b), one sees the initial spectrum showing no methyl termination signatures at all. All that is seen is a strong peak at ~2860 cm^{-1} which then converts to the usual ~2830 cm^{-1} peak upon a higher temperature heating >550°C.

In the spectra above, the ~2860 cm^{-1} feature was not identified. It seems common not only in the experiments involving methyl species conversion, but may be the same species as seen for the adsorption of hydrogen onto the bare, reconstructed (2x1) surface described in Ch. III. Previous polarization measurements of the latter's 2860 cm^{-1} peak suggested it was a monohydride, but with a shifted frequency due to an unrelaxed surface strain or different understructure. Polarization measurements were also

performed on the peak (~2860 cm^{-1}) resulting from the activated methane dosed surface. The sps spectrum showed no discernable features.

E. Coadsorption by Activated Hydrogen or Methane

From the above experiments, it would seem logical to believe that the methyl termination is unlikely under typical CVD conditions, and that the presence of large amounts of atomic hydrogen would cause the surface to be dominated by the monohydride termination. To illustrate this, mixtures of hydrogen gas and methane gas of various ratios were dosed with thermal activation by the 1800°C hot filament. The substrate temperature was held at ~820°C to anneal the damage caused by atomic hydrogen bombardment and is typical of CVD conditions. After ~10 minutes of dosing at 10^{-5} torr, the sample was immediately cooled and the SFG spectra taken. With 100 % hydrogen, the usual, well-ordered CH monohydride peak was present. With 0.5 % CH_4 in H_2 the spectrum showed a similar spectrum as the 100 % H_2 case. For 10 % CH_4 in H_2, only the CH monohydride peak (~2835 cm^{-1}) was seen but the peak intensity was reduced to 50 %. With 50 % CH_4 in H_2, the CH monohydride peak was reduced to 10 %. Finally, with 100 % CH_4, only a very weak signal <5 % was seen.

Another example shows that if the activated methane surface was subsequently dosed with hydrogen (with a ~820°C substrate temperature), the monohydride quickly dominated the surface, seemingly removing the carbon deposited by the methyl radical dosing. This is the fundamental process from which the well-ordered narrow linewidth hydrogen termination is born.

The above illustrates clearly that hydrogen dominates the surface as a monohydride under these conditions, even with significant CH_4 composition of the dosing gas or

contamination of the surface. However, a large fractional amount of hydrocarbon in the gas mixture does seem to reduce the available coverage of hydrogen on the surface. This is probably due to there being insufficient hydrogen to remove the carbon which block adsorption sites.

F. Discussion

From the experiments above, the methyl species was identified on the diamond with the aid of SFG spectra from the liquid acetone surface and the theoretical prediction for the lineshapes of the characteristic vibrational spectra of the methyl termination.

When thermal decomposition of the methyl groups occurs, an intermediate species is formed at 2860-2870 cm^{-1}. The polarization measurements seem to indicate that this is a monohydride. The nature of this species is still a mystery. Recently, scanning tunnelling microscopy of vapour-grown polycrystalline films has been observed by Busmann *et al.*[18]. In that study, they observed bulk-like (111) surfaces but also features described as a $\sqrt{3} \times \sqrt{3}$ R30° superstructure. They attributed this to be the formation of carbon trimers on the (111) surface which were shown to be stable structures according to molecular dynamics calculations. It was shown that these trimers could support a monohydride termination where each carbon would carry a single monohydride. If this indeed is the case, the 2860-2870 cm^{-1} peak might be attributed to this. However, it should be noted that the conditions of the surface preparation were vastly different for the two cases.

Usual CVD conditions incorporating very high substrate temperatures and high temperature gas phase reactive species would seem to indicate that it is impossible for the methyl species to be present on the growing surface. This contrasts some present

viewpoints on the mechanisms leading to diamond growth as many think that the methyl species is an important precursor for diamond growth. This does seem to agree with the experimental fact that almost *any* carbon source (such as fullerenes, amorphous carbon, or hydrocarbons) can be used in CVD diamond growth as long as there is an adequate supply of atomic hydrogen. This suggests the carbon is plainly deposited on the surface where it bonds indiscriminately to incorporate into the substrate. If the bonding arrangement yields an sp^3 bonding which is commensurate with the underlying crystal structure the carbon atom remains and is not likely to be removed by the atomic hydrogen. However, if the bonding arrangement is graphitic, then this would be preferentially removed by atomic hydrogen. Since this process would be dynamic with simultaneous removal and deposition of surface species, one would expect that diamond growth would be slow and that appreciable growth rates would not occur until higher pressures were used. These are well-known facts of CVD diamond growth.

In the process of the decomposition of the methyl species on the surface, it is not known whether the carbon associated with the original methyl group has remained on the surface or has desorbed. It is most likely that the former occurred. This was backed by the lack of change in the CH monohydride signal after another methyl radical dosing (and thermal heating to >750°C) was performed. It seemed as though the carbon was still situated on the diamond blocking adsorption sites. A suggestion is to use radioactive tagging of the methyl species. If the conversion of the "tagged" methyl species results in the incorporation of the carbon in the bulk, they would be detected.

The above observations agree with the coadsorption experiments showing that there must be much more hydrogen; otherwise full hydrogen surface coverage and graphitic carbon removal does not occur. This is probably the reason why high quality diamond films require a great deal of hydrogen in the feed gas.

G. Conclusion

The methyl termination was shown to exist on the diamond surface for low temperatures only. At temperatures >350°C, the methyl group undergoes conversion to eventually give the usual CH monohydride (~2835 cm^{-1}) with an intermediate 2860-2870 cm^{-1} strained monohydride phase.

References

1. R. C. DeVries, Ann. Rev. Mater. Sci. **17**, 161 (1987).

   K. E. Spear, J. Am. Ceram. Soc. **72**, 171 (1989).

   J. C. Angus and C. C. Hayman, Sci. **241**, 913 (1988).

2. F.G. Celii and J.E. Butler, J. Appl. Phys., **71**, 2877 (1992).

   F.G. Celii and J.E. Butler, Appl. Phys. Lett., **54**, 1031 (1989).

   E.J. Corat and D.G. Goodwin, *Novel Forms of Carbon*, Mater. Res. Soc., 377 (1992).

3. S.J. Harris and A.M. Weiner, J. Appl. Phys., **67**, 6520 (1990).

4. Y.R. Shen, Nature (London) **337**, 519 (1989) and references therein.

   Y.R. Shen, Surface Science, **299/300**, 551 (1994) and references therein.

5. B. J. Waclawski, D. T. Pierce, N. Swanson, and R. J. Celotta, J. Vacuum Sci. Technol. **21**, 368 (1982).

6. S.-Tong Lee and G. Apai, Phys. Rev. B. **48**, 2684 (1993).

7. Takashi Aizawa, Toshihiro Ando, Mutsukazu Kamo, and Yoichiro Sato, Phys. Rev. B **48**, 18348 (1993).

2. Y. Cong, R. W. Collins, G. F. Epps, and H. Windischmann, Appl. Phys. Lett. **58**, 819 (1991).

9. R.P. Chin, J.Y. Huang, Y.R. Shen, T.J. Chuang, H. Seki and M. Buck, Phys. Rev. B **45**, 1552 (1992).

10. C. Hirose, N. Akamatsu, and K. Domen, J. Chem. Phys., **96**, 997 (1992).

    C. Hirose, N. Akamatsu, and K. Domen, Appl. Spectr., **46**, 1051 (1992).

    C. Hirose, H. Yamamoto, N. Akamatsu, and K. Domen, J. Phys. Chem., **97**, 10064 (1993).

    N. Akamatsu, K. Domen, and C. Hirose, J. Phys. Chem., **97**, 10070 (1993).

11. K. Wolfrum, A. Labereau, Chem. Phys. Lett., **228**, 83 (1994).

12. B. B. Pate, Surf. Sci. **165**, 83 (1986).

13. J. N. Smith, Jr. and W. L. Fite, J. Chem. Phys. **37**, 898 (1962).

14. S.W. North, D.A. Blank, P.M. Chu, Y.T. Lee, J. Chem. Phys., **108**, 792 (1995).

    T.G. DiGiuseppe, J.W. Hudgens, and M.C. lin, J. Phys. Chem., **86**, 36 (1982).

    G.N. Robinson, G.M. Nathanson, R.E. Continetti, and Y.T. Lee, J. Chem. Phys., **89**, 6744 (1988).

    C. Yamada, E. Hirota, and K. Kawaguchi, J. Chem. Phys., **75**, 5256 (1981).

15. Y. Mitsuda, T. Yamada, T.J. Chuang, H. Seki, R.P. Chin, J.Y. Huang, Y.R. Shen, Surf. Sci. Lett., **257**, L633 (1991).

16. R. Renaud and L.C. Leitch, Can. J. Chem., **32**, 545 (1954).

17. Brian D. Thoms, John N. Russell, Jr., Pehr E. Pehrsson, and James E. Butler, J. Chem. Phys., **100**, 8425 (1994).

18. H.-G. Busmann, S. Lauer, I.V. Hertel, W. Zimmermann-Edling, H.-J. Güntherodt, Th. Fauenheim, P. Blaudeck and D. Porezag, Surf. Sci., **295**, 340 (1993).

    T. Frauenheim, U. Stephan, P. Blaudeck, D. Porezag, and others, Diamond and Related Materials, **3**, 966 (1994).

Figures

Fig. 1. Pyrolysis of the di-tert-butyl peroxide (DTBP) molecule to form two methyl radicals and two acetone molecules.

Fig. 2. SHG signal (p-in p-out) versus activated methane dosing time (min.) on the bare, reconstructed (2x1) surface.

Fig. 3. (a) Saturation spectrum of the DTBP dosed (~800°C hot filament) nearly bare, room temperature diamond C(111) surface for ssp (open circles) and sps (open triangles) polarization combination. The solid line represents a four peak fit with a nonresonant background according to Eqn. (3.2) which includes a resonant term of the opposite phase. (b) Saturation spectrum of the CH_3I dosed (~800°C hot filament) nearly bare, room temperature diamond C(111) surface. The solid line represents a five peak fit with a nonresonant background according to Eqn. (3.2) which includes a resonant term of the opposite phase. The dotted lines in both graphs represent a three peak fit with a nonresonant background but *without* a resonant susceptibility of opposite phase.

Fig. 4. The effects of thermal treaments after the dosing of the pyrolysis of DTBP (~800°C hot filament) onto the nearly bare, room temperature diamond C(111) surface. (a) the nearly bare surface, (b) the DTBP dosed surface, (c) heated to 350°C, (d) heated to 500°C, (e) heated to 620°C, (f) heated to 740°C, and (g) heated to 800°C. Spectra (c)-(g) have been incrementally shifted upwards by 5 units for clarity.

Fig. 5. The effects of thermal treaments after the dosing of activated CH_3I (~800°C hot filament) onto the nearly bare, room temperature diamond C(111) surface. (a) the nearly bare surface, (b) the activated CH_3I dosed surface, (c) heated to 350°C, (d) heated to 450°C, (e) heated to 550°C, (f) heated to 660°C, (g) heated to 740°C, and (h) heated to 800°C. Spectra (c)-(h) have been incrementally shifted upwards by 5 units for clarity.

Fig. 6. The effects of thermal treaments after the dosing of activated CH_3I (~1800°C hot filament) onto the nearly bare, room temperature diamond C(111) surface. (a) the nearly bare surface, (b) the activated CH_3I dosed surface, (c) heated to 350°C, (d) heated to 450°C, (e) heated to 550°C, and (f) heated to 660°C. Spectra (b)-(f) have been incrementally shifted upwards by 5 units.

Fig. 7. The effects of thermal treaments after the dosing of activated CH_4 (~1800°C hot filament) onto the nearly bare, room temperature diamond C(111) surface. (a) the nearly bare surface, (b) the activated CH_4 dosed surface, (c) heated to 350°C, (d) heated to 450°C, (e) heated to 555°C, (f) heated to 660°C, and (g) heated to 775°C. Spectra (b)-(g) have been incrementally shifted upwards by 5 units for clarity.

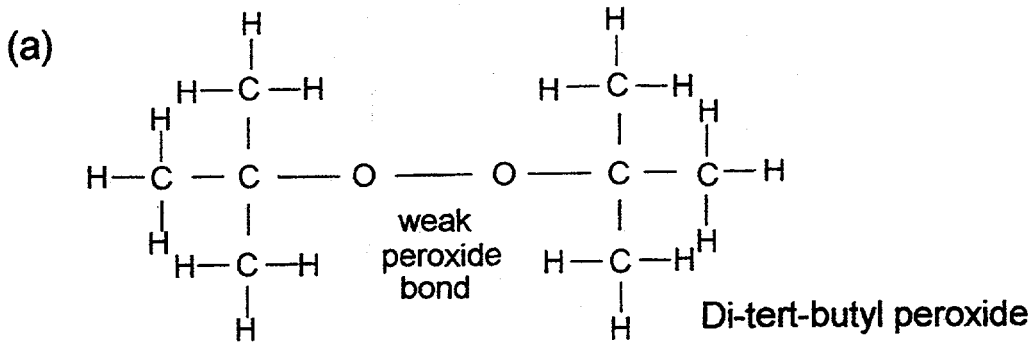
(a)
weak
peroxide
bond
Di-tert-butyl peroxide

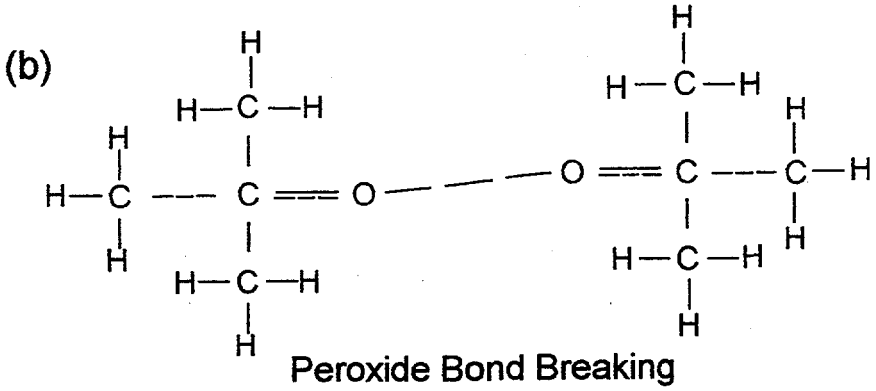
(b)
Peroxide Bond Breaking

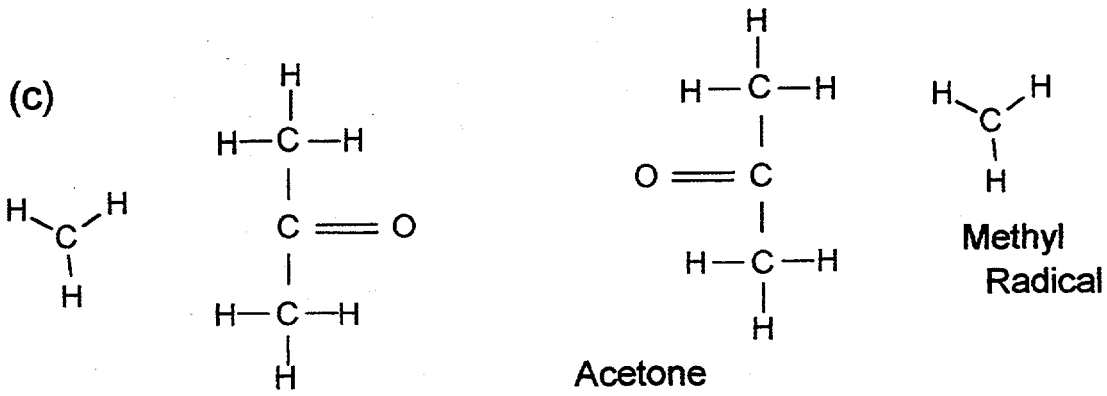
(c)
Acetone
Methyl
Radical

Fig. 1

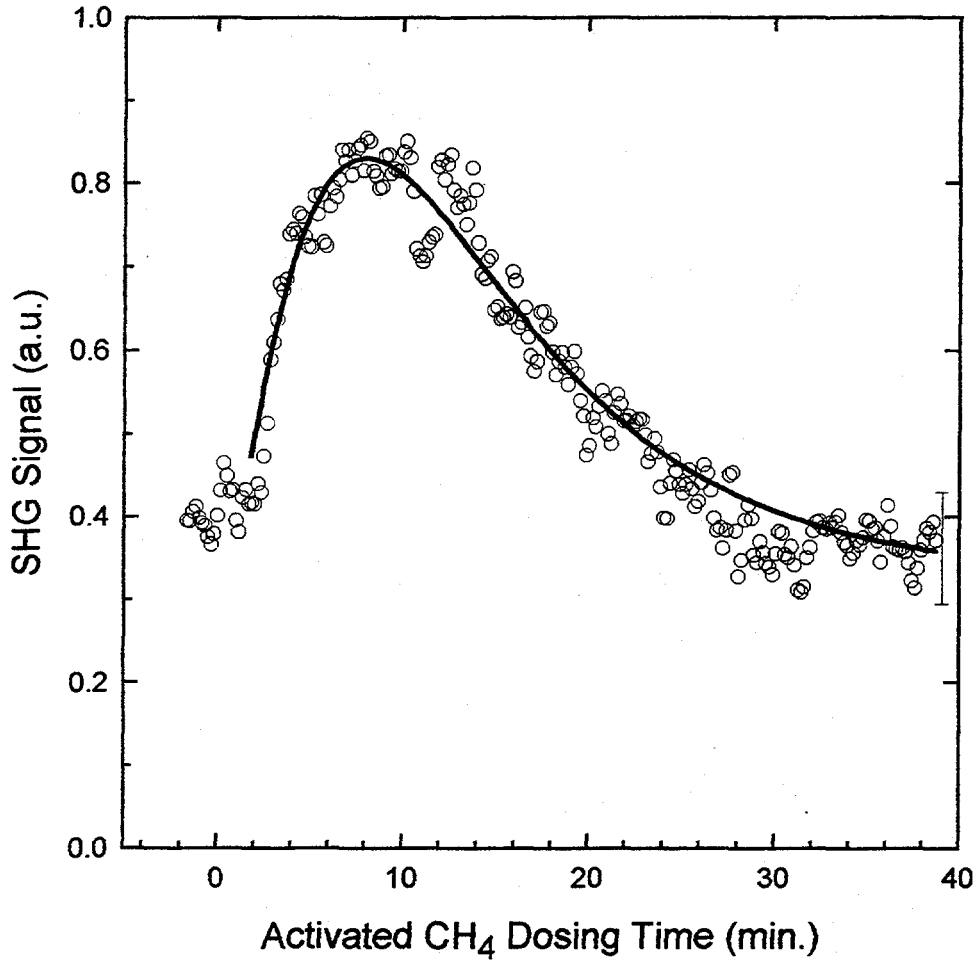
1.0
0.8
0.6
0.4
0.2
0.0
SHG Signal (a.u.)
0
10
20
30
40
Activated CH_4 Dosing Time (min.)

Fig. 2

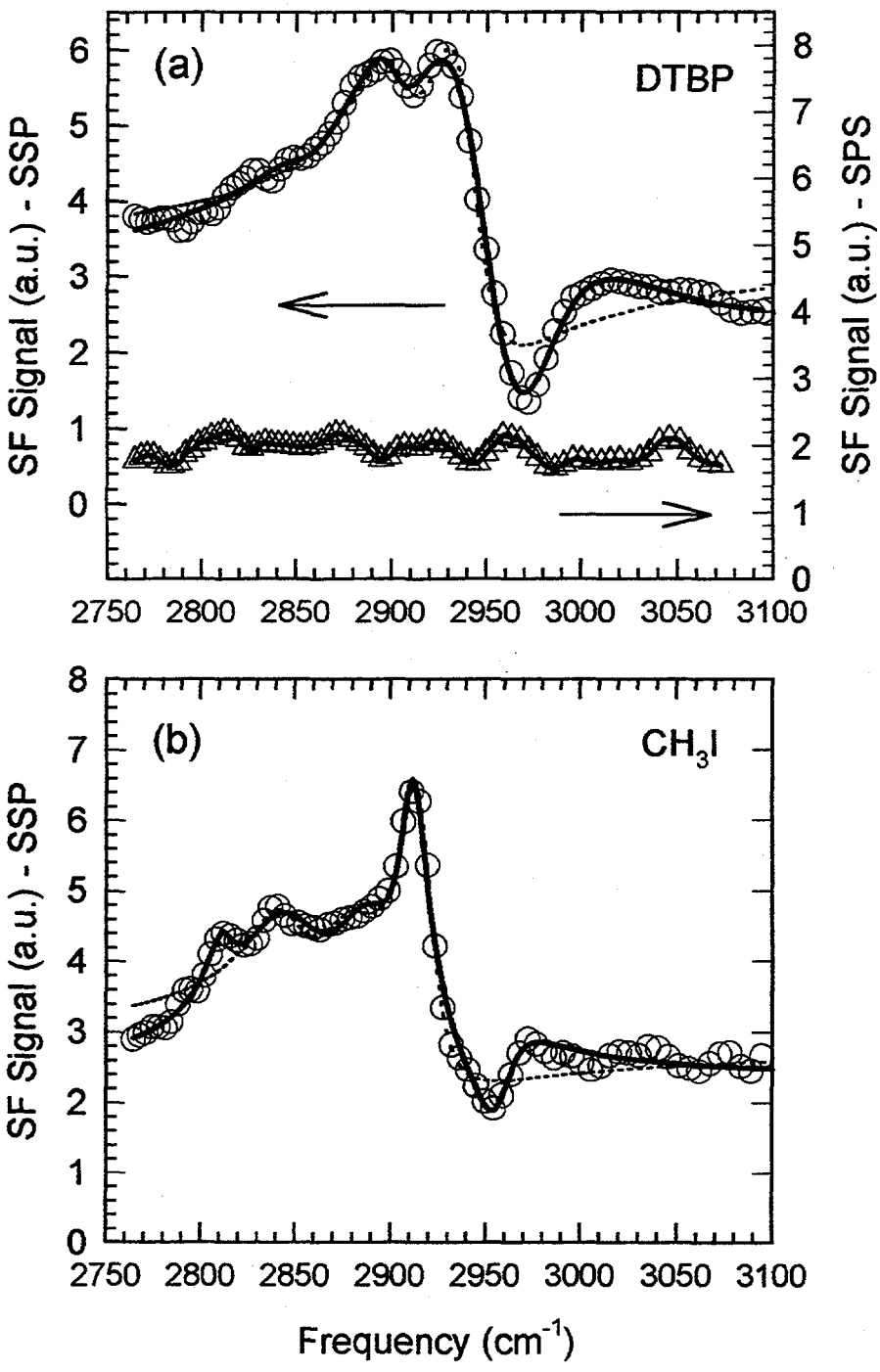

Fig. 3

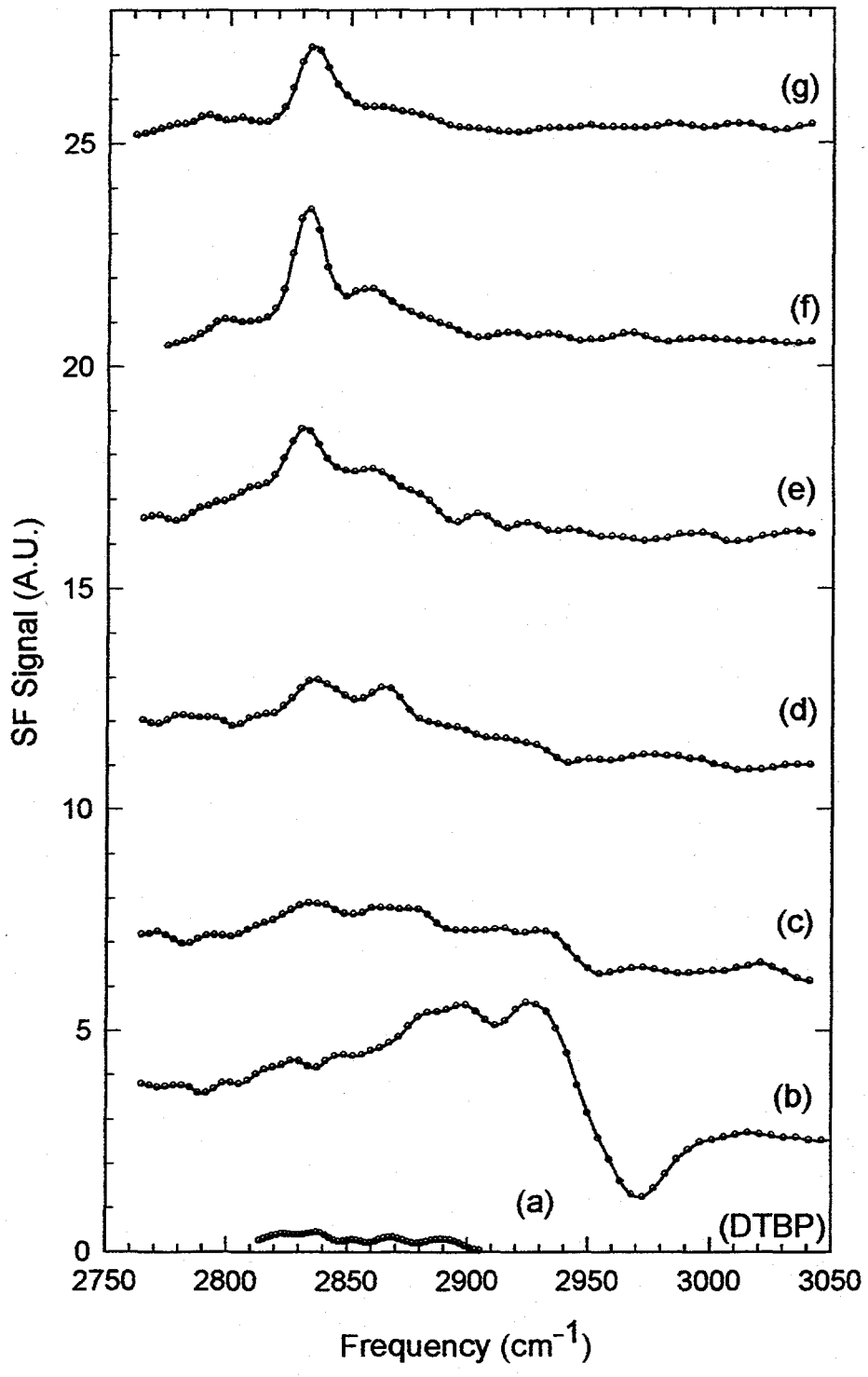
(g)
(f)
(e)
(d)
(c)
(b)
(a)
(DTBP)
SF Signal (A.U.)
0
5
10
15
20
25
2750
2800
2850
2900
2950
3000
3050
Frequency (cm^{-1})

Fig. 4

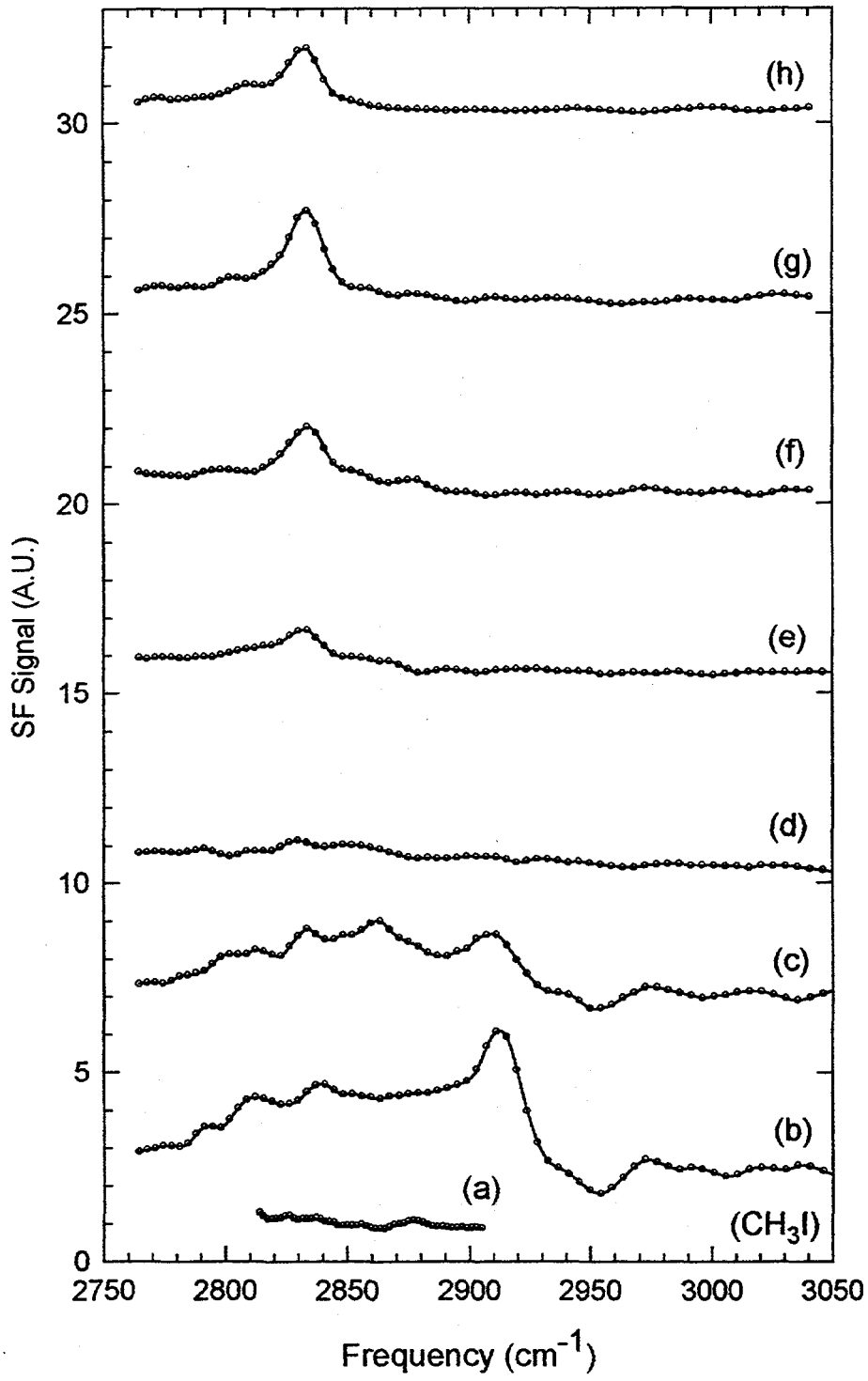
(h)
(g)
(f)
(e)
(d)
(c)
(b)
(a)
(CH_3I)
SF Signal (A.U.)
0
5
10
15
20
25
30
2750
2800
2850
2900
2950
3000
3050
Frequency (cm^{-1})

Fig. 5

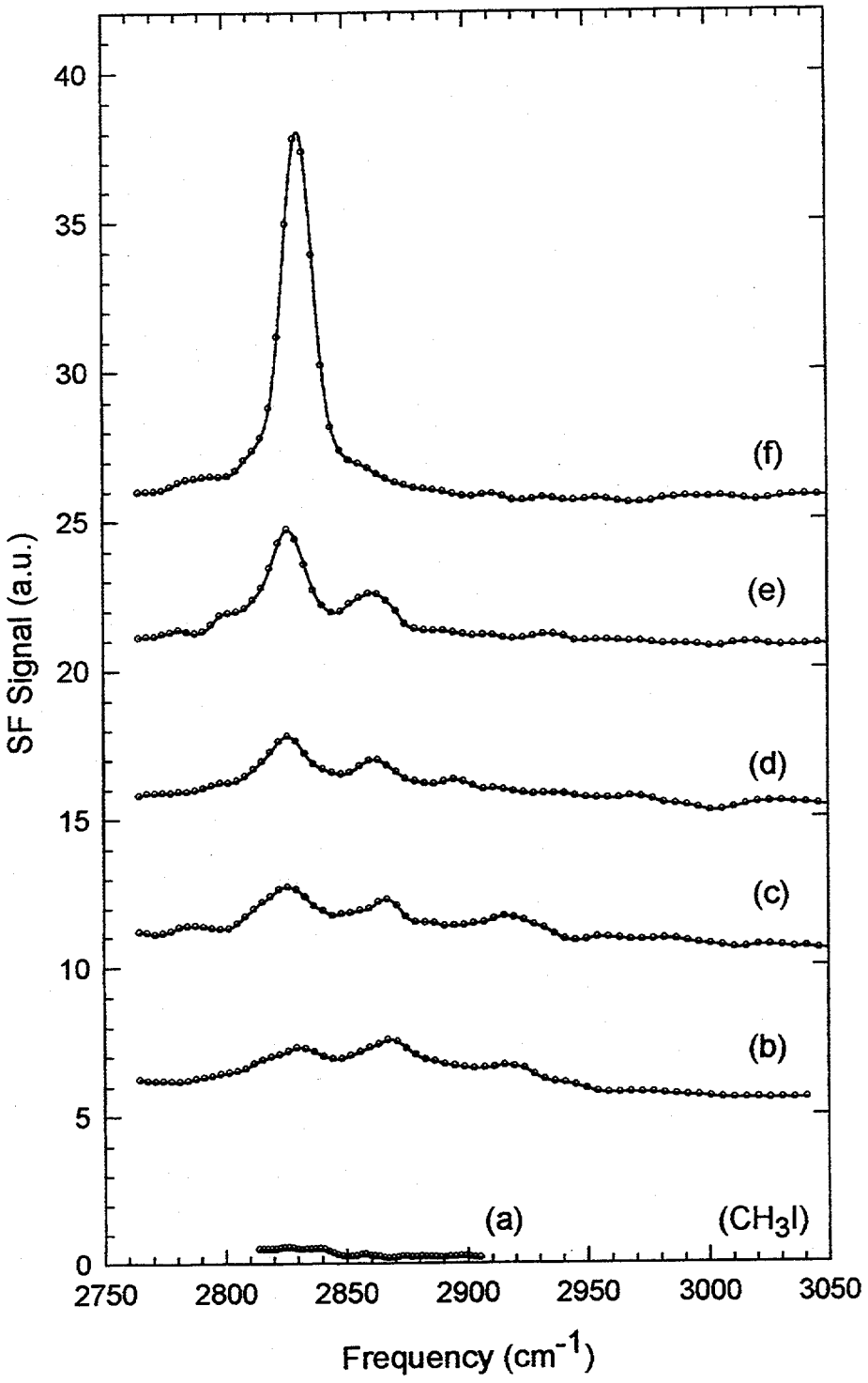
SF Signal (a.u.)
Frequency (cm^{-1})
(f)
(e)
(d)
(c)
(b)
(a)
(CH$_3$I)
0
5
10
15
20
25
30
35
40
2750
2800
2850
2900
2950
3000
3050

Fig. 6

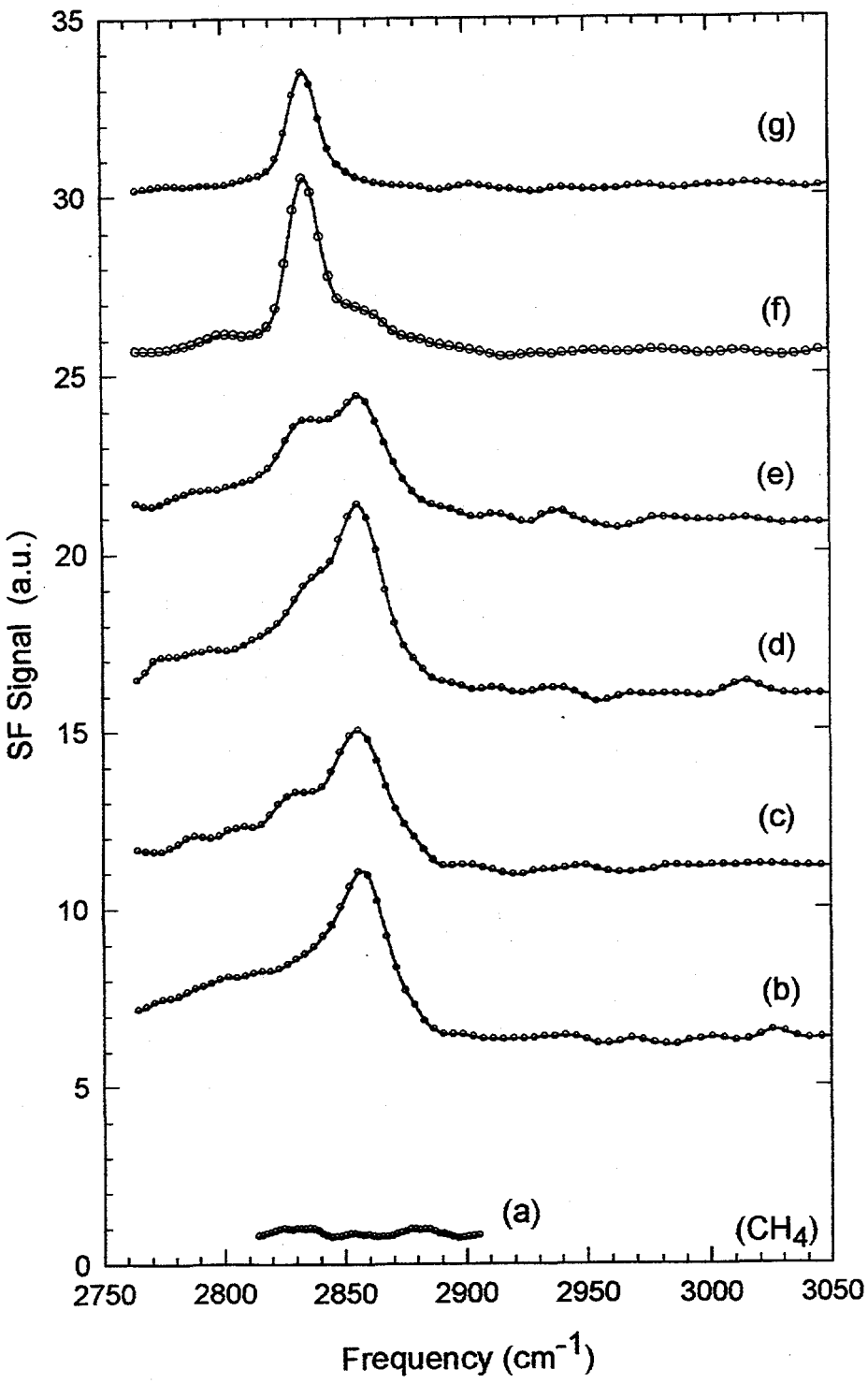
35
30
25
20
15
10
5
0
SF Signal (a.u.)
(g)
(f)
(e)
(d)
(c)
(b)
(a)
(CH4)
2750
2800
2850
2900
2950
3000
3050
Frequency (cm-1)

Fig. 7

VI. Interaction of Hydrogen with the Diamond C(100) Surface

A. Introduction

In the previous chapters, the (111) surface was studied. However, two other principle growth planes of importance are the (100) and the (110) surfaces. In this chapter, the diamond (100) surface is considered.

Like the (111) surface, the nature of the hyride termination of the C(100) surface is somewhat controversial. For a fully hydrogenated surface, the surface is described as a dihydride where there are two hydrogen atoms bonded to the surface carbon denoted by 2H:C(100)-(1x1), shown in Fig. 1(a). However, some theoretical studies[1] suggest that this geometry is unlikely due to the large steric hinderance of neighboring hydrogen atoms. As a result, the surface undergoes a reconstruction where carbon dimers are formed where only one hydrogen atom bonds with the surface carbon atom, denoted by H:C(100)-(2x1), shown in Fig. 1(b). If all hydrogen is removed from the (100) surface, by thermal desorption for example, the reconstructed surface forms π-bonded carbon dimers instead, denoted by C(100)-(2x1), shown in Fig. 1(c).

Recently, Aizawa *et al.*[2] studied the surfaces of microwave assisted CVD diamond for the (100) surface. They observed only one mode at ~2930 cm^{-1} by high resolution electron energy loss spectroscopy (HREELS) for the H:C(100)-(2x1) reconstructed surface as determined by low energy election diffraction (LEED). In a separate experiment, Thoms *et al.*[3] also used HREELS to study the (100) surface exposed to atomic hydrogen and observed a single peak at ~2915 cm^{-1}.

With SFG vibrational spectroscopy, one should be able to resolve the nature of the hydride termination with the increased resolution and sensitivity.

B. Experiment

The experimental setup was similar to that of the diamond (111) studies described in Ch. III with similar beam parameters for the SFG measurement. However, the diamond now used was oriented in the (100) direction within 3°. The sample was polished,[4] acid etched, and installed into the ultrahigh vacuum chamber in a similar manner as the (111) diamond sample.

C. Results

The hydrogen terminated diamond (100) surface was obtained by a similar high substrate temperature hydrogen dosing as for the (111) surface. However, a well-ordered hydrogen terminated surface was more difficult to achieve. It seemed that the degree of polishing played a more important role as a longer, more aggressive polishing improved the spectra. For the hydrogen terminated surface, Fig. 2 shows the SFG spectra for both ssp (SF ouput, visible input, infrared input) and sps polarization combination in which each spectrum was fitted with two resonant terms and a nonresonant background (solid lines). The ssp spectrum (upper curve) was dominated by a strong peak at ~2940 cm^{-1} with a weaker peak at ~2870 cm^{-1}. The weaker peak represented a resonant contribution indicative of a surface coverage that was ~17 % of the stronger peak. Correspondingly in the sps spectrum (lower curve), the strong peak was at ~2940 cm^{-1} with the weaker one at ~2870 cm^{-1}. Here, the weaker peak represented a resonant contribution indicative of a surface coverage that was ~19 % of the stronger peak.

If one looks at the ratio of the peak strengths for the large peak and the weaker peak

for the two infrared polarizations, one might get a clue as to the nature of the surface species. For the strong feature, the ratio of the ssp versus sps signal is ~3.6; whereas, for the weak peak the ratio is ~3.3. With an experimental error of ~15 %, these ratios are identical.

The two peaks in the ssp and sps spectra must represent the same two surface species at ~2940 cm^{-1} and ~2870 cm^{-1}. This suggests that these peaks represent two monohydrides which have a similar orientational distribution, and that the only difference between them is their surface density and a slightly different bonding arrangement giving slightly different frequencies. Perhaps they represent species located on terraces and near step sites. From the ratio of the ssp and sps peaks, we can use the same treatment as that used in Ch. III for the CH monohydride. In this case, the azimuthal plane is treated as isotropic since the surface now has four-fold symmetry.

$$\begin{aligned} \chi^{(2)}_{R,YYZ} &= N_S \alpha^{(2)}_{\zeta\zeta\zeta}\left[\tfrac{1}{2}(1-r)\left\langle \sin^2\theta\cos\theta\right\rangle + r\left\langle\cos\theta\right\rangle\right] \\ \chi^{(2)}_{R,YZY} &= \chi^{(2)}_{R,ZYY} = \frac{N_S}{2}\alpha^{(2)}_{\zeta\zeta\zeta}(1-r)\left\langle \sin^2\theta\cos\theta\right\rangle \end{aligned} \tag{6.1}$$

where θ is the orientation angle of the CH relative to the surface normal; $r = \alpha^{(2)}_{\eta\eta\zeta}/\alpha^{(2)}_{\zeta\zeta\zeta}$ (≈ 0.14) is the ratio of transverse and longitudinal Raman polarizability associated with a CH bond[5]; η and ζ are the axes perpendicular and parallel to the bond axis, respectively; and $\langle\ \rangle$ denotes the orientational average of the CH bonds on the surface. From Eqn. (6.1), it is now possible to determine the polar bond angle (assuming an orientational distribution) from $\chi^{(2)}_{R,YYZ}$ and $\chi^{(2)}_{R,YZY}$.

Since it is expected that the CH bond distribution has a maximum at some angle away from the normal, one may assume that the orientational distribution is a delta

function at a polar angle, θ. From Eqn. (6.1), the polar angle derived is $\theta \approx 20°$. This is consistent with the fact that if the (100) surface supported only a monohydride H:C(100)-(2x1) surface, the resulting reconstruction would orient the CH bonds more normal to the surface than for the dihydride 2H:C(100)-(1x1) surface in which the CH bond angle would be closer to $\theta \approx 55°$. This is because the carbon would be fully sp^3 hybridized which would give a HCH bond angle of ~110°.

D. Discussion

Here, the SFG spectra for the diamond (100) surface appears to correspond well with the results of HREELS by Aizawa *et al.* (~2930 cm^{-1}) and Thoms *et al.* (~2915 cm^{-1}). The ~2940 cm^{-1} and ~2870 cm^{-1} peaks in the spectra had the same polarization dependence ($\theta \approx 20°$) with fractional coverages of 85 % and 15 %, respectively; they were assigned as monohydrides. These experimental results agree with the majority of theoretical studies suggesting that the steric interactions for the dihydride termination are energetically unfavorable and that the monohydride is the more likely surface termination.

We have not suceeded to observe the bending modes of these monohydrides. This would be helpful in confirming that the hydrides on the surface were monohydrides and that the assignment above was correct.

References

1. J. Furthmuller, J. Hafner, G. Kresse, Europhys. Lett., **65**, 2957 (1994).

   T.I. Hukka, T.A. Pakkanen, M.P. D'Evelyn, J. Phys. Chem., **98**, 12420 (1994).

   A.V. Hamza, G.D. Kubiak, and R.H. Stulen, Surf. Sci., **237**, 35 (1990).

   B.N. Davidson and W.E. Pickett, Phys. Rev. B, **49**, 11253 (1994).

   T. Frauenheim, U. Stephan, P. Blaudeck, D. Porezag, and others, Phys. Rev. B, **48**, 189 (1993).

   S.H. Yang, D.A. Drabold, J.B. Adams, Phys. Rev. B, **48**, 5261 (1993).

2. T. Aizawa, T. Ando, M. Kamo, Y. Sato, Phys. Rev. B, **48**, 18348 (1993).

   T. Ando, T. Aizawa, K. Yamamoto, Y. Sato, and others, Diamond and Related Materials, **3**, 975 (1994).

3. B.D. Thoms and J.E. Butler, Phys. Rev. B, **50**, 17450 (1994).

   B.D. Thoms, M.S. Owens, J.E. Butler, C. Spiro, Appl. Phys. Lett., **65**, 2957 (1994).

4. B. B. Pate, Surf. Sci. **165**, 83 (1986).

5. K. M. Gough, J. Chem. Phys. **91**, 2424 (1989).

Figures

Fig. 1. The hydrogen terminated diamond C(100) surface. (a) fully saturated dihydride surface 2H:C(100)-(1x1). (b) reconstructed monohydride surface H:C(100)-(2x1) (c) Bare reconstructed (π-bonded) surface C(100)-(2x1).

Fig. 2. SFG spectrum for the ssp (s - SF output, s - visible input, p - infrared input) and sps polarization combinations. The solid line is a two resonant term fit with a nonresonant background.

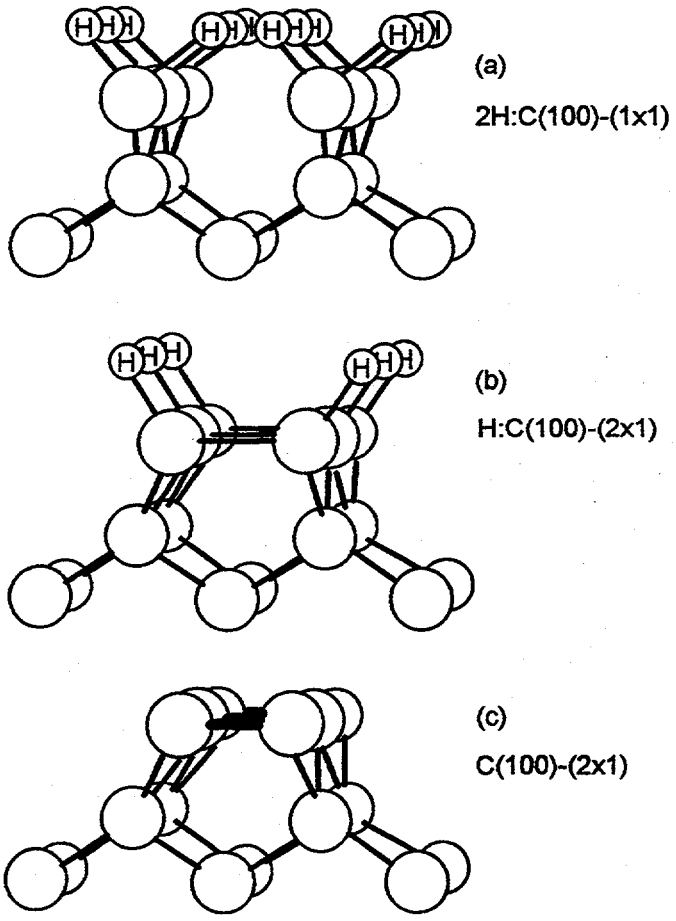

Fig. 1

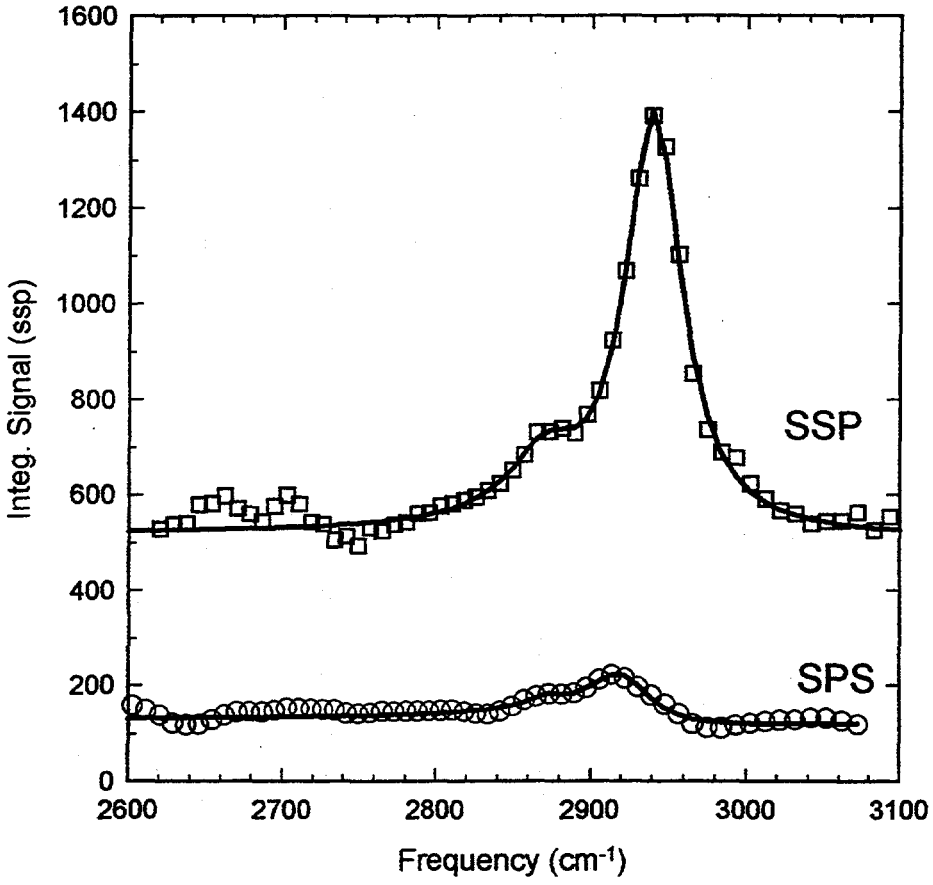
1600
1400
1200
1000
800
600
400
200
0
Integ. Signal (ssp)
SSP
SPS
2600
2700
2800
2900
3000
3100
Frequency (cm-1)

Fig. 2

VII. Conclusion and Extensions

The study of the diamond surface by second harmonic generation and sum frequency generation has been very successful. Many physical and chemical properties of the hydrogen and carbon bonding on the diamond surface were observed. The foundation for the experiments lay in the SFG vibrational spectroscopy. With extensions of this to include time resolved measurements and thermal desorption spectroscopy, some difficult parameters were determined. The greatest advantage of the vibrational spectroscopy was to be able to observe surface chemical bonding occurring in-situ giving insight to the processes of diamond growth.

On the diamond (111) surface, it was observed that the monohydride species terminated the surface with hydrogen at top-sites. On the fully hydrogenated surface, a CH stretch mode (2838 cm^{-1}) and a CH bend mode (1331 cm^{-1}) were observed in the vibrational spectrum. The nature of the adsorption, abstraction, and desorption of hydrogen were also observed. Upon adsorption of atomic hydrogen onto the bare (111) surface, a metastable monohydride 2860 cm^{-1} was observed in the SFG spectrum which converted to the usual 2838 cm^{-1} peak upon annealing or more hydrogen dosing. The ratio of the rate of abstraction to the rate of adsorption was appreciable ($K_{abs}/K_{ads} = 20\ \%$) for atomic hydrogen dosing. For thermal desorption, kinetic parameters were determined showing near first-order kinetics (n=1.3) with a pre-exponential factor of $10^{15}\ s^{-1}$ and desorption energy of 4.0 eV. For the fully H-terminated (111) surface, a large (110 cm^{-1}) anharmonicity and ~19 psec lifetime were measured for the first-excited CH stretch mode. The bare reconstructed C(111)-(2x1) surface showed the presence of CC stretch modes. By a polarization analysis of the SFG spectra, these were consistent with the Pandey π-bonded chain structure. When exposed to the methyl radical, the SFG spectra suggested that methyl species were terminating the

surface. After heating to sufficiently high temperatures, they were converted to the monohydride species. The preliminary result for the nature of the hydrogen termination on the diamond (100) surface suggests a monohydride termination.

A natural extension is to carry on with similar experiments for the C(100) surface as was started in Ch. VI. In addition, the C(110) surface should be studied. Because the (110) surface is a more open surface lattice only a monohydride termination of the topmost carbon atoms should occur as the steric hinderance should be much less than for the (100) surface. As a result, the likelihood of having a well-ordered hydrogen terminated surface is high, which should result in a strong, narrow CH peak in the SFG spectra.

In all the experiments described above, only reactants involving hydrogen and carbon have been involved. However, it has been shown that oxygen is good at increasing the growth rates in the CVD diamond growth process. Others have put various halogens on the diamond surface, as well. For the SFG studies, the limitation of the infrared source would allow only studies with atoms lighter than oxygen as the heavier elements bonded to carbon would have vibrational frequencies too low for observation with our apparatus. The carbon oxygen bonds can be seen at ~1700 cm^{-1} for doubly bonded CO bonds. However, for singly bonded CO bonds, the frequency is located at ~1150 cm^{-1} which is near the limit for the present apparatus.

Appendix A: Widely Tunable OPG/OPA/DFG Infrared System

This appendix discusses the details of the widely tunable, narrow linewidth, near-infrared to far-infrared generator used for the experiments contained within and extensive to this article. As mentioned in chapter II, this system was somewhat described by Zhang *et al.* In that paper, an academic demonstration of the general behavior of the design was presented. Since then, the system was developed into an automated subsystem of the SFG apparatus able to be operated in a variety of configurations.

The purpose of the inclusion of this appendix in this document was to assist future users and experimentalists with the use of the aforementioned design. There were many subtle issues that took several months to refine in order to get the best and sufficiently useful performance for practical experiments.

It is assumed that the reader is familiar with the paper by Zhang *et al.*, as the purpose here is for a more practical understanding of system's operation.

The discussion here is broken into two major subsections: the BBO OPG/OPA visible / near-infrared stage and the Difference Frequency Generation (DFG) amplification stage utilizing $LiNbO_3$ or $AgGaS_2$.

As mentioned earlier, a Nd:YAG system produced ~50 mJ of 1064 nm light in a 25 psec pulse. 18 mJ of this 1064 nm beam was used to generate SHG (532 nm) in a temperature-tuned lithium borate (LBO) crystal. The crystal size was 5(H) x 5(W) x 6(L) mm^3 held at ~150.5°C within a large copper oven. Both crystal faces were AR coated for both 532 nm and 1064 nm light and for protection of the hydroscopic surfaces. The 1064 nm beam size was ~3.0 mm in diameter with an intensity of ~10 GW/cm^2 sufficient to cause efficient conversion. The SHG conversion was ~70 % yielding ~12 mJ of 532 nm green light. Originally, an angle-tuned LBO crystal was used but proved to be inadequate. In the case of temperature-tuning, the larger acceptance

angle and relaxed phase matching conditions gave a much higher conversion efficiency. When operated in the saturation regime, the fluctuations of the SHG output (and all stages subsequently) was less sensitive to the fluctuations (short and long time scale) of the Nd:YAG laser. Additionally, because of the increased efficiency (~2x), the higher available power enabled greater outputs.

It should be noted that although the damage threshold of BBO is very high, there can be significant degradation of the hydroscopic surfaces if exposed to air. In the present system, the BBO crystals were situated within a purged dry nitrogen box. An alternative solution is to AR coat the crystals or situate them within a sealed box with windows containing dessicant. This latter solution, however, might prove to be awkard as the crystals must be rotated for angle-tuning. The freshly polished, uncoated BBO and LBO crystals were carefully measured to have damage thresholds at 25 GW/cm^2 and 40 GW/cm^2 ($\pm$20 %), respectively, measured at 1064 nm (35 psec) gaussian mode.

For a short time subsequent to the initial basic design, a 355 nm pump beam was generated using two LBO crystals. One for SHG geneneration and the second for 355 nm generation using 1064 nm and 532 nm light. Although a 355 nm pumped BBO enabled a greater tunable range than for 532 nm pumped, the decision was made to use the 532 nm pumped scheme for several practical reasons. First, greater efficiency of the BBO stage to produce near-infrared light was desirable as it would be the primary seed beam for the DFG stage. Secondly, because the tuning range desired was close to the degeneracy point of the crystal, the alignment of the crystals would not be as critical because of the relaxed phase matching condition. This was clearly desirable as the tuning range and hence the beam parameters would change considerably over a wide scan range. Thirdly, 532 nm generation would have resulted in less power fluctuations than a similarly simple 355 nm generation scheme as one less nonlinear process would be required.

Once it was decided that 532 nm would be the pump, the design would have to be refined for user-friendliness. The pump (532 nm) would pass through two BBO crystals ($5 \times 5 \times 10$ mm^3) which had its tuning rotation in the horizontal plane (Type I phase matching). The pump (horizontally polarized) with ~5 GW/cm^2 intensity was slightly divergent by the telescope located just before the SHG generator also served to compress the beam size. As shall be pointed out shortly, a divergence (~5 mrad) of the beam *was* desirable.

The BBO crystals being rather long, efficiently generated the signal and idler beams. This was almost too much as the crystals must be sufficiently separated to prevent unwanted light generation off-axis (such as for the degenerate 1064 nm) which would lead to poor power and stability at the desired frequency. The output after the first two-crystal pass was ~1.5 mJ. However, this had a very broad linewidth (>20 nm) due to the proximity of the degeneracy point. The pump was extracted to an adjoining delay arm with the signal beam sent to a grating in Littrow geometry. In this particular system, the polarization of the signal beam was vertical so a two mirror arrangement rotated the polarization enabling an incident grating polarization that gave maximum diffraction efficiency for horizontal rotation of the grating. A 10:1 telescope was used for angular magnification of the grating's dispersion by a factor of 10 on the return trip. This enabled a narrower linewidth of the signal seed beam which would then be amplified upon the second pass through the same BBO crystals.

It was mentioned in the orignal paper that it would be important to illuminate the most grating lines to obtain the narrowest linewidth. However, this was not the case. The limiting factor was the acceptance angle determined by the size of the pump area within the BBO crystal on the second pass. An analogy would be a monochrometer having a large exit slit. The limiting factor was now determined by the "effective dispersive power" of the grating and not the number of grating lines illuminated as would

be the case for very narrow entrance and exit slits. Unfortunately, the signal beam must pass through the same telescope on its way to the grating which magnified the beam diameter by a factor of 10. This was not desirable since the larger beam now has a temporal dispersion across its diameter from the Littrow geometry. A better arrangement would have been a double-pass first-order diffraction of the grating using a rotating mirror at normal incidence to the desired diffracted signal beam (see inset, Ch. II, Fig. 2). The temporal dispersion across the beam would then cancel on the second diffraction pass. This change was not done on the current setup since this was not crucial. Another added benefit of the 10:1 telescope was the ability to adjust the divergence of the signal beam to prepare it for amplification on the second BBO pass.

Meanwhile, the diverted green pump was sent along a delay line so that it would be able to temporally/spatially rejoin the narrow linewidth seed signal beam for amplification on the second BBO pass. The green beam was slightly divergent serving two simultaneous benefits. First, the intensity was lowered (~2 GW/cm^2) so no OPG action and no power broadening on the second pass would spoil the narrow linewidth. The second was that the full available energy of the pump beam could be utilized in a now larger beam through the crystals giving greater output (~800 μJ, signal and idler). Adjustment of the signal seed beam using the 10:1 telescope provided good overlap with the now larger pump beam. If needed, an additional attenuator could be placed within the green delay arm to reduce the second pass intensity without changing the other beam parameters.

At this time, it should be emphasized that the Pellin Broca prisms (before the BBO first pass and before the BBO second pass) were crucial for excluding the possibility of the 1064 nm light or broadband signal beams spoiling the desired processes. As the narrow linewidth seed beam was amplified, the complementary idler beam generated had a linewidth identical to the signal beam. Because the 532 nm pump beam had a 2 cm^{-1}

linewidth, this was the limit that one could achieve on the second pass output even if the grating returned an extremely narrow linewidth seed beam. Indeed, this was confirmed by measurement.

The final output from the second pass amplification gave a total of 800 μJ signal and idler beam output with vertical polarization. With the grating blocked, the absence of the seed beam then allowed evaluation of the second pass pump beam parameters. In this mode, the second pass output was less than 5 μJ. This small amount was representative of the amount of OPG occurring on the second pass. This amount was found to be smaller (with a good safety margin) than the amount which would spoil the narrow linewidth output. The consequence of having too intense a second pass pump beam was the amplification of the seed beam and the generation of a broader beam centered at the frequency of the gain maximum. Since there was no guarantee that the two frequencies were the same (unless an extremely good alignment occurred) , an undesirable double-peaked output generally resulted.

The original goal for maximum energy output and a narrow linewidth would require higher intensities and extremely good alignment. This would not be feasible in a practical scanning system where an extremely good alignment over the whole scanning range would be impossible to sustain. The scheme of using much lower intensities and a diverging pump beam (utilizing all available energy) then became the only choice.

The output of the second pass BBO amplification passes through a 532 nm rejection mirror and then the signal and idler components may be separated by dielectric mirrors, absorption filters, or dispersing elements.

With ~400 μJ of idler (~1.2-2 μm) and a 1064 nm pump in another nonlinear crystal, difference frequency generation (DFG) allowed the generation of light from 2.5 μm to ~12 μm with a narrow linewidth. Type II phase matching was utilized with the

pump horizontally polarized, the seed beam vertically polarized, and the DFG output vertically polarized.

Actually, DFG is like OPA except with the two input beams being comparable in intensity. The crystals used were $LiNbO_3$ and $AgGaS_2$. Although the use of the former seems redundant as the $AgGaS_2$ covers this frequency range, this is not quite true. The greater flexibility of $LiNbO_3$ allows greater output of energy with its higher damage threshold and good nonlinearity. In addition, since the $AgGaS_2$ crystal was extremely costly and the angle tuning large to cover the whole 2.5 μm to 12 μm range, a smaller crystal with a more limited angle tuning range in the more exotic range (4 μm to 12 μm) was economically advantageous. The crystal used was optimized for the 6.5 μm wavelength in the center of the tuning range. The crystal dimensions were 8(H) x 10(W) x 15(L) mm^3 with a cost of US$ 5800 (1993) including AR coatings for the input and output faces.

For the DFG crystal, the 1064 nm pump intensity was limited by the damage threshold of the $AgGaS_2$ material. By experience with earlier crystals, the damage threshold was ~0.5-0.9 GW/cm^2 depending on the crystal. This type of damage was difficult to characterize as it varied from one crystal to another. As well, this type of damage was not the usual photoionization avalanche process which occurred at much higher intensities. It seemed to be a slower process associated with an accumulated exposure at intensities over the above mentioned values. The manufacturer has indicated it to be a damage process associated with the surface of the crystal (unaffected by the AR coatings). They believe the process was related to the migration of silver ions near the surface.

The DFG (idler) output after a germanium plate at Brewster's angle resulted with the power curve given in Fig. 3 of chapter II. About ~300 μJ of the BBO idler and ~5 mJ of the 1064 nm pump was used. If the seed idler was reduced by half, the DFG output

only decreased slightly but became more unstable. As the DFG output wavelength increased, the energy steadily decreased until around 9 μm where the crystal's bulk absorption was strong.

In the 2.5 μm to 4 μm range, $LiNbO_3$ was used with the same parameters as that for the $AgGaS_2$ crystal. Although not optimized, the idler output energy was a satisfactory 150-200 μJ.

Generally, CaF_2 lenses were need after the germanium plate to control the divergence of the beam. The lenses were chosen to image the DFG crystal to an appropriate point downstream. The use of CaF_2 was chosen by the availability of existing components and a need to only cover to ~8 μm at the time. Since they have a cutoff at about 8.5 μm, it should be suggested that BaF_2 , ZnSe or ZnS be used to cover the whole output range. Even better, the use of off-axis paraboloid gold mirrors would minimize the reflection losses.

Another item worth mentioning was that the wide tuning range of the one $AgGaS_2$ crystal displaced the beam substantially. A glass or fused quartz block acting as a compensating element *before* the $AgGaS_2$ crystal should be used. With each "crystal" oppositely rotated, a fixed placement of the output beam results.

Appendix B: Assorted Infrared SFG Spectra for Different Bond Types

In this appendix, several spectra spanning the range from ~1000 to 4000 cm^{-1} were presented. Its purpose was to serve as a reference for the many spectra taken on the existing SFG system.

As mentioned in Chapter II, infrared-visible SFG spectra depends on several factors including non-resonant backgrounds, a response by both infrared and Raman processes, and polarization dependences. Since the process is inherently a surface specific probe of solid-gas, solid-liquid, solid-solid, liquid-liquid, and liquid-gas interfaces, the spectra may be different from the bulk spectra as the interface can have a different chemical environment. This may result in frequency shifts, intensity and polarization ratio changes within the vibrational signatures. The intent was that the spectra may represent a typical sampling of what can be expected using the SFG technique.

For the majority of the content within this document, the carbon-hydrogen bond has been explored in the stretch and the bending/deformation ranges. Here, spectra of other bond types are additionally presented. A brief description of the system associated with the spectrum was provided in the figure captions.

Figures

Fig. 1. The liquid-gas interface of ethanol using ssp polarization geometry. Both the CH_x stretch (2700-2950 cm^{-1}) and the OH stretch (3000-3400 cm^{-1}) features were seen. The spectra below 3000 cm^{-1} used the 4 cm^{-1} linewidth infrared source whereas the spectra above 3000 cm^{-1} used the ~30 cm^{-1} linewidth.

Fig. 2. The liquid-gas interface of acetone. The CH_3 symmetric stretch (~2930 cm^{-1}) mode seen using the ssp polarization geometry (open circles). The solid line represents a two peak fit (one resonant term has opposite phase) with a nonresonant background. The dotted line is for a one peak fit. The spectrum for the sps polarization combination (open squares).

Fig. 3. The solid-gas interface of 8CB (cyano-biphenol) on fused silica using ssp polarization. The CN stretch (~2230 cm^{-1}) mode was clearly distinguished.

Fig. 4. The liquid-solid interface of propionitrile and BaF_2 using ssp polarization geometry. The $CH_{x=2,3}$ stretch (2800-3000 cm^{-1}) and CN stretch (~2260 cm^{-1}) modes were seen.

Fig. 5. The liquid-gas interface of stearic acid on water (pH=7) using ssp polarization geometry. The COO··H stretch (1670-1750 cm^{-1}) mode signatures show three distinct features.

Fig. 6. The solid-air interface of hydrogen terminated porous silicon (~5-10 nm characteristic length scale) using ssp polarization geometry. The $SiH_{x=1,2,3}$ stretch modes (2050-2200 cm^{-1}) were seen with the corresponding *transmission* spectrum shown for comparison.

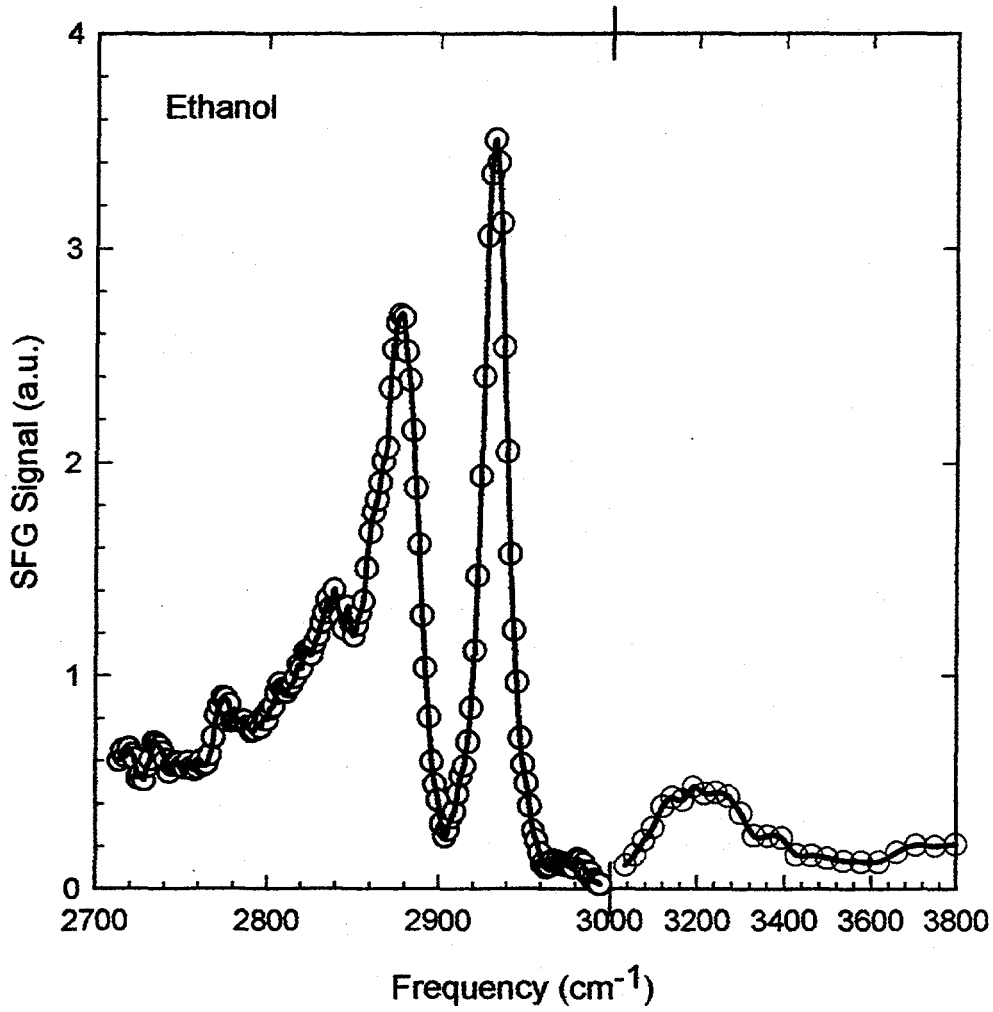
Ethanol
SFG Signal (a.u.)
Frequency (cm-1)
0
1
2
3
4
2700
2800
2900
3000
3200
3400
3600
3800

Fig. 1

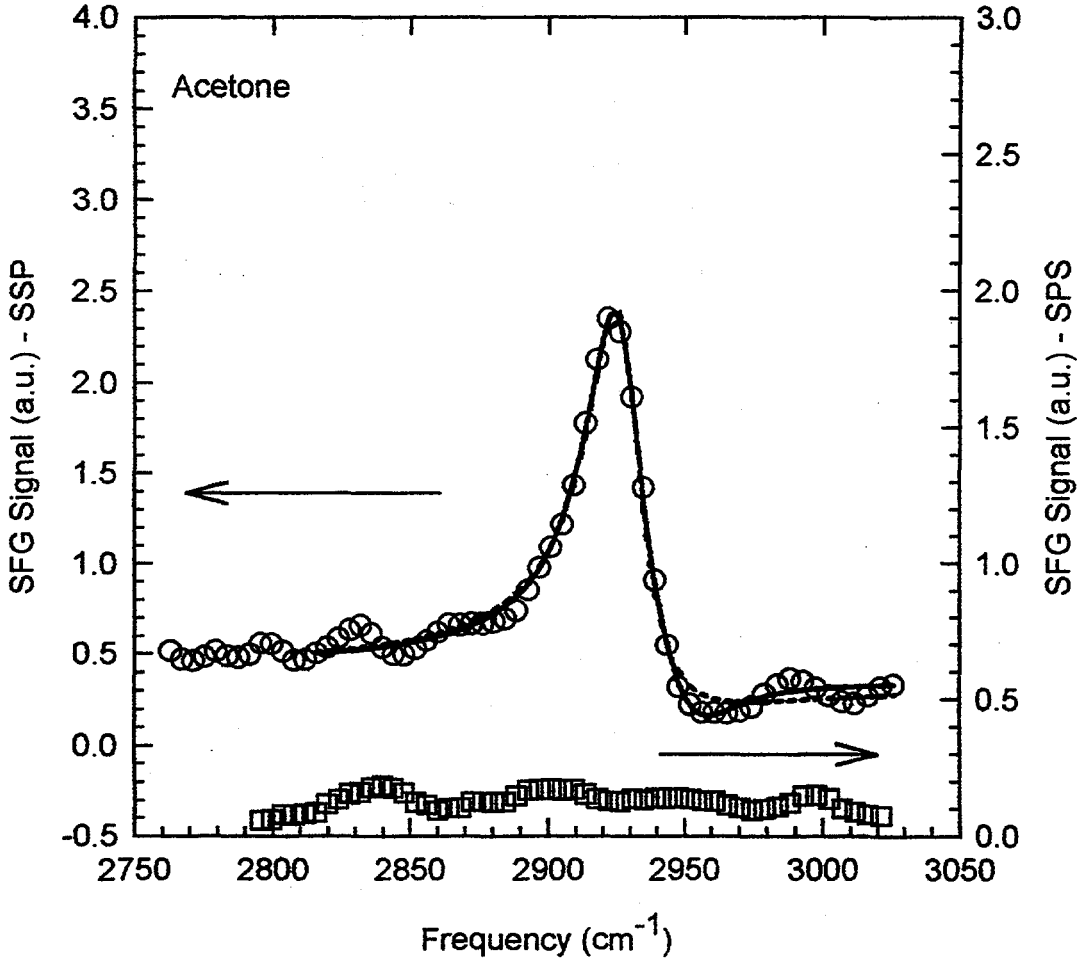
Acetone
SFG Signal (a.u.) - SSP
SFG Signal (a.u.) - SPS
Frequency (cm^{-1})
4.0
3.5
3.0
2.5
2.0
1.5
1.0
0.5
0.0
-0.5
3.0
2.5
2.0
1.5
1.0
0.5
0.0
2750
2800
2850
2900
2950
3000
3050

Fig. 2

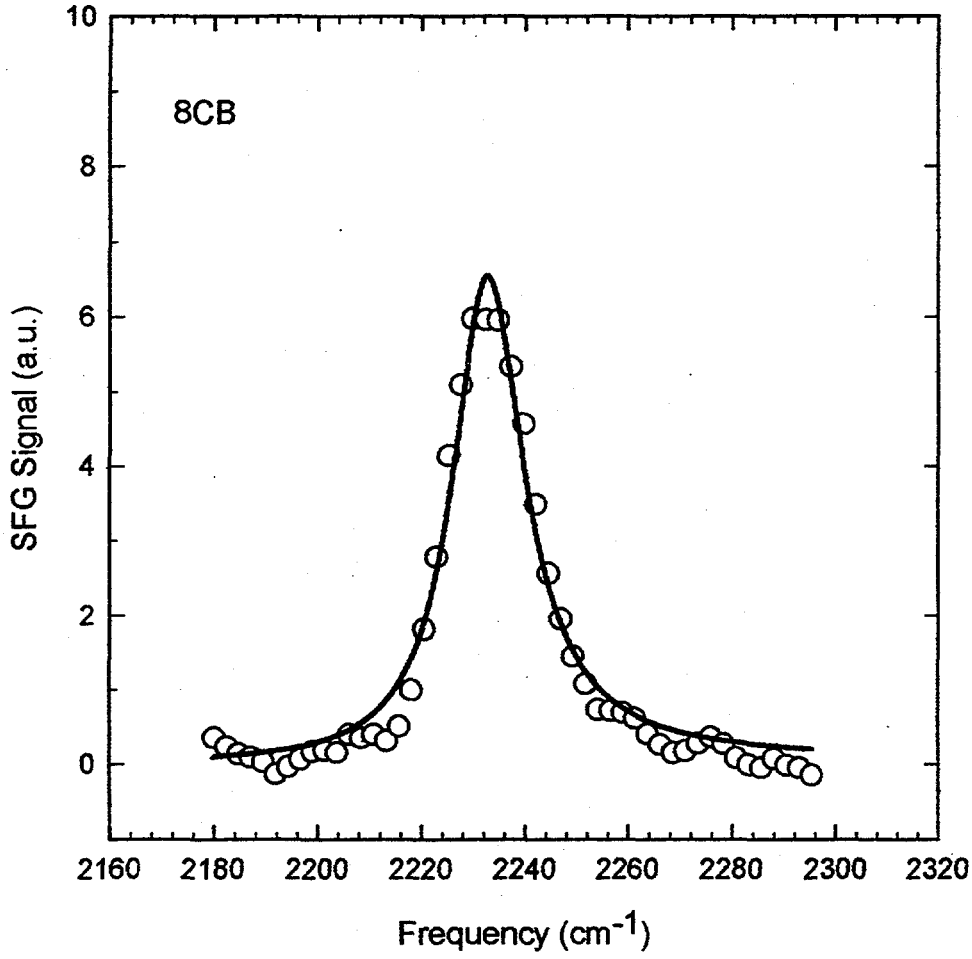
8CB
SFG Signal (a.u.)
Frequency (cm-1)
0
2
4
6
8
10
2160
2180
2200
2220
2240
2260
2280
2300
2320

Fig. 3

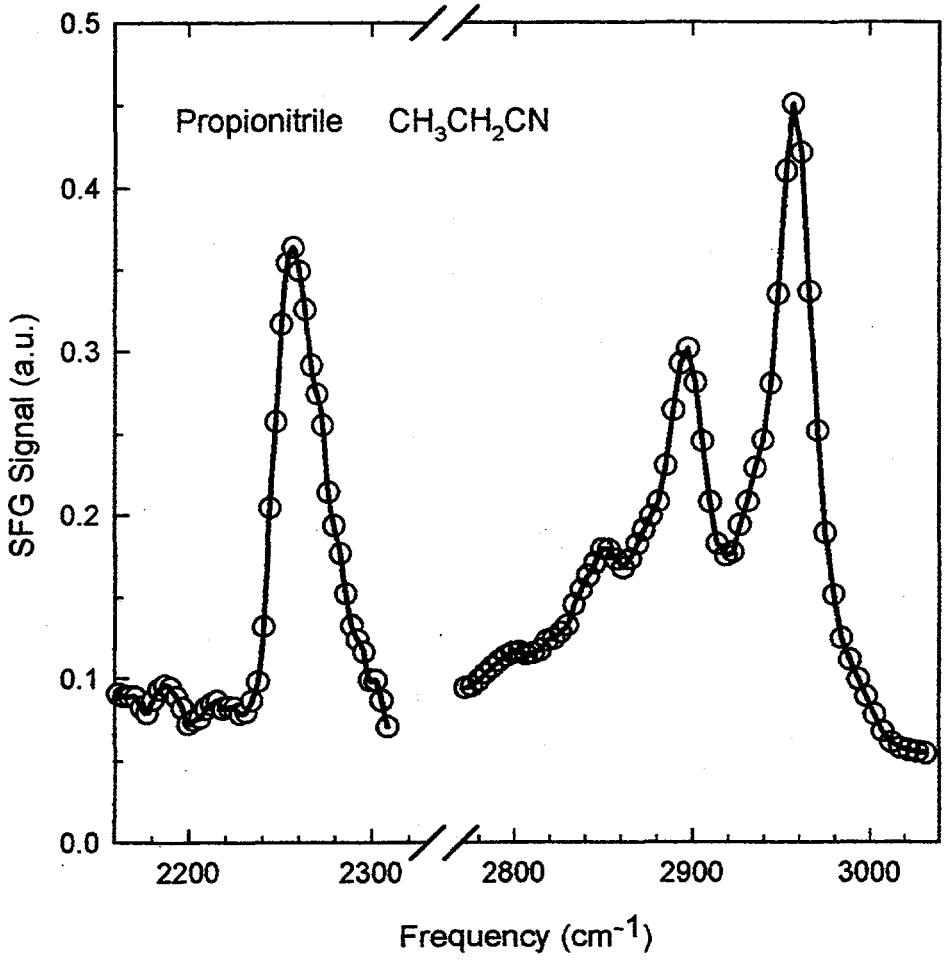
Propionitrile CH3CH2CN
SFG Signal (a.u.)
0.0
0.1
0.2
0.3
0.4
0.5
2200
2300
2800
2900
3000
Frequency (cm-1)

Fig. 4

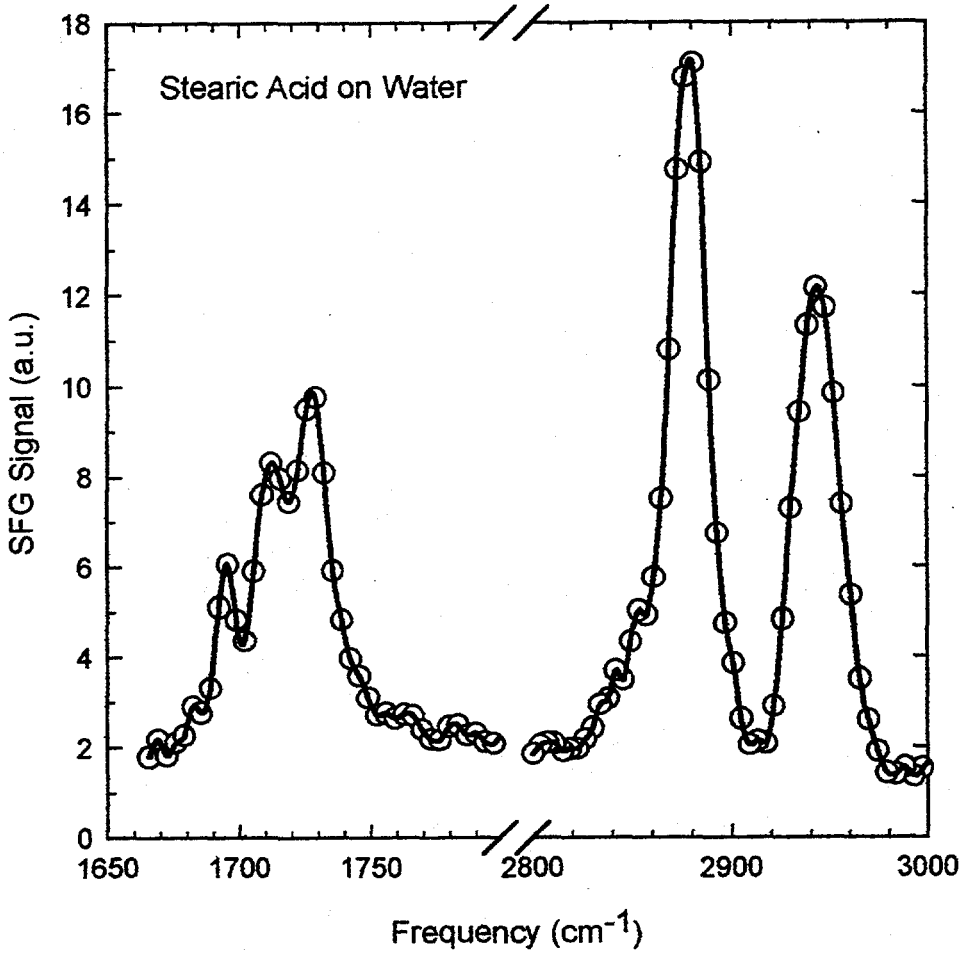
Stearic Acid on Water
SFG Signal (a.u.)
Frequency (cm-1)
0
2
4
6
8
10
12
14
16
18
1650
1700
1750
2800
2900
3000

Fig. 5

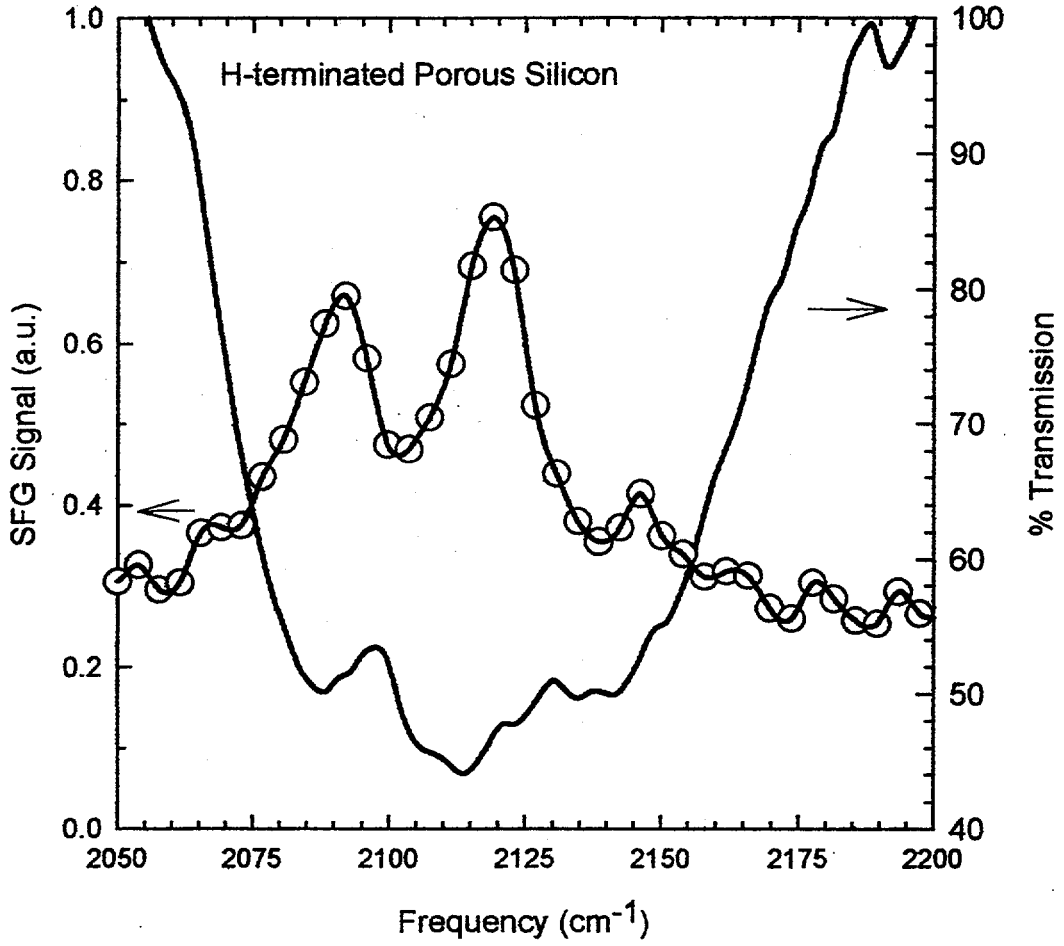
H-terminated Porous Silicon
SFG Signal (a.u.)
% Transmission
Frequency (cm-1)
1.0
0.8
0.6
0.4
0.2
0.0
100
90
80
70
60
50
40
2050
2075
2100
2125
2150
2175
2200

Fig. 6